UNIVERSITY OF OKLAHOMA

GRADUATE COLLEGE

THE EFFECT OF PORE SPACE ON FLUID FLOW AND PHASE BEHAVIOR IN TIGHT FORMATIONS

A DISSERTATION

SUBMITTED TO THE GRADUATE FACULTY

In partial fulfillment of the requirement for the

Degree of

DOCTOR OF PHLOSOPHY

By
SHADI SALAHSHOOR
Norman, Oklahoma
2019

THE EFFECT OF PORE SPACE ON FLUID FLOW AND PHASE BEHAVIOR IN TIGHT FORMATIONS

A DISSERTATION APPROVED FOR THE

MEWBOURNE SCHOOL OF PETROLEUM AND GEOLOGICAL ENGINEERING

BY

Dr. Mashhad Fahes, Chair

Dr. Catalin Teodoriu

Dr. Ramadan Ahmed

Dr. Xingru Wu

Dr. Jeffrey Harwell

Acknowledgements

I would like to thank my advisor Dr. Mashhad Fahes, for her guidance, support and invaluable advice throughout my research. Thank you for being a smiling face, even on my darkest days and for encouraging me to always take care of myself mentally, physically, spiritually, and emotionally. You have been not only the academic advisor, but also the mentor I always wanted and without you I would not be the confident woman I am today.

Besides my advisor, I would like to thank the rest of my Ph.D. committee: Dr. Teodoriu, Dr.Wu, Dr.Ahmed, and Dr. Harwell for their insightful comments and encouragement. Without their advice and feedback, completion of this work would not have been possible.

I would also like to extend my deepest gratitude to Dr. Maysam Pournik for all his help and support. It is impossible for me to forget his role in my life; I would not be where I am today without his support through one of the most difficult times in my life.

This research work involved conducting laboratory experiments and it could not happen without the help from a number of people. I am also grateful to Dr. Teodoriu, Gary Stowe, Dr. Tinni and my amazing lab-mates for their invaluable assistance in resolving many experimental complications.

There are many more people that have earned my gratitude for their contribution to my time in graduate school by connecting, inspiring, collaborating, interacting, and challenging, academically and personally. I am thankful to all of you, I could not accomplish this without every one of you.

Last but not the least, I would like to thank my wonderful parents for their patience, love and support along this way. Thank you for inspiring me to dream big and encouraging me to follow my passion without letting anyone or anything stop me. I am indebted to my parents for inculcating in me the dedication and discipline to do whatever I undertake well.

My special appreciation goes to my love, Hamid, who is a true and great supporter and has unconditionally loved me during my good and bad times. Thank you for always believing me and my intellect even when I didn’t have faith in myself. These past five years have not been an easy ride, but it would have been impossible without having you in my life!

Table of Content

List of Figures

List of Tables

Abstract

Unconventional resources have led to a new abundance of natural oil and gas supply all over the world over the past decade and are expected to play a vital role in the future of this industry. Despite tremendous growth of extraction technologies which increased the production of these reserve significantly, knowledge and understanding of flow and phase behavior of the fluid in unconventional resources has remained insufficiently explored.

Accurate understanding of phase behavior of fluids trapped in the extremely small pores of these resources, especially shale reservoirs, is the center of attention for a lot of scholars globally. Although numerous mathematical and theoretical studies are available to explain phase behavior of confined fluids, limited number of studies attempted to explore this effect experimentally. Experimental data are invaluable in providing the deep insight needed to explain this effect, validate available models, and introduce methods of characterizations that would help with optimization of production plans.

The present work is an attempt to enhance the understanding of fluid phase behavior in tight formations through experimental investigations. Microscopic effects and their macroscopic consequences that plays a crucial role in adding to the complexity of fluid phase behavior in these reservoirs are explored and explained prior to discussing modeling and experimental works. Fundamental knowledge of phase behavior and thermodynamic principals that are essential for exploring this effect and for comparing the shortcomings of established experimental approaches in phase behavior studies of conventional reservoirs are covered. A thorough review on the existing theoretical and experimental studies on the topic, considering their results and predictions, is conducted to shed more light on the need for further experimental investigation of phase behavior alterations in tight gas condensate formations.

Isochoric method is an indirect high-precision way of phase transition point determination which is commonly used in other disciplines where a clear non-visual determination of phase transition of a fixed volume of fluid is needed. The present work provides an insight into using this approach in determining dew pint pressure (DPP) for gas mixtures inside and outside of the porous media. A semi-automated apparatus for measuring and monitoring equilibrium conditions along with fluid properties is designed based on the isochoric method. The apparatus provides constant volume, variable pressure (0 to 1500 psi), and variable temperature (290 to 410 K) experimental conditions. Pressure and temperature measurements are used to detect the phase transition point along the constant-mole-constant-volume line based on the change in the slope of this line at the transition point. A packed bed of $BaTiO_3$ nanoparticles, providing a homogenous porous medium with pores of 1 to 70 nm is used as a representative nano-scale porous medium. The synthesized porous medium is very helpful in uncoupling the effect of pore size from the effect of mineralogy on the observed deviations in behavior, providing a volume more than 1000 times larger than typical nano channels.

The result is a set of Isochoric lines for bulk and confined sample, plotted on the phase envelope to demonstrate the change in saturation pressure. Phase envelopes (P-T diagrams) of the same mixture using different equations of state are constructed and the accuracy of each of these equations of state in providing an experimentally detected DPP is discussed. Many attempts in explaining the shift in saturation pressures of the reservoir fluid confined in the narrow pores of unconventional reservoirs compared to those of the bulk can be found in the literature. However,

there are some contradictions between the predicted behavior using different mathematical approaches. Experimental data could be substantially helpful in both validating models and improving the understanding of the fluid behavior in these formations. Contrary to what many published models predict, the results of the present work show that confinement effects shift the DPP towards higher values compared to the bulk for a fixed temperature in the retrograde region. In the non-retrograde region, however, this shift is towards lower dew point pressure values for the confined fluid compared to the bulk. Capillary condensation is identified to be the main source of the deviations observed in the behavior of fluids inside nanopores. We evaluated published models, including those based on EOS modifications, by comparing it to experimental results to provide a quantification of their accuracy in estimating saturation pressure values for the confined mixture. Future applications of the present work for directing it towards an all-inclusive theory for all reservoir fluids in unconventional formations are clearly outlined.

Chapter 1: Introduction

Unconventional reservoirs are hydrocarbon reserves whose production requires specific high technology operations outside the scope of conventional practices used throughout decades to produce oil and gas, including shales, tight sands, and tight carbonates, form extremely large natural gas resources. Despite conventional reservoirs, these rapidly growing reservoirs are dispersed over large areas which makes them difficult to be produced. However, as stated in the EIA natural gas production forecast graph, unconventional gas, specifically shale gas, is predicted to increase the total amount of gas production by 56% from 2012 to 2040 based on the EIA 2014 annual report.

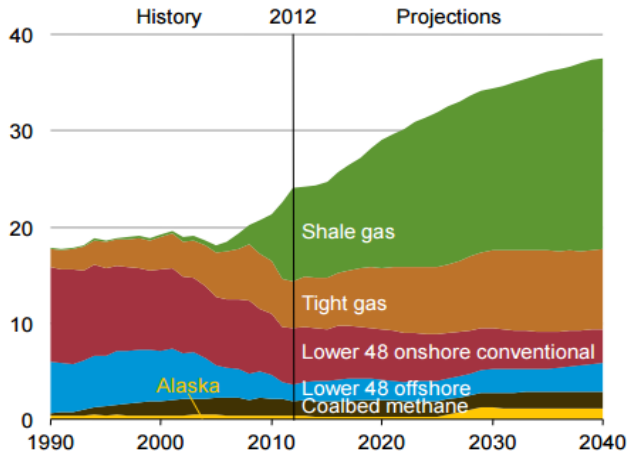

Figure 1.1. Historical and projected sources of natural gas in the United States (EIA's Annual Energy Outlook, 2014).

Despite the tremendous success in developing new methods of extraction such as horizontal drilling and advanced stimulation techniques such as multi-stage fracturing, the industry faces many operational challenges which include low recovery factors, rapidly declining production rates, and uncertainties in reserves and production estimates due to the unique criteria and unknown fluid flow and phase behavior in the tiny pores. While the diameters of pore-throats in conventional reservoirs are larger than 2 μm, in tight formations, pores are about 2 to 0.03 μm in diameter, while in shale reservoirs, it ranges from 0.1 to 0.005 μm (Nelson, 2009).

Knowledge of fluid phase behavior is crucial to the efficient production of hydrocarbons from all reservoirs. Improper characterization and wrong models of phase behavior are a major cause of many production problems faced by the industry in both conventional and unconventional reservoirs. Based on ExxonMobil's energy outlook of 2014, almost 40% of the world-wide natural gas reserves are contained in unconventional reservoirs including shale gas, tight gas, and coalbed methane (Toscano et al., 2016). A clear majority of studies in this area are theoretical models with the aim of simulating the effect of pore geometry and pore sizes on phase behavior. Although there are some contradictions among the outcomes of these theoretical methods, almost all of them approved that the presence of small pore spaces in porous medium alters the phase behavior from what is observed in conventional resources and experiments. What prevents researchers from validating their models is the limited experimental data on the effect of nano-confinement. Quite

many experiments have been conducted to investigate the effects of fluid phase behavior on oil and gas reservoirs production. However, most of these experiments are conveyed under static condition in traditional PVT cells with a bulk volume of 20 cc to 100 cc and does not account for the effect of a porous medium with tight micro- and nano- scale pore spaces which are considered as the source of unique storage and flow characterization of tight formations and shales. Hence, exploring this effect experimentally creates an effective path in making accurate production plans for this category of reservoirs.

Shale reservoirs are basically mudstones or carbonate rocks primarily acting as source rock in a petroleum system. They usually spread over a long distance with low thickness of the play. These layers have both organic and mineral pore spaces and nano-pores are abundant in both parts. As mentioned earlier, phase behavior and production mechanisms are significantly different under nanoconfinement because of the capillary pressure, curvature, adsorption, nonhomogeneous fluid density, and other effects. A better understanding of the phase behavior of the fluid inside nano-pores may lead to additional characterization techniques for the shale plays and therefore, lead to improvement in hydrocarbon recovery from these widespread huge reservoirs with considerable producible hydrocarbon all around the world.

Aside from the significantly large capillary pressure in small pores which cause deviation in phase behavior of confined fluid from that of the bulk which affects flash and VLE (Vapor-Liquid Equilibrium) calculations considerably, the presence of organic matter (kerogen) in shale reservoirs elevates the effect of adsorption which is another controlling factor in VLE calculations. Many scholars have explored the extend of adsorption in shale reservoirs both theoretically and experimentally.

adsorption studies in shale media are mostly limited to methane (CH_4) which has been considered as an important factor in gas production, and CO_2, which is widely used for sequestration in enhanced and improved oil and gas recovery.

1.1. Characteristics of Shale Reservoirs

The uniqueness of shale reservoirs is tightly related to their exceptional structure, mineralogy, and hydrocarbon generation process. In these reservoirs, bitumen and hydrocarbons are generated at the same time as the organic network of kerogen develops throughout the primary migration. During this period, multicomponent equilibrium exists between kerogen and the hydrocarbon components that are generated by the decomposition of kerogen in the period of its maturation (Ertas et al., 2006). Ross and Bustin (2009) present a correlation between the TOC of shale and its storage capacity for the Western Canadian Sedimentary Basin (WCSB) based on the improved adsorption capacities of organic rich shale strata (higher TOC) compared to organic-lean (lower TOC) ones, which indicates that organic-rich shales (TOC>2 wt.%) generally contain more gas than organic-lean shales (TOC<0.5 wt.%).

It should be noted that pore structure complexities and surface area heterogeneities in nano-pores of shale, makes it difficult to present a solid prediction on the sorbed storage capacities of shale only based on TOC. Each shale reservoir requires multifaceted reserve estimation considering other reservoir parameters such as moisture, temperature, porosity, and maturation

level of the present organic matter. For example, Bakken formation, located in Williston basin covering an area of 300,000 square miles with the maximum thickness of 160 feet (Pathak et al., 2014), has the average TOC varying from 25 to 28 percent and contains roughly 5.972 billion barrels. of proved reserves; while Eagle Ford formation located in the area of Gulf of Mexico covering an area of just about 20,000 square miles with the thickness of 50 to 300 feet, has the average TOC of only 2 to 4 percent and contains almost 5.172 billion barrels of proved reserves based on EIA's report in 2014 (Cho et al., 2016). In general, the amount of organic matter along with the decrease in pore sizes elevate the adsorption effect. The importance of the impact of adsorption effects and pore sizes on fluid phase behavior predictions encouraged many scholars to investigate methods of measuring adsorption in porous media, as well as methods for accurate pore size measurements.

1.2. Pore Size Distribution

The pore size distribution in shale has been profoundly investigated as one of the unique characteristics of shale reservoirs. The shale matrix is mainly composed of pores in the range of 2 to 50 nm and has a considerable number of pores less than 2 nm in diameter (Kuila and Prasad, 2013).

The importance of the effect of pore size on phase behavior has been explored by many scholars. One of the earliest attempts to study fluid behavior in narrow pores was done by Peterson et al. (1986). The Density profile and grand potential of the fluid (Argon-CO_2) were examined by varying the pore radius under different conditions. In all cases, for a fixed temperature, gas/liquid coexistence curve was shortened with decreasing pore radius. They also found that the strength of fluid-wall forces have a great impact on phase transition in smaller pores (Peterson et al., 1986).

Jackson and McKenna (1990) studied the effect of pore sizes on the phase behavior at the solid-liquid interface (the melting behavior) of organic materials using differential scanning calorimetry. A significant reduction in the measured bulk enthalpy of pore solid for a series of organic solids was noted, which is an indication of a decrease in melting point as a result of pore diameter reduction. They also found a linear correlation between the melting point depression of the confined nonpolar organic solid inside the pores and the reciprocal diameter of the pores for pore diameters from 40 to 370 angstroms (4 to 37 nm).

Bustin et al. (2008) presented a bi-modal pore size distribution with one mode around 10 nm for Barnett by implementing a methodology referred to as "MARIO", which eliminated the void volume error associated with using Helium for pore volume determination in shale. Sondergeld et al. (2010) indicated that pore sizes around 10 nm to 20 nm are abundant in shale samples based on SEM images; they also stated that flow characteristics of fluids in shale reservoirs are "uniquely tied to nano-scale pore throat and pore size distribution".

Mercury injection capillary pressure (MICP) tests can be used to study the pore throat size distribution (radii) in shale samples. Efforts for studying pore size ranges in shale media by many scholars confirm that shale consists of grain sizes less than 5 μm which form a considerable amount of pores with sizes in the range of 3 nm to 100 nm (Schettler et al., 1989, Sondergeld et al., 2010).

Typical pore throat diameters in shale reservoirs vary between 0.5 nm and 100 nm (Ambrose et al., 2010).

SEM images reveal that most of the pores with less than 50-nm diameter are located inside the kerogen rather than inside the non-organic parts of the rock. As the ratio of the pore inner surface area to the pore volume increases, the effect of surface-dependent phenomena such as desorption and diffusion increases. This means that the amount of hydrocarbon adsorbed to a surface or dissolved in the organic matter becomes more important. This is the main difference in fluid behavior between shale and conventional reservoirs or tight sands, and is also a source of difference between various shale formations (Etminan et al., 2014).

Cho et al. (2016) present a comparison between mineralogy, pore structure, pore size distribution, and organic content of Bakken, Eagle Ford, and Niobrara formations. MICP was performed on several samples from these formations and the results show low entry pressure (566 psi) for middle Bakken which explains the role of micro-fractures and larger pore-throat sizes (0.0240 to 0.1585 μm) in this formation on creating a relatively high permeable pathway. High intrusion pressures (above 10000 psi) for Niobrara samples is in agreement with the small pore-throat size (0.0046 to 0.0119 μm) in this clay-dominant formation. Lower Eagle Ford samples show a very similar behavior to Niobrara samples and pore-throat sizes for this formation is reported to be in the rage of 0.0089 to 0.0413 μm. Note that the dominant mineralogy in Bakken formation is dolomite, calcite, and quartz, in Eagle Ford formation is dolomite, calcite, clays, and quartz, and in Niobrara formation is calcite, illite/smectite clays, quartz, dolomite, albite and pyrite.

1.3. Physics Behind Fluid Phase Behavior in Confined Pore Spaces

To understand the underlying physics behind fluid flow and phase behavior in the tight pores of these reservoirs, one needs to explore key forces which are important at nano-scale pores and their influence on reservoirs production. Prior to that, pore structure and heterogeneity of tight reservoirs need to be understood. Geometric constraints and, as a result, disturbed interactions between molecules and pore walls are the source of confinement effect in tight formations.

In the pore network, fluid molecules have interactions with each other and with the pore walls. In larger pore sizes, molecules collisions with the pore walls are negligible compared to the interactions between molecules themselves. In tight reservoirs, fluid molecules are confined and the free path available to them is restricted by the geometry. Devegowda et al. (2012) presented that the effect of pore proximity is felt when the pore size to molecule size ratio is less than 20. In nano-scale pores, the molecules in the vicinity of pore walls are affected by pore-wall interaction forces which leads to alteration of fluid behavior from what one can see in conventional reservoirs consisting of comparatively large pores. This effect is schematically illustrated in Figure 1.2.

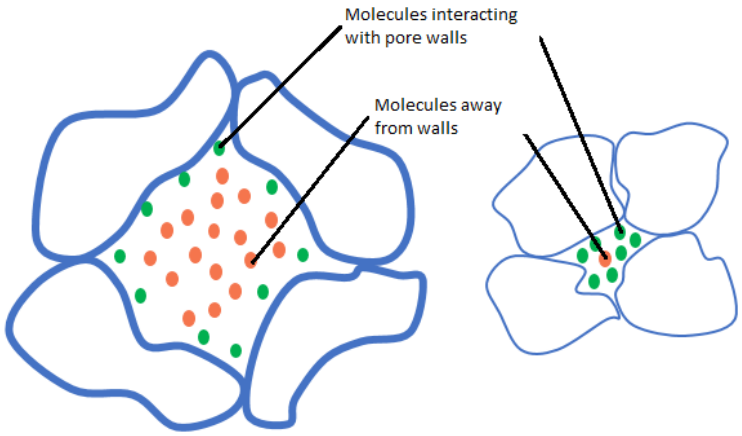

Figure 1.2. Schematic representation of confinement effect (left: large pore without confinement, right: tiny pore where confinement is significant)

This nano-scale pores can be either organic matter or mineral matrix pores. Adsorption happens in organic pores and dissolution happen in kerogen, but molecule-wall interactions happen in all type of pores. Many scholars approved that the changes of fluid behavior under confinement is because of increased influence of pore walls on the apparent physical properties of the fluid such as critical pressure and temperature, density, viscosity, surface tension etc. These elevated interactions increase the effect of capillary, structural, and adsorptive forces. Therefore, the effect of confinement on fluid behavior can be explored as below:

1.3.1. Molecular Interactions in Play

Molecular interactions are vital in fluid behavior in tight pore spaces and still need to be well understood. Intermolecular forces are generally divided into categories of opposites which are attractive/repulsive, short-ranged/long-ranged, and strong/weak (Israelachvili, 2011). For fluids in porous media, the most common models to study the intermolecular interactions are cylindrical or slit-like pores in which the width of the slit or diameter of the cylinder is in the order of a few to a hundred nanometers. Slit-pore is mostly used by scholars to model confined pore geometry. In a slit-pore, intermolecular forces of the confined fluid are described in three different categories (Lu and Hu, 2009)

- Interactions between fluid molecules (intermolecular interactions)
- Interactions between the walls and the confined fluid particles
- Possible forces between particles at the interface

Covalent or chemical bonds between atoms are the forces that combine atoms in the form of molecules and are out of the scope of our study. Ionic and polar interactions between atoms or molecules mostly deal with the chemical structures of fluid molecules. The type of intermolecular forces which act between all atoms and molecules are “dispersion forces”. They are long-ranged forces and depending on the situations can be effective at large distances (more than 10 nm) to very small distance (about 0.2 nm). These forces can be either repulsive or attractive. In the attractive case they are named “attractive dispersive forces” and in the repulsive case they are “short-ranged repulsive forces”. Attractive dispersive forces in combination with short-ranged

repulsive forces and "electrostatic forces"- in case of having polar molecules- are totally named and known as "Van der Waals" forces (Israelachvili, 2011). Van der Waals forces are the non-bonding forces acting as intermolecular and wall- molecule interactions. They are also dominant forces in physisorption (weak physical adsorption in the absence of chemical adsorption).

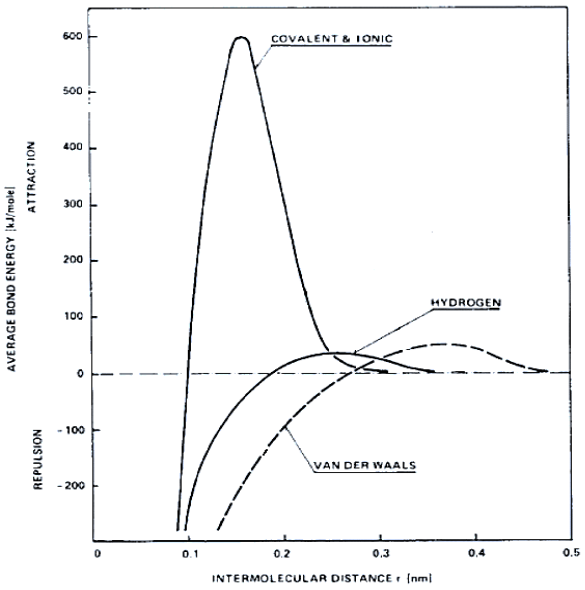

Figure 1.3. Effective range of intermolecular forces based on intermolecular distance (Lee, 1991).

As stated in Figure 1.3, attractive intermolecular forces have a relatively long range; and repulsive forces are significant only when molecules are very close to each other, so they are known as short-range interactions.

These interactions between fluid molecules with each other or with the surface (pore walls) can be described by a potential energy because the effect of all these interactions is reflected in the total potential energy of the pore-fluid system which can be derived from the following equation:

$$U_P = U_{ff} + U_{fw} + U_{ww} \qquad (1-1)$$

Where U_{ff} is the potential of molecule interactions in fluid, U_{fw} is the potential of fluid molecule interactions with pore walls, and U_{ww} is the potential of molecule interactions at the interface (between pore wall and the molecules) if it exists (Lu and Hu, 2009).

At solid interface, U_{ww} can be ignored because of negligible interactions. In this case intermolecular potential would be a combination of U_{ff} and U_{fw}. Therefore, total energy of interaction (potential of interactions) is a function of distances as represented in Figure 1.4.

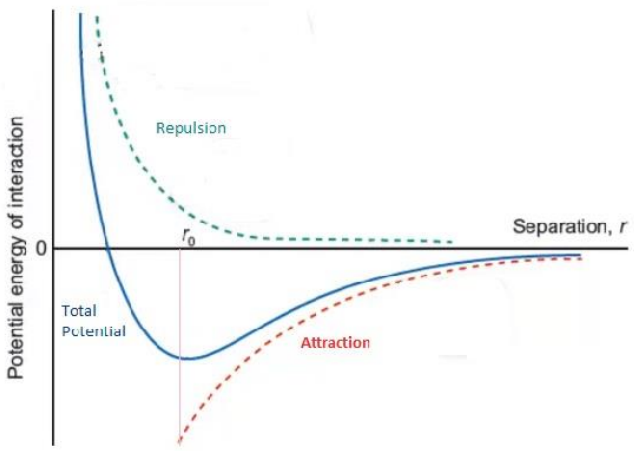

Figure 1.4. Total potential energy of interactions as a function of distance (r) (Lu and Hu, 2009)

There are several proposed intermolecular potential functions for different systems. One of the simplest and widely used models in confined fluid potential studies is the Lennard-Jones potential:

$$U(r) = 4\varepsilon\left[(\frac{\sigma}{r})^{12} - (\frac{\sigma}{r})^{6}\right] \qquad (1-2)$$

Where r is the distance between the centers of two particles, σ is the value of r at which the energy is zero, and ε is the strength of attraction between molecules. A schematic representation of Lennard-Jones potential model is shown in Figure 1.5.

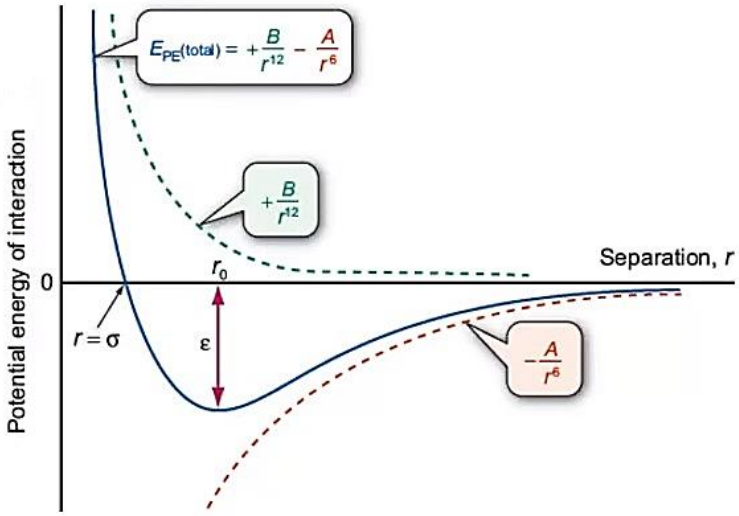

Figure 1.5. Molecular interaction and the Lennard-Jones potential (Oxford Academic Press).

The application of this intermolecular potential function is in the molecular simulations which has become a common method of modeling fluid behavior in nano-scale pores and one of

the well-known approaches in molecular simulation is "molecular dynamics" (MD). MD is basically a predictive tool to take into account the molecular interactions in determining fluid properties with a good accuracy.

For example, it can be used to reproduce molecular interactions between a surface and the fluid in order to determine the contact angle of the droplet with the wetting surface (Wang et al., 2016). It also is widely used to model the density of a heterogeneous fluid in confined pores (Peng and Yu, 2008, Li et al., 2014, Jin and Firoozabadi, Kamalvand et al., 2008). Examples and details of this methods are included in proceeding sections.

1.3.2. Capillary Effect Due to Confinement

Capillarity effect is elevated in nano-scale pores and underestimating this effect may lead to inaccurate estimation of recovery and saturation pressure. In fact, increased interaction of molecules with wall increases the capillary pressure which highly affects liquid vapor equilibrium. This effect results in density and viscosity reduction in oil, and density and viscosity increase in gas (Nojabaei et al., 2012). Capillary effect or interfacial tension can be calculated via the well-known Young-Laplace equation:

$$P_c = P_{nw} - P_w = \frac{2\sigma cos\theta}{r} \qquad (1-3)$$

Where P_c is the capillary pressure, P_{nw} is non-wetting fluid pressure (gas), P_w is the wetting fluid pressure (liquid), σ in the interfacial tension, θ is the wetting contact angle, and r is pore radius.

In conventional cases, vapor liquid equilibrium (VLE) calculation are done base on the condition that both phases are in chemical equilibrium; which simply means at constant pressure and temperature, chemical potentials are equal (for multi component systems) or Gibbs free energies are equal (for pure substances).

However, elevated capillary effect in nano-scale pores results in pressure difference even at equilibrium. Hence, to consider the effect of capillary pressure in VLE calculation, fugacities are considered equal for the two phases (gas and oil), while the pressures are different.

$$f_i^L = f_i^V \qquad (1-4)$$

$$P_v = P_L + \frac{2\sigma cos\theta}{r} \qquad (1-5)$$

Therefore the equilibrium constant K_i which is $K_i = \frac{y_i}{x_i} = \frac{\phi_i^l}{\phi_i^g}$ in conventional cases will be changed into $K_i = \frac{y_i}{x_i} = \frac{P_L \phi_i^l}{(P_L + P_c)\phi_i^g}$; where y_i is mole fraction of component i in gas phase, x_i is the mole fraction of component i in liquid phase, ϕ_i^l is the fugacity coefficient of component i in liquid

phase defined as $\phi_i^l = \frac{f_i^L}{x_i P_L}$, and ϕ_i^g is the fugacity coefficient of component i in liquid phase defined as $\phi_i^g = \frac{f_i^g}{y_i P_g}$ (Nojabaei et al., 2012).

Many substances are mechanically and adhesively very sensitive to the presence of even traces of "condensable" vapors; "vapors whose liquids form a small contact angle with the surface". Once the first meniscus is formed, it will result in increased van der Waals interaction between vapor phase molecules inside the space of a capillary. Therefore, this process proceeds to a multilayer adsorption from vapor to the solid pore wall (Israelachvili, 2011). This phenomenon is known as capillary condensation; it occurs due to the strong pore wall fluid molecule interactions in miniature pore spaces and can lead to the point that the entire pore space is filled with condensed liquid below the saturation pressure of the vapor, P_{sat}. Li and Firoozabadi (2009) proposed that the phase change due to capillary condensation could occur beyond the cricondentherm in nano-pores even when the bulk fluid is still in the single phase.

1.3.3. Adsorption Due to Confinement

Langmuir adsorption is one of the earliest models in studying the effect of adsorption on phase behavior, presented by Langmuir (1918). The assumptions of the Langmuir adsorption model include a surface that is flawlessly flat and homogeneous, the adsorbate (gas) being an ideal gas at the considered temperature, and that the adsorbate and adsorbent (surface) are in equilibrium. Additionally, the Langmuir adsorption model is only applicable for systems with a single component adsorbate. Adsorption is more favored at lower temperatures and lower pressures and its application at high pressure and temperature is limited and hardly justified (Langmuir, 1918). The original Langmuir adsorption isotherm is represented by Eq. 1 below:

$$\theta_1 = \frac{\sigma_1 \mu_1}{1 + \sigma_1 \mu_1} \qquad (1-6)$$

θ_1 is defined as the fraction of the site to which adsorbed molecules are attached, $\sigma_1$is a measure of adsorbed molecule bond to the surface (expressed as gas pressure (p) in later references), and μ_1 is the rate at which a gas condenses on an uncovered surface (known as Langmuir constant (b) after him).

Brunauer-Emmett-Teller (BET) theory is considered as an extension of the Langmiur theory, which is a theory for monolayer molecular adsorption. BET aims to explain the multilayer adsorption by assuming that gas molecules physically adsorb on a solid surface in infinite layers, there is no interaction between each adsorption layer, and Langmuir theory is applicable for each (Brunauer et al., 1938).

Schettler et al. (1989) studied the amount of producible gas from several Devonian shale samples as a function of the external pressure of methane. Results indicated that the sample pore volume is much less than the amount of methane extracted from the sample. In addition, the curvature of the isotherms was too large, and curved in the wrong direction. It was concluded that the volume of methane in the sample and the curvature of the isotherm line could not be explained satisfactorily by only considering sample porosity. Conducting several degassing studies, they

proved that the primary contributor of production in Devonian shale is desorbed gas, mainly methane, and that needs to be considered in any simulation or modeling of shale reservoirs.

Ambrose et al. (2011) applied the Langmuir adsorption isotherm to estimate gas in place in shale reservoirs considering a multicomponent reservoir fluid. In this study, they determined the composition and amount of the adsorbed phase by extending the Langmuir model to application in a multicomponent system and taking into account the effect of volumetric/free gas as well as the amount of sorbed-gas[1]. This model overcame the simplicity of the original Langmuir model by considering different contributions of the different components of a gas mixture in the total amount of sorbed gas and phase densities using the total gas in place formulation. However, this model does not account for the other limitations of the use of the Langmuir adsorption isotherm. As stated by Jin and Firoozabadi (2016), the possibility of multilayer adsorption occurrence in nanoscale pores and the likelihood of capillary condensation and hysteresis in small pores because of confinement limit its applicability under those conditions. They suggested the following adjustment to Langmuir equation to overcome these limitations:

$$\theta_{excess} = \frac{pb}{1+pb}\left(1 - \frac{\rho_B}{\rho_{ads}}\right) \qquad (1-7)$$

Where, θ_{excess} is the excess amount of adsorbed phase whose density is ρ_{ads} (density of adsorbed phase) and ρ_B is the density of bulk fluid phase.

Adsorption of different hydrocarbons on solid surfaces has been studied by many scholars in different disciplines throughout the years. The earliest experiments in this area were conducted by McGonigal et al. (1990) and Castro et al. (1998) who managed to capture a direct image of an alkane layer on graphite (alkane-graphite interface) using a scanning tunneling microscope.

Recently, Wang et al. (2015) applied Molecular Dynamics (MD) simulation to investigate the adsorption of hydrocarbons in nanoscale pores of unconventional systems. This study reveals that multiple layers of adsorbed gas and liquid hydrocarbons always exist in confined pore spaces. The number of these adsorbed layers significantly depends on the slit size and the composition of the oil or gas. Heavier hydrocarbons show more propensity for adsorption. Therefore, the thickness of the adsorbed layer depends largely on the relative proportion of light and heavy hydrocarbons. On average, there are three or four adsorbed layers in the half-length of an organic slit, and the thickness of each layer is around 0.48 nm.

In dry gas shale reservoirs, adsorption is known as one of the storage mechanisms which is almost 45% of initial gas storage; this amount in liquid rich shales is decreased to 5-13% of total liquid in place (Rajput, 2014).

Adsorption can be either physical (physisorption) in which molecule-wall bonds are weaker (like van der Waals) or it can be chemical adsorption (chemisorption) in which stronger

[1] Total gas in place in shale reservoirs consists of volumetric gas in place which is stored in pore spaces and is referred as free gas component. This gas is mixed with the sorbed gas in shale; however, the effect of it needs to be separated in total gas estimation based on adsorption model.

bonds (valence bonds) are formed and the chemical nature of adsorptive is altered by a surface dissociation or reaction.

From the physical point of view, adsorption is the development of a phase with a considerably higher density inside the pores of adsorbent material. In gas condensate reservoirs, adsorption is similar to the condensation phenomena of gas inside the pores which is also affected by capillary effect (capillary condensation).

Adsorption mainly relies on the properties of the adsorbent. Adsorbent phase density is an important parameter in determining the total adsorption capacity of an adsorbent. Several assumptions have been made to capture density effect. One of the common assumptions is to consider the density of the adsorbed phase to be the same as the liquid density. This assumption, however, fails to explain excess adsorption beyond critical point where there is no gas. It means density of the adsorbed phase -which for CO_2 was tested by Sircar et al., (1971) is greater than liquid saturation density. Another approach is using molecular simulation to capture the density effect in such tiny pores. However, almost none of them have been successful in giving accurate data and most of them show a large variation in adsorbed gas density on different adsorbents. Some of these results are summarized by Ngo, and is presented in the following table (Ngo, 2015):

Table 1.1. Density of adsorbed gases reported by different scholars using different approaches, gathered by (Ngo, 2015).

Adsorbed Fluid	Reference	Adsorbent materials	Adsorbed Density (g/cm^3)	Range of CO_2/CH_4 (g/cm^3)
CH_4	Ambrose et al. (2012)	Graphite	0.34	0.2-0.78
	Haydel et al. (1967)	Silica Gel	0.37	
	Mavor et al. (2004)	Coal	0.42	
	Rolniak et al. (1980)	Zeolite 13X and 5A	0.16-0.32	
	Moffat et al. (1955)	Carbon Black	0.23	
	Gasparik et al. (2012)	Shale	0.2-0.64	
	Gasparik et al. (2013)		0.53	
	Gasparik et al. (2014)		0.42-0.78	
	Moghaddam et al. (2013)		0.19	
	Rexer et al. (2014)		0.76	
	Rexer et al. (2013)		0.26	
	Tan et al. (2014)		0.3-0.5	
CO_2	Melnochenko et al. (2006)	Silica Aerogel	1.07	0.35-1.25
	Di Giovanni et al. (2001)	Silica Gel	1.09	
	Radlinski et al. (2009)	Coal	0.20-0.60	
	Fitzgerald et al. (2005)		1.40	
	Weniger. P et al. (2012)		0.93-1.49	
	Steriotis el al. (2004)	Activated Carbon	0.52-0.59	
	Humayun and Tomasko (2000)		1.01-1.04	
	Sudibandriyo et al., 2003		0.99	
	Van Hemert et al. (2009)		0.99	
	Pini et al. (2006)		1.05	
	Gensterblum et al. (2009)		0.95-1.01	
	Weniger et al. (2010)	Shale/Clay	0.79-1.08	
	Chareonsuppanimit et al. (2012)		1.25	
	Busch et al. (2008)		0.84-1.2	
	Jeon et al. (2014)		0.35-0.84	
	Gao et al. (2004)	NAY Zeolite	0.8-1.3	
	Hocker et al. (2003)	Zeolite 13X	1.59-1.75	
	Pini (2014)		1.14-1.23	
	Steriotis el al. (2002)	Carbon slit-pore	0.57-0.75	
	Kurniawan et al. (2006)		0.88	
	Liu and Welcox (2012)		0.81-0.90	

On the other hand, most of these studies agreed that the amount of excess adsorption goes up with increasing pressure. It means aside from the calculated adsorbed amount, there will be an excess amount of adsorbed phase due to high pressure. This excess amount may be calculated as below (Ngo, 2015):

$$m_{excess} = m_a \left(1 - \frac{\rho}{\rho_a}\right) \qquad (1-8)$$

Where, m_{excess} is the excess amount of adsorbed gas whose density is ρ_a and ρ is the bulk density.

Although the amount of adsorption in shales is still a dilemma, there is no doubt that strong interactions between fluid molecules and solid constituents elevates the amount of adsorption and due to the relatively large amount of such tiny pores, adsorption attribution is a considerable portion of the storage capacity of such rocks.

Chapter 2: Thermodynamics Principle Applied in Solving This Problem

Thermodynamics is a branch of science which relates system behavior to measurable properties of that systems such as pressure and temperature. From thermodynamics point of view, a phase is a part of a system with uniform physical and chemical properties. In a system, multiple phases can coexist under equilibrium.

The distribution of different components among phases that coexist is addressed under thermodynamic relationships. One of the fundamental relationships in thermodynamics which is used to study phase equilibrium by presenting the concept of chemical potential is Gibbs free energy relationship (Firoozabadi, 2016):

$$G = G\left(P, T, n_1, n_2, \dots, n_{n_c}\right) \qquad (2-1)$$

$$dG = -SdT + VdP + \sum_{i=1}^{n_c} \mu_i dn_i \qquad (2-2)$$

Where G is the Gibbs free energy, P is the temperature (bar), T is the temperature (K), V is the volume (m^3), n_i is the number of moles of component i, S is the entropy (joule/K), and μ_i is the chemical potential of the component i.

Firoozabadi (2016) listed the condition of equilibrium as follows:

- Thermal equilibrium

  Having an isolated system which consists of two subsystems, if the volume of each of them is constant (dV=0, dV'=0), there is no compositional changes in each of them (dn_i=0, dn_i'=0), and the total internal energy of the system is also constant ($d(U + U') = 0$), then the two subsystems are in thermal equilibrium if:

  $$T = T'$$

- Mechanical Equilibrium

  Having an isolated system which consists of two subsystems, if the total volume of the system is constant ($d(V + V')$=0), there is no compositional changes in each of them (dn_i=0, dn_i'=0), and the total internal energy of the system is also constant ($d(U + U') = 0$), then the two subsystems are in mechanical equilibrium if:

  $$T = T'$$
  $$P = P'$$

- Chemical equilibrium

  Having an isolated system which consists of two subsystems, if the total volume of the system is constant ($d(V + V')$=0), there is no compositional changes in the system ($d(n_i + n_i')$=0), and total internal energy of the system is also constant ($d(U + U') = 0$), then the two subsystems are in chemical equilibrium if:

  $$T = T'$$
  $$P = P'$$
  $$\mu_i = \mu_i'$$

It simply means that the flow of components between the two subsystems (two phases) ends up in equality of chemical potentials of the two phases at equilibrium ($\mu_i = \mu_i'$).

Pressure, temperature, and chemical potential are not independent variables. Gibbs-Duhem equation relates these parameters to each other by the following equation (Firoozabadi, 2016):

$$SdT - VdP + \sum_{i=1}^{n_c} n_i \, d\mu_i = 0 \qquad (2-3)$$

Gibbs-Duhem equation for a single component can be rearranged to $d\mu = -sdT + \nu dP$ where s and ν are molar entropy and molar volume. Under constant temperature this equation is reduced to $d\mu = \nu dP$. Integrating over a pressure range from P_0 (reference pressure) to P we have:

$$\mu(P,T) = \mu(P_0,T) + \int_{P_0}^{P} \nu dP \quad \xrightarrow{yields} \quad \mu(P,T) = \mu^0 + RTln\left(\frac{P}{P_0}\right) \qquad (2-4)$$

Note that for an ideal gas the well-known equation of state $PV = nRT$ holds true. Therefore, the above-mentioned calculated chemical potential is valid only for ideal gases.

Gibbs free energy of a single component is $dG_i = \nu dP = d\mu$. So, Gibbs free energy for a single component of an ideal gas can be written as:

$$dG_i = RTd\left(\ln\left(\frac{P}{P_0}\right)\right) \qquad (2-5)$$

Lewis (1901) introduced an extension for Gibbs free energy for non-ideal gases:

$$dG_i = RTd(lnf_i) \qquad (2-6)$$

Where f_i (bar) is a function called fugacity and is defined as effective pressure which replaces the mechanical pressure. The physical meaning of this pressure is defined schematically in Figure 2.1.

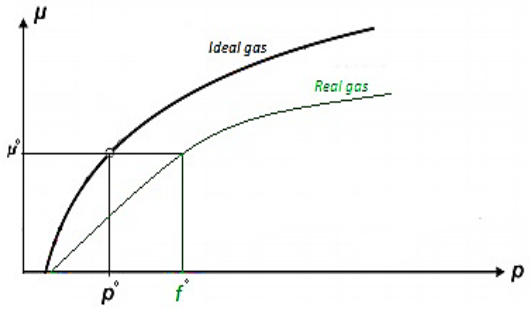

Figure 2.1. Chemical potential as a function of pressure for ideal gas (top curve) and real gas (bottom) which demonstrate what $f_{i=}\frac{f}{f^0}$ is.

Fugacity coefficient of a component (φ_i) is defined as [Firincigolu, 2013]:

$$\varphi_i = \frac{f_i}{x_i P} \qquad (2-7)$$

Where, x_i is the mole fraction of the gas.

Based on equation 2.6 one can conclude that $d\mu_i = RTd(lnf_i)$. Therefore, under equilibrium the following equations hold true:

Ideal gas $\mu_i = \mu_i'$

Real gas $f_i = f_i'$

Where $\mu_i$and μ_i' are chemical potentials of subsystems (two phases) and $f_i$and f_i' are fugacities of the two available phases.

2.1. Equations of State

Equations of state (EOS) are thermodynamic instruments which are simple ways to interconnect macroscopically measurable properties of a system and calculate pressure, volume, temperature (PVT) of that system (Haider, 2015).

Considering a pressure versus volume plot, as shown in Figure 2.2, an EOS is expected to be representative of the phase behavior of the fluid both inside and outside of the two-phase envelope. As illustrated in the figure, the flatness around the critical point cannot be accurately captured by any of the equations of state.

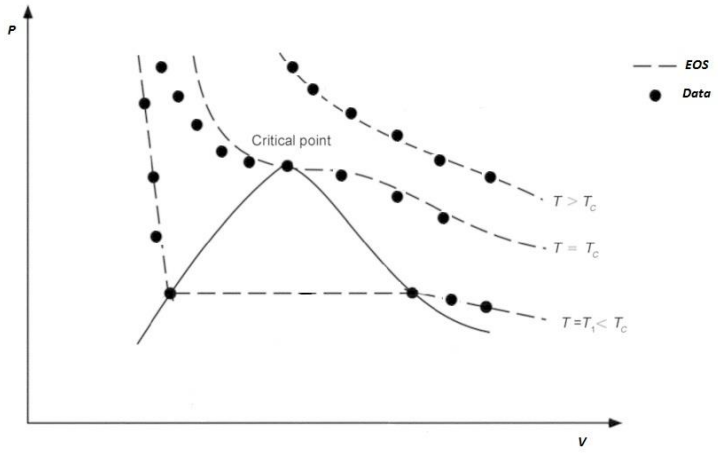

Figure 2.2. EOS representation of P-V diagram for a pure substance

Equations of state are categorized into "cubic" and "non-cubic" equations of state. Cubic EOS may have three roots when $T \leq T_c$, only one root when $T > T_c$, and three equal roots at $T = T_c$. Although non-cubic EOS describe the volumetric behavior of the pure substances, they are not good for complex hydrocarbon mixtures, especially in the critical region (Firoozabadi, 2016).

The most popular non-cubic equations of states are compressibility EOS and the Virial EOS.

2.1.1. Compressibility Equation of State

The simplest EOS for real gases is the compressibility EOS:

$$PV = ZnRT \qquad (2-8)$$

In which, Z is the compressibility factor which is an indication of real gas behavior from ideal gases. Using this EOS, the task becomes to find Z-factor knowing that it should be equal to unity for ideal cases.

2.1.2. The Virial Equation of State

The virial formulation defines the compressibility factor (Z) as an infinite power series of V_m, which is molar volume of the gas, as follows:

$$pV_m = RT\left[1 + \frac{B}{V_m} + \frac{C}{V_m} + \cdots\right] \qquad (2-9)$$

Where *B, C, D,…* are the virial coefficients, functions of temperature and composition.

The virial EOS has a good theoretical connection with the interaction potentials; which means, the second virial coefficient (*B*) represents binary interactions between particles, the third one (*C)* is representative of ternary interactions between the particles, and so on.

Coefficients come from fitting isothermal volumetric data into the truncated version of the virial expansion.

2.1.3. Van der Waals Equation of State

Van der Waals EOS is derived by considering intermolecular interactions in a system consisting of vapor and liquid in equilibrium where the general equation is:

$$\left(P + \frac{a}{{V_m}^2}\right)(V_m - b) = RT \qquad (2-10)$$

Where, V_m in the molar volume (V/n) and parameters a and b are Van der Waals constants having clear physical meaning:

$$a = \frac{2\pi C}{(n-3)\sigma^{(n-3)}}$$

$$b = \frac{2}{3}\pi\sigma^3$$

Where, σ is the molecule size (so-called hard sphere diameter), n is an integer, and C is a constant.

For a system of real fluids in engineering applications, the parameters a and b are calculated by considering the critical-point conditions to the EOS as:

$$\left(\frac{\partial P}{\partial V_m}\right)_{T=Tc} = \left(\frac{\partial^2 P}{\partial V_m^2}\right)_{T=Tc} = 0$$

Therefore, a and b parameters can be calculated as follows:

$$a = \frac{27\,R^2(T_c)^2}{64\quad P_c}$$

$$b = \frac{RT_c}{8P_c}$$

Where, T_c and P_c refer to critical temperature and critical pressure.

2.1.4. Soave-Redlich-Knowng Equation of State

Redlich and Kwong (RK) (1949) made an important modification to attractive term (relating it to temperature) of the van der Waals EOS by proposing the following equation:

$$\left[P + \frac{a}{T^{\frac{1}{2}}v(v+b)}\right](v-b) = RT \qquad (2-11)$$

Later, Soave made a significant improvement to the Redlich-Kwong equation of state by replacing the temperature in the attraction term by a more general function α. Hence, the Redlich-Kwong EOS is written as:

$$P = \frac{RT}{V_m - b} - \frac{a\alpha}{V_m(V_m+b)} \qquad (2-12)$$

Where,

$$\alpha = \frac{1}{T^{0.5}}$$

Again, parameters a and b might be calculated by setting the first and second derivatives equal to zero at critical point:

$$a = 0.42748\left(\frac{R^2(T_c)^2}{P_c}\right)$$

$$b = 0.08664\frac{RT_c}{P_c}$$

α might be calculated based on Pitzer acentric factor (ω), as follows:

$$\alpha = [1 + (1 - T_r^{0.5})(0.480 + 1.574\omega - 0.176\omega^2)]^2,$$

Where, $T_r = T/T_c$ is the reduced temperature. Although this improvement made Redlich-Kwong EOS more accurate for pure hydrocarbons as well as for hydrocarbon mixture VLE, does not provide reliable liquid density.

2.1.5. Peng-Robinson Equation of State

Another important modification of Van der Waals EOS was made by Peng and Robinson (1976) as follows:

$$\left[P + \frac{a(T)}{v(v+b) + b(v-b)}\right](v-b) = RT \qquad (2-13)$$

This equation improved the liquid density prediction but could not describe volumetric behavior around critical point accurately (Firoozabadi, 2016). Density prediction is the weakness of almost all equations of state.

The Peng-Robinson equation of states (PR-EOS) in terms of gas compressibility factor is written as:

$$Z^3 - (1-B)Z^2 + (A - 3B^2 - 2B)Z - (AB - B^2 - B^3) = 0 \qquad (2-14)$$

Where $A = \frac{aP}{R^2T^2}$ and $B = \frac{bP}{RT}$.

Calibrating the model by laboratory measurements such as Constant Composition Expansion (CCE), Constant Volume Depletion (CVD), separator tests and Differential Liberation (DL), is a general approach to determine EOS parameters which are explored in detail in the next chapter (Firincioglu et al., 2012).

2.2. Vapor-Liquid Equilibrium (VLE)

The first step in VLE studies is defining equilibrium ratio (K_i). In a multi-component system, the equilibrium ratio is defined as the ratio of the mole fraction of a component in gas phase (y_i) to the mole fraction of that component in liquid phase (x_i) (Lake, 1989).

$$K_i = \frac{y_i}{x_i}$$

VLE calculations are useful to define needed parameters to describe the flow in reservoirs, such as bubble point and dew point. Dew point, pressure at which there is infinitesimal quantity of liquid in equilibrium with gas, and bubble point, pressure at which there is infinitesimal quantity of gas in equilibrium with liquid are shown graphically in P-T diagrams (Figure 2.3).

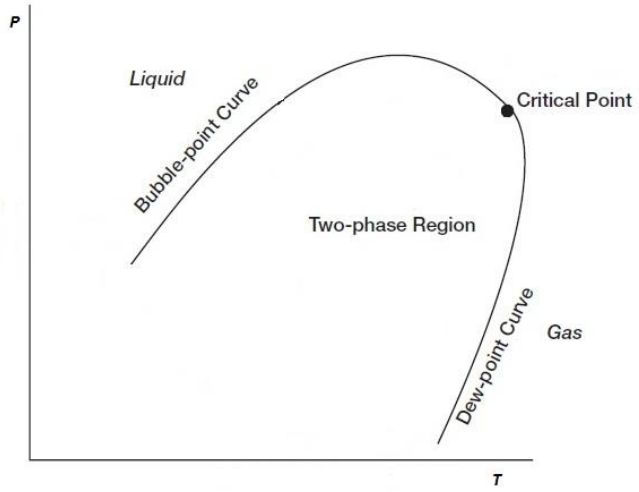

Figure 2.3. A typical P-T diagram (Lake, 1989).

2.3. Classical Thermodynamics for Confined Fluids

The difference between classical thermodynamics for confined fluids and bulk fluids is that for a bulk fluid, surface tension (interfacial tension between liquid-vapor, slid-liquid, or solid-vapor) does not depend on the curvature. In other words, it is the same as planar values. While for the confined fluid this effect is considerable and in the derivation of the equilibrium conditions, the effect of curved interface (curvature effect) needs to be taken into account.

Kelvin equation is widely used to describe VLE at a curved interface. The main assumption of Kelvin equation is that for a pure substance at pressures away from critical point, generally, $\nu_G \gg \nu_L$. Therefore, the equilibrium condition ($d\mu_G = d\mu_L$) for a pure component, using Laplace equation ($P_G - P_L = \frac{2\sigma}{r}$) can be approximated by:

$$\nu_L dP_L = \nu_G dP_G$$

$$dP_G = dP_L + \frac{2\sigma}{r}$$

$$dP_G = \frac{2d(\frac{\sigma}{r})}{1 - (\frac{\nu_G}{\nu_L})}$$

$$\nu_G \gg \nu_L \xrightarrow{yields} -\nu_G dP_G = 2\nu_L d\left(\frac{\sigma}{r}\right) \qquad (2-15)$$

Integrating the above equation from r=∞ (flat interface) to any r (droplet radius) gives us the well-known Kelvin equation:

$$\ln\left(\frac{P_{G,Curv}}{P_{G,flat}}\right) = -2\sigma\frac{\nu_L}{rRT}$$

Sphiro and Stenby (1997) modified Kelvin equation for multicomponent non-ideal mixtures and proposed the generalized Kelvin equation as follows:

$$\frac{P_{G,Curv}}{P_D} = \left(\frac{V_{G,mix}}{V_L} Z_{ave} - 1\right)(x-1) + \frac{V_{G,mix}}{V_L} Z_{ave}(x-1)^2 \qquad (2-16)$$

Where $P_{G,Curv}$ is same as original Kelvin equation, P_D is the dew point pressure, $V_{G,mix}$ is the gas (vapor) volume of the mixture, V_L is the liquid volume of the mixture, Z_{ave} is the average compressibility factor (average gas compressibility between P_B (bubble point pressure) and P_D (dew point pressure)), and $x = \frac{P_B}{P_D}$ is the relative pressure which is the ratio of bubble point to dew point pressure.

As mentioned before, Kelvin equation (both the original and the generalized form) is based on the Young-Laplace equation (also known as capillary approximation). Capillary approximation ($P_G - P_L = \frac{2\sigma}{r}$) neglects compressibility of the fluid which means liquid is considered to have a constant density. In addition, it considers interfaces as fixed surface with an exact location which means the finite size of the interface region is not taken into account.

Another alternative approach to model the fluid behavior in confined space is the use of equations of state. Travalloni et al. (2010a) modified Van der Waals EOS to include the effect of confinement. Their proposed configuration, as shown in Figure 2.4, consists of different regions. Region I is outside of the fluid-wall intermolecular attraction field, hence, only fluid-fluid intermolecular interactions are considered. Region II with width δ_p, however, is where fluid molecules are affected by pore wall molecules and fluid-wall intermolecular forces are effective. Region III is considered as the inaccessible area, with width equal to half of the sphere-shaped molecule diameter, $\frac{\sigma_{dia}}{2}$ (Travalloni et al., 2010a).

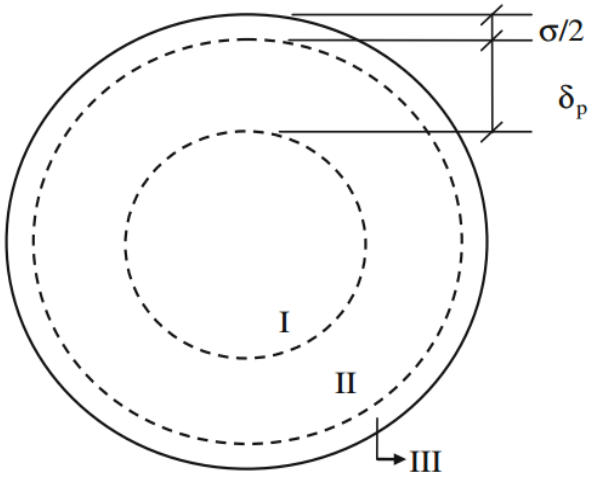

Figure 2.4. Different regions inside a cylindrical pore defined based on molecule-wall interactions (Travalloni et al., 2010a).

The extended Van de Waals equation proposed by Travalloni et al (2010a), is (Travalloni et al., 2010a):

$$P = \frac{RT}{(\nu - b_p)} - \frac{a_p}{\nu^2} - \theta_g \frac{a_p}{\nu^2}\left(1 - \frac{b_p}{\nu}\right)^{\theta_g - 1}(1 - F_{pr})\left(RT\left(1 - \exp\left(-\frac{N_{av}\varepsilon_p}{RT}\right)\right) - N_{av}\varepsilon_p\right)$$

$$(2-17)$$

$$a_p = \sum_{i=1}^{n_c}\sum_{j=1}^{n_c}\left(z_i z_j \sqrt{a_i a_j}\left(1 - \frac{2}{5}\frac{\sigma_{dia,ij}}{r_p}\right)\right)$$

$$b_p = \sum_{i=1}^{n_c} z_i b_{p,i}$$

$$b_{p,i} = \frac{N_{av}}{\rho_{max,i}}$$

Where R (J K^{-1} mol^{-1}) is universal gas constant, T (K) is the temperature, ν (m^3 mol^{-1}) is the average molar volume, θ_g is the geometric term which is a function of r_p, δ_p and $\frac{\sigma_{dia}}{2}$, N_{av} is the Avogadro number, ε_p is the energy parameter of the attractive interaction between two fluid molecules, ρ_{max} is the molecular density of the packed confined fluid, and F_{pr} is the value which shows the fraction of the confined fluid molecules that are subjected to the attractive field of pore wall molecules (Travalloni et al., 2010a).

The above-mentioned extended Van der Waals equation can be written in concise form as follows:

$$P = \frac{RT}{(\nu - b_p)} - \frac{a_p}{\nu^2} - f(r_p, \delta_p, \varepsilon_p)$$

In which the first part ($\frac{RT}{(\nu - b_p)} - \frac{a_p}{\nu^2}$) represents fluid-fluid interaction potentials and the second part ($f(r_p, \delta_p, \varepsilon_p)$) represents wall-fluid interaction potentials.

2.4. Statistical Mechanics

Vanderlick and Davis (1989) first proposed using statistical mechanics to study the behavior of confined fluid. The thermodynamic system consists of a large number of particles which are described by state variables (intensive or extensive) and are used to determine the system's properties in average sense. Statistical mechanics deals with the average behavior of such a system made up of a large number of particles by using probability theory. Statistical thermodynamics (also called equilibrium statistical mechanics) derives classical thermodynamics of materials in terms of properties of their constituent particles considering all the interactions between them. Proceeding with some definitions, we will explore the main equations in statistical thermodynamics (Roque-Malherbe and Roque-Malherbe, 2007).

- Ensemble: is a hypothetical collection of an extremely high number of states that a system could be in. Where, these high numbers of systems represent a wide variety of microstates, each compatible with the given macro-state, statistical mechanics is used to study such ensembles; an infinite number of molecules in a room is an ensemble studied by statistical mechanics.
- Probability distribution: in order to obtain a statistical ensemble which is representative of the real system, it is essential that the occurrence of each state follows an appropriate probability distribution.

$$N = \sum_{i=1}^{\Omega} n_i$$

$$E = \sum_{i=1}^{\Omega} P_i E_i$$

Where N is the number of systems in an ensemble, E is the total energy of the ensemble, n_i is the number of systems in i-th state, Ω is all accessible energy sates for the macro-system, E_i is the energy of given state (for all systems in an ensemble), P_i is probability of finding the system in one of the i-th passible states.

As mentioned before, statistical mechanics deals with probability distribution because it is hardly possibly to determine which system (out of N) is in which state (out of Ω).

- Entropy: is also defined based on the probability of finding the system in one of the possible Ω states.

$$S = -k \sum_{i=1}^{\Omega} P_i ln P_i$$

Where k is the Boltzmann constant.

- Canonical (NVT) ensemble: represent a system which is in thermal equilibrium with a large bath. Hence, the system is at an imposed temperature and volume with a fixed number of particles.

$$P_i = \frac{n_i}{N}$$

$$\sum_{i=1}^{\Omega} P_i = 1$$

$$\sum_{i=1}^{\Omega} P_i E_i = E$$

$$\sum_{i=1}^{\Omega} n_i = N$$

Applying the method of Lagrange multipliers (Appendix A) to the entropy equation with abovementioned constraints, results in the following auxiliary function:

$$f = -k\sum_{i=1}^{\Omega} P_i lnP_i + \alpha\sum_{i=1}^{\Omega} P_i + \beta\sum_{i=1}^{\Omega} P_i E_i \qquad (2-18)$$

Solving $\frac{\partial f}{\partial p_i}$ for the maximum condition gives the following equation:

$$P_i = \frac{\exp(-\beta E_i)}{Z} \qquad (2-19)$$

Where $Z = \sum_{i=1}^{\Omega} \exp(-\beta E_i)$ and $\beta = \frac{1}{kT}$.

Having said that, S can be written in the following format:

$$S = k\beta E + kln(Z) \qquad (2-20)$$

Now, it is possible to define thermodynamic functions with the help of canonical ensemble. Helmholtz free energy can be calculated as follows:

$$A = U - TS \qquad (2-21)$$

Considering that $U = E$ and $S = k\beta E + kln(Z)$, we have:

$$A = -kTln(Z)$$

- Grand potential (Ω): comes from Legendre transformation of Helmholtz free energy and is minimum at equilibrium for an open system (unlike other thermodynamic functions, internal energy (U), enthalpy (H), Helmholtz free energy (A), and Gibbs free energy (G), which are minimum at equilibrium for a closed system).

$$A = \sum_{i=1}^{n_c} \mu_i dn_i - SdT - PdV \qquad (2-22)$$

$$A = A(n_1, n_2, \dots, n_{n_c}, T, V)$$

Applying Legendre transformation (Appendix B):

$$\Omega = -PV \qquad (2-23)$$

$$\Omega = \Omega(\mu_1, \mu_2, \dots, \mu_{n_c}, T, V)$$

- Grand Canonical Ensemble (GCE): represents a system which is in a heat bath at constant temperature and volume but with variable number of particles. In other words, both energy and the particles can flow to and from the bath to the system.

$$S = -k\sum_{i=1}^{\Omega}\sum_{j=1}^{N} P_{i,j} lnP_{i,j}$$

$$\sum_{i=1}^{\Omega}\sum_{j=1}^{N} P_{i,j} = 1$$

$$E = \sum_{i=1}^{\Omega}\sum_{j=1}^{N} E_i(V,j) P_{i,j}$$

$$N = \sum_{i=1}^{\Omega}\sum_{j=1}^{N} jP_{i,j}$$

In order to find the probability distribution, one needs to find maximum entropy first. The method of Lagrange multipliers is used to find the maximum entropy.

$$F = -k\sum_{i=1}^{\Omega}\sum_{j=1}^{N} P_{i,j} lnP_{i,j} + \alpha\sum_{i=1}^{\Omega}\sum_{j=1}^{N} P_{i,j} + \beta\sum_{i=1}^{\Omega}\sum_{j=1}^{N} E_i(V,j)P_{i,j} + \gamma\sum_{i=1}^{\Omega}\sum_{j=1}^{N} nP_{i,j} \qquad (2-24)$$

$$\frac{\partial f}{\partial P_{i,j}} = -klnP_{i,j} + 1 - \alpha + \beta E_i(V,j) + \gamma j = 0$$

Consequently:

$$P_{i,j} = \frac{\exp[-\beta E_i(V,j)]\exp[-\gamma j]}{\Theta}$$

$$\Theta = \sum_{i=1}^{\Omega}\sum_{j=1}^{N} \exp[-\beta E_i(V,j)]\exp[-\gamma j] = \sum_{j=1}^{N} Z(j)\exp[-\gamma j]$$

Where $Z = \sum_{i=1}^{\Omega}\exp[-\beta E_i]$ is the canonical partition function, $= \frac{1}{kT}$, and $\gamma = -\frac{\mu}{kT}$.

Again, entropy can be re-written as:

$$S = -k\beta\mu N + k\beta E + kln(\Theta)$$

Therefore, Helmholtz free energy can be expressed as:

$$A = \mu N - kTln(\Theta)$$

With these introductory definitions we can proceed to one of the widely used approaches in statistical mechanics called density functional theory (DFT).

DFT is a powerful mathematical approach to describe both structural and thermodynamic properties of fluids from the molecular perspective. It is equally useful for the bulk and inhomogeneous systems and accounts for intermolecular forces and at the same time it is computationally efficient (Berlin, 2009).

Van der Waals was the first who postulate that molecules distribute continuously in the heterogeneous region and proposed that the density number of molecules ($\rho(r)$) is a function of the position r at the interface:

$$X = \int \rho(\vec{r})x(\vec{r})d\vec{r}$$

Where X can be any extensive thermodynamic function (entropy, internal energy,…).

Because entropy s(r) and internal energy U(r) are not measurable and there is no general expression for them, an equivalent function (A(r)) which depends on only measurable variables for a closed system is used in variational principle of equilibrium. Therefore, for a closed system at fixed temperature and volume, the distribution of molecules minimizes the Helmholtz free energy:

$$A = \int \rho(\vec{r})a(\vec{r})d\vec{r}$$

Calculus of variations (Appendix C) considering the mass conservation in a closed system as a constraint gives us:

$$\frac{\partial A}{\partial \rho(\vec{r})} - \mu = 0$$

Where μ is the Lagrangian multiplier arising from mass conservation constraint in the closed system.

Generally speaking, the simplest part of a dynamical system is a particle which moves in a 3D space and can be specified by its position ($\vec{r}$(x,y,z)), velocity ($\dot{\vec{r}}$), acceleration ($\ddot{\vec{r}}$), etc. There are various dynamical systems to describe mechanical problems. The most popular one in Newtonian system which is a rectangular coordinate and a particle is specified in it by its position over the time ($\vec{r}$(t)). In Newtonian system, a particle can follow any path based on its original position and imposed velocity and acceleration and this path is specified by (t, $\vec{r}$(t), $\dot{\vec{r}}$(t)).

Another dynamical system to describe mechanical movement of a particle is Lagrangean. Lagrangean approach is based on the variational principle. The underlying idea is that "nature tries to minimize something". Therefore, a particle in Lagrangean systems moves along the minimum period:

$$\vartheta(\gamma) = \int_{t_1}^{t_2} \mathrm{L}\left(\mathrm{t}, \vec{r}(\mathrm{t}), \dot{\vec{r}}(\mathrm{t})\right) dt$$

$$D\big(\vartheta(\gamma)\big) = 0$$

Where D is the derivative with respect to any admissible path (γ).

The third dynamical system to specify the mechanical approach of a particle is the Hamiltonian. Hamiltonian formulation, in fact, brings the conservation of energy into the dynamical system; which means that if a Hamiltonian function does not depend on time, then its value (its energy) is constant. Hamiltonian formulation depends on momentum of the particle instead of its velocity vector which makes it useful for molecule or atom systems for which finding the velocity vector is not easy. For a classical system of N particles, Hamiltonian is:

$$H_N = KE + \varphi + U_{ext} \qquad (2-25)$$

$$H_N = \sum_{i=1}^{N} \frac{p_i^2}{2m} + \varphi(\overline{r_1}, \overline{r_2}, \dots, \overline{r_N}) + \sum_{i=1}^{N} U_{ext}^{i}\,(\overline{r_i})$$

Where KE is the kinetic energy, ϕ is the potential energy and U_{ext} is the external potential. P_i is the momentum of the particle i, m is its mass, $\varphi(\overline{r_1}, \overline{r_2}, \dots, \overline{r_N})$ is the total intermolecular potential, and U_{ext}^{i} is the one-body external potential. So, $U_{ext} = \sum_{i=1}^{N} U_{ext}^{i}\,(\overline{r_i})$.

Using GCE probability equation, the probability of finding a Hamiltonian system in one of the possible states can be expressed as:

$$P_N(H_N) = \frac{\exp[-\beta H_N]\exp[-\gamma N]}{\Theta} \qquad (2-26)$$

Where $= \frac{1}{kT}$, $\gamma = -\frac{\mu}{kT}$, and Θ is the grand canonical partition function ($\Theta = \sum_{i=1}^{\Omega} \exp[-\beta H_i]\exp[-\gamma N]$).

Therefore;

$$\ln(P_N) + \ln(\Theta) = \frac{-H_N + \mu N}{kT}$$

$$kT\ln(P_N) + H_N = \mu N - kT\ln(\Theta) = A$$

As mentioned before, Helmholtz free energy (A), can be expressed as a function of $\rho(r)$:

$$A[\rho(\overline{r})] = KE + \varphi + kTln(P_N)$$

Where $\rho(\overline{r}) = \overline{\rho}(\overline{r})$ at equilibrium ad there is no external potential U_{ext}.

At equilibrium and in the presence of an external potential U_{ext}- for example when the fluid in confined in a pore and there is an adsorption field happening there- grand potential ($\Omega = A - \sum_{i=1}^{n_c} \mu_i n_i$) can be expressed as follows (using Legendre transformation):

$$\Omega[\rho(\overline{r})] = A[\rho(\overline{r})] - \int \rho(\overline{r})u\,(\overline{r})d\overline{r}$$

Where, $u(\overline{r}) = \mu - U_{ext}(\overline{r})$.

For a classical thermodynamic system consisting of N particles, the equilibrium density $\overline{\rho}(\overline{r})$ is determined using Euler-Lagrange equation (Appendix D). Therefore, the equilibrium density is the function which makes $\Omega[\rho(\overline{r})]$ a minimum.

$$\frac{\delta\Omega[\rho(\overline{r})]}{\delta\rho(\overline{r})} = 0$$

Where, $\frac{\delta}{\delta\rho(\overline{r})}$ is the functional derivative. Combining the above-mentioned equation with $\Omega[\rho(\overline{r})] = A[\rho(\overline{r})] - \int \rho(\overline{r})u\,(\overline{r})d\overline{r}$ one obtains:

$$\frac{\delta\Omega[A(\overline{r})]}{\delta\rho(\overline{r})} = \mu - U_{ext}(\overline{r}) = u(\overline{r}) \qquad (2-27)$$

Which is the minimum condition that helps in determining the equilibrium density (Roque-Malherbe and Roque-Malherbe, 2007).

The Helmholtz free energy used in the above-mentioned calculations is named “intrinsic Helmholtz free energy” by Ruthven (1984).

Chapter 3: Confined Fluid Phase Behavior Experiments and Models

3.1. Conventional Experimental Methods

Conventional PVT tests that are commonly conducted in the laboratory to study fluid phase behavior, are normally done by placing the target mixture in a PVT cell with a typical volume of around 100 cc. Some of these cells have a transparent window to make it possible to visualize phase separation and all of them represent bulk phase behavior. The most common tests are:

- Flash Vaporization (Constant Composition Expansion or CCE)
- Differential Liberation
- Constant Volume Depletion (CVD)

The experimental details associated with these tests are briefly explained here (McCain, 2010):

3.1.1. Flash Vaporization (CCE)

This experimental procedure is also known as flash liberation, flash expansion or PV relation (Figure 3.1). As the name suggests, a known mass of reservoir fluid is placed in a laboratory cell, the overall composition of the reservoir fluid or its original mass remains constant and the thermal environment is also maintained constant at reservoir temperature throughout the experiment. Theoretically, the pressure condition set should be approximately that of initial reservoir pressure. CCE tests are conducted to study the PV relationship of a given fluid and determine the saturation pressures.

A single-phase sample is initially brought to reservoir pressure or a pressure slightly above the initial reservoir pressure while temperature is constant at reservoir temperature. After stabilization of pressure and temperature, pressure depletion is commenced, hence, the oil volume increases.

Periodic agitation of the fluid is needed to prevent the phenomenon of supersaturation, or metastable equilibrium, where a mixture remains as a single phase even though it should exist as two phases. Upon completion of the test, pressure-volume data are plotted and the pressure at which the slope changes is considered as the bubble point pressure of the mixture at the given temperature. The corresponding volume at the bubble point is the saturated volume of the liquid (V_{sat}).

This change of slope happens because as soon as the bubble point is reached, the compressibility of the fluid increases (single phase liquid compressibility is very low), therefore, the same magnitude of reduction in pressure, causes more volume increase in the mixture. In a volatile oil sample, this change of slope is less pronounced than that of a black oil sample.

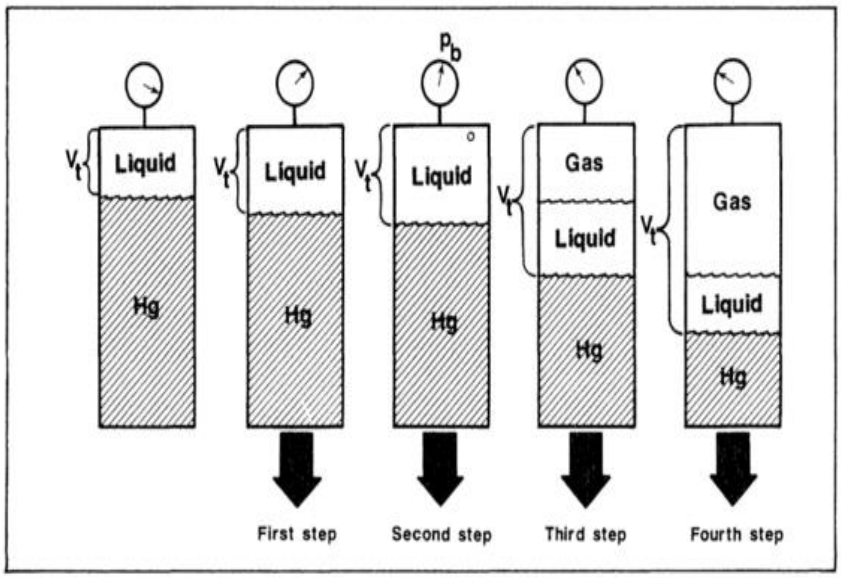

Figure 3.1. Laboratory flash vaporization procedure (McCain, 2010).

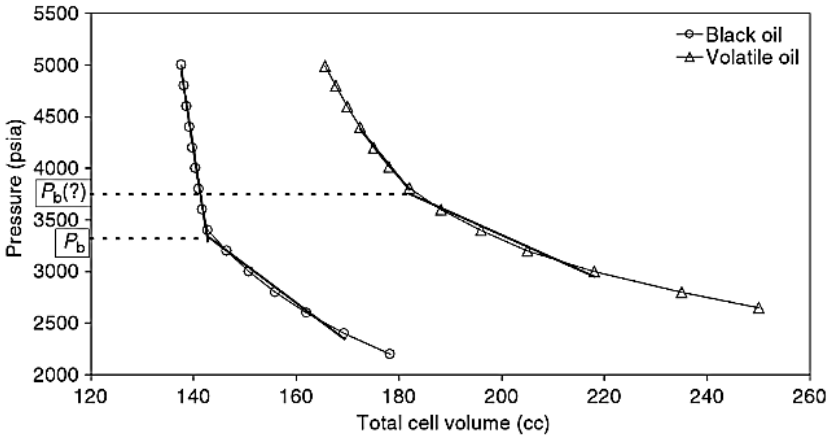

Figure 3.2. P-V behavior comparison in black oil and volatile oil (Dandekar, 2006).

3.1.2. Differential Liberation (DL)

The Differential Liberation (DL) or Differential Vaporization experiment is conducted at reservoir temperature to evaluate compositional and volumetric changes of oil as pressure is reduced.

The sample of fluid is introduced to the laboratory cell as a single phase at reservoir temperature. Pressure is reduced by increasing cell volume until the fluid reaches its bubble point. After agitating the cell to ensure equilibrium between the gas and liquid has reached, all the gas is released from the cell under a constant pressure by reducing the volume.

The volume of liquid remaining in the cell, V_o is measured based on the volume of collected gas. The process is repeated in steps until atmospheric pressure is reached. The temperature is then reduced to 60 °F, and the residual oil volume and its specific gravity is measured.

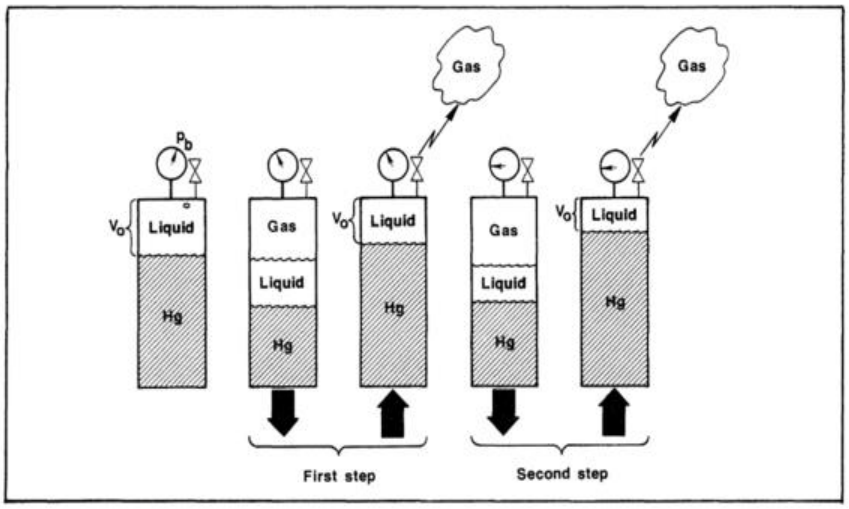

Figure 3.3. Laboratory differential vaporization procedure (McCain, 2010).

The formation volume factors of expelled gas (B_g) and remained oil (B_o) at each stage is calculated. The total amount of gas removed during the experiment shows the solution gas R_s.

3.1.3. Constant Volume Depletion (CVD)

The CVD experiment is performed to provide the volumetric and compositional data for gas-condensate reservoirs producing due to pressure depletion. The test consists of a series of expansions followed by gas removals.

A typical CVD experiment for gas-condensate reservoir is conducted by setting the initial pressure and temperature conditions of the test cell above dew point to start with a single-phase fluid. Next, the pressure is reduced stepwise till it reaches below the saturation pressure of more volatile systems. At some point during the experiment, cell pressure drops into dew point, the volume of fluid at this point is introduced as saturation volume. As pressure drops further below dew point, sufficient volume of gas ΔV_g is expelled from the cell at a constant pressure in order to return the cell volume to the its original saturated volume and keep the volume constant and that is why this test is named constant volume depletion.

The gas released at each stage is brought to atmospheric conditions, and gets analyzed to determine composition, volume, and compressibility factor. Upon termination of the test (after 5 to 10 pressure reduction steps up to atmospheric pressure) the residual liquid in the cell is also analyzed. The amount of liquid dropout in a CVD test is determined at each pressure step by ratio of condensed volume in the cell to the reference volume.

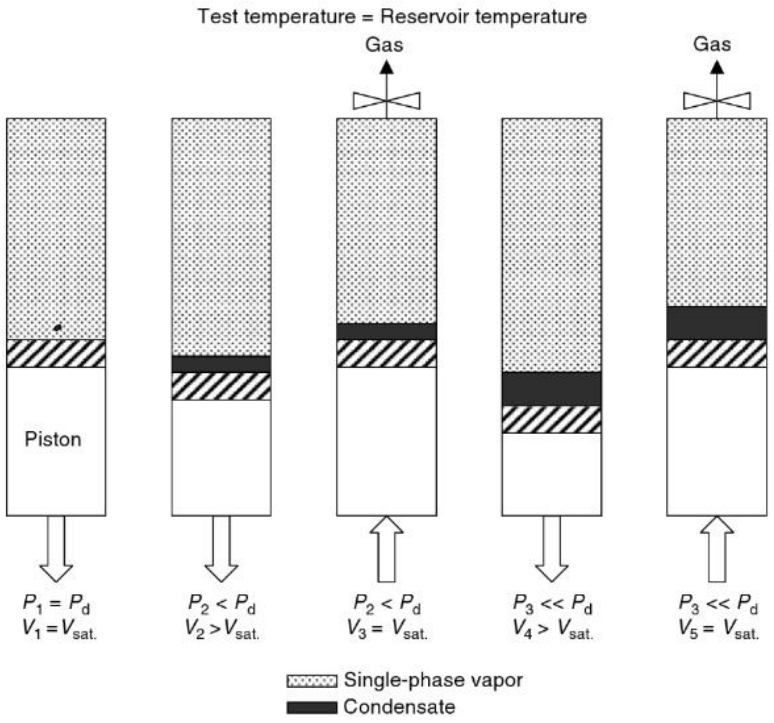

Figure 3.4. Laboratory constant volume depletion procedure (Dandekar, 2006).

3.1.4. Isochoric Approach

Aside from conventional experimental methods which are widely used in PVT studies, there are quiet many experimental approaches for specific needs and conditions. The isochoric VLE method which appeared in literatures back to 1986 is one of the versatile, static, closed-cell methods for fluid two phase behavior studies over wide ranges of pressure and temperature. This method relies on identifying the change in slope of isochoric lines as they cross vapor-liquid phase boundaries.

As discussed earlier, the challenging area of experimental thermodynamics is determining accurate vapor-liquid equilibrium and the isochoric (constant volume) technique appeared to be relatively simple and accurate.

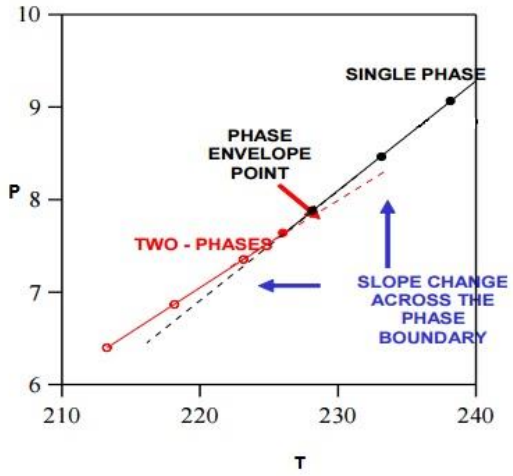

Figure 3.5. Isochoric approach for determining phase boundaries (Mantilla, 2012).

A typical isochoric apparatus is normally a closed isochoric cell made of temperature resistant material which is equipped with a surrounding heat exchange, a temperature control and monitoring system, and a pressure control and monitoring system. The sample is loaded into the isochoric cell at the initial desired condition to be a single-phase liquid or gas. A heat exchanger is used to lower or raise temperature, and pressure is monitored accordingly. After stabilization, pressure and temperature data are collected and analyzed. The P-T data are plotted and the change in slope that happens at one point very close to the phase boundary allows determination of bubble point or dew point as shown in Figure 3.6 (Mantilla, 2012, Velez et al., 2010, Zhou et al., 2006).

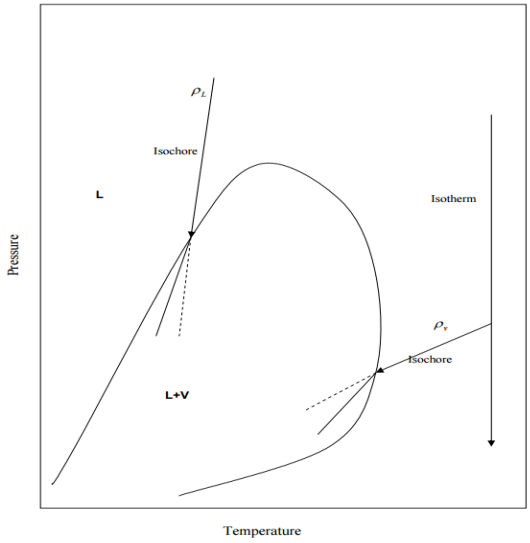

Figure 3.6. Two Phase diagram of a mixture and isochoric lines (Zhou et al., 2006).

3.2. Existing Models to Describe Confinement Effect on Phase Behavior

3.2.1. Theoretical Studies

Unconventional reservoirs exhibit complex phase behavior during depletion of reserves. This complexity associates with the loss of valuable condensate fluid in reservoirs, or

misestimating the production, which makes it more important to achieve a good understanding of the fluid phase behavior and properties. Accurate prediction of reservoir performance requires investigating the effect of porous media on phase behavior.

The earliest experimental and theoretical studies to investigate the effect of porous media on phase behavior dated back to the 1960s and 1970s, long before all this attention towards shale reservoirs being started. These studies predicted that higher dew point pressure values measured in porous media could be in the order of 10 to 15% more than that measured in a conventional PVT cell (Tindy and Raynal, 1966), (Sigmund et al.), (Alfred Chatenever; John C. Coulhan, 1952). Almost all of these experiments agreed that the phase behavior of a fluid system in a porous media packed column is entirely different from the PVT cell which is free of porous media. Attempts to improve the understanding of fluid phase behavior under confinement continued through the development of new methods for measuring porosity and surface area. The amount of free molecules (free hydrocarbons in place) can be calculated from total porosity, while the amount of dissolved or adsorbed hydrocarbons is mostly related to the surface area of pores (Li et al., 2014).

Many theoretical and modeling studies were published in the past decade simulating the effect of pore geometry and pore size on phase behavior. One of the earliest attempts to model fluid behavior in narrow pores using classical thermodynamics was done by Peterson et al. (1986). The Density profile and grand potential of the fluid (Argon-CO_2) were examined by varying the pore radius under different conditions using Mean Field Theory (MFT). They observed that gas-liquid transition occurs at pressures below the bulk fluid vapor pressure in all cases. For a fixed temperature, the gas/liquid coexistence curve was shortened with decreasing pore radius. They also found that the strength of fluid-wall forces has a great impact on phase transition.

Zarragoicoechea and Kuz (2004) illustrated, referencing older single-component experimental data, that there is a difference between the phase behavior of confined fluids and bulk fluids. They showed that, to properly take into account the behavior of confined fluids, the critical properties of the components should be altered as a function of the ratio of the molecular size to the pore size. The contradiction between EOS simulations and experimental data was initially investigated by Singh et al. (2009). They conducted a Monte Carlo simulation in order to explore the effect of nano-confinement on a number of thermophysical properties including vapor-liquid surface tension of methane, ethane, propane, n-butane, and n-octane in bulk and slit pores of graphite and mica surfaces. Results of this study show that the shift in critical temperature depends on the nature of the surface and the shift in critical pressure depends on the pore size which continuously increases as a result of pore size reduction and becomes almost constant eventually for pore sizes less than 3 nm. However, the critical density demonstrates fluctuation with a decrease in the pore size. Calculated surface tension of the bulk n-alkanes in mica and graphite slit pore systems with pore size diameters ranging from 0.8 nm to 5 nm were sensibly in agreement with experimental data illustrating that vapor-liquid coexistence characteristics (saturated densities and vapor pressures) are less sensitive to the surface characteristics (material and nature of the surface and surface tension) at the smaller pore width and are suppressed mostly because of the confinement.

Travalloni et al. (2010a) suggested that as the pore size becomes smaller, normally for pore-to-molecule size ratio lower than 20, the thermo-physical and dynamic properties of confined fluids may deviate considerably from those measured in bulk fluid. They also quantified the changes in the critical pressure and described these variations using trigonometric functions of the pore diameter. They used an extension of the van der Waals theory to include the impact of confinement on the equation of state (EOS) calculations. Devegowda et al. (2012) pointed out that alteration in fluid properties and transport in nano-pores can be attributed to the limited number of molecules present in these pores and to the interaction between the molecules itself (van der Waals interaction) and between the molecules and pore surfaces. Didar and Akkutlu (2013) conducted Monte Carlo simulation to explore the effect of nano-confinement on the critical properties of methane. Results of their study indicate that as the pore size decreases, critical pressure and temperature of methane also decrease. They also observe that in a slit-pore of 3-nm width, lighter components occupy the more central layers and heavier ones are more inclined to form layers along the walls.

Danesh et al. (1991) conducted a survey to evaluate the reliability of ten equations of state in predicting the phase behavior and volumetric properties of hydrocarbon fluids in conventional PVT cells. In conventional phase behavior studies, in order to evaluate the phase behavior of a reservoir fluid, especially in compositional reservoir simulators, cubic equations of state (EOS) are employed. Peng Robinson EOS is precise in describing the phase behavior and properties of bulk hydrocarbons but it is inapplicable in small pores (Li et al., 2014). Li and Firoozabadi (2009) proposed an engineering version of the density functional theory (DFT[2]) which was applied to extend PR-EOS for heterogeneous, non-uniform molecular distribution. Later, in another study by Li et al. (2014), DFT was applied to predict the adsorption of fluid in nanoscale porous media. They reported for the first time that phase change due to capillary condensation could occur beyond the cricondentherm in nano-pores even when the bulk fluid is still in single phase.

Although the amount of produced liquid at dew point in constant volume depletion modeled by EOS with shifted critical properties is much less than that without considering the effect of confinement, Jin and Firoozabadi (2016) indicated that applying EOS with shifted critical properties "violates chemical equilibrium between the fluids in the pores". The results from this study demonstrate an increase in the upper dew point and a decrease in the lower dew point and bubble point pressures with decreasing pore size for pores larger than 10 nm and smaller than 100 nm.

The approach used by Jin and Firoozabadi (2016) to investigate the effect of nano-confinement using DFT is a combination of classical thermodynamics for pores greater than 10

[2]Statistical thermodynamics from molecular point of view is needed to understand the fluid behavior in micropores. Density functional theory (DFT) and grand canonical Monte Carlo (GCMC) are two statistical approaches commonly used in micropores which are applicable for both pure substances and mixtures JIN, Z. & FIROOZABADI, A. 2016. Thermodynamic Modeling of Phase Behavior in Shale Media. *SPE Journal,* 21**,** 190-207.

nm and statistical thermodynamics[3] for pores smaller than 10 nm. They also used the "solid solution model" to consider the effect of species dissolution in kerogen. The results of their study show that for pore sizes above 10 nm, surface adsorption is negligible while the effect of curvature is considerable, density profile is homogenous, and equations of state with shifted critical properties are accurate in predicting the elevated liquid dropout resulting from interface curvature. Both critical pressure and temperature of confined fluids in pore sizes less than 10 nm decrease as the pore size is reduced, which means that as the pore size decreases, "the properties of confined fluids approach the bulk". This is in contradiction with the prediction by Singh et al. (2009) about the continuous increase in the downward shift of the critical pressure of confined fluids due to reduction of pore sizes; while the critical temperature shift follows more than two paths and the reduction of critical temperature stops below a specific pore radius. Jin and Firoozabadi (2016) also concluded that in pores less than 10 nm, strong fluid/surface interactions are controlling factors of phase behavior, hence, surface adsorption is important, and the fluid density profile is inhomogeneous. This means that density cannot be considered as a constant value and the equation of state, even with adjusted critical properties, cannot be used to accurately predict the fluid phase behavior.

In the following sections, we dive further into fundamentals and details of EOS and MD methods applied by different scholars in studying this effect.

3.2.2. Equations of State Methods

Equations of state (EOS) are thermodynamic instrumentals which are simple ways to interconnect macroscopically measurable properties of a system and calculate its pressure, volume, and temperature (PVT) (Haider, 2015). Equations of state are categorized into "cubic" and "non-cubic". Cubic EOS may have three roots when $T \leq Tc$, only one root when $T > Tc$, and three equal roots at $T = Tc$. Although non-cubic EOS describe the volumetric behavior of the pure substances, they are not good for complex hydrocarbon mixtures especially in the critical region (Firoozabadi, 2016). The most popular non-cubic equations of state are compressibility EOS and the Virial EOS and the most popular cubic EOS in modeling fluid phase behavior are Van der Waals EOS and Peng-Robinson EOS. As mentioned earlier, the heterogeneity in fluid density due to fluid molecule interactions with pore walls in tight formations makes equations of state inaccurate for fluid phase behavior prediction under confinement and raises the need for modifying the original form to account for the effect of confinement.

The proposed approach for generalizing van der Waals equation of state in nano-pores by Zarragoicoechea and Kuz (2002), assumed that pores have squared cross section and walls are inert. This means although they did find a good match between the shift on critical properties as a function of pore size and the experimental data, the interactions between fluid and pore walls were ignored in their model (Zarragoicoechea and Kuz, 2002).

Zarragoicoechea and Kuz (2004) also utilized the generalized van der Waals equation of state to derive an equation for the shift in critical properties of the confined fluid compared to the

[3] The cut-off point for sorption diffusion is considered 50 nm by Etminan et al. (2014), and 10 nm by Jin & Firoozabadi (2016).

bulk values. This general relation between the thermal shift and dimensionless length of the pore space was in agreement with some experimental data that they used. This relation is shown in Figure 3.7 (Zarragoicoechea and Kuz, 2004).

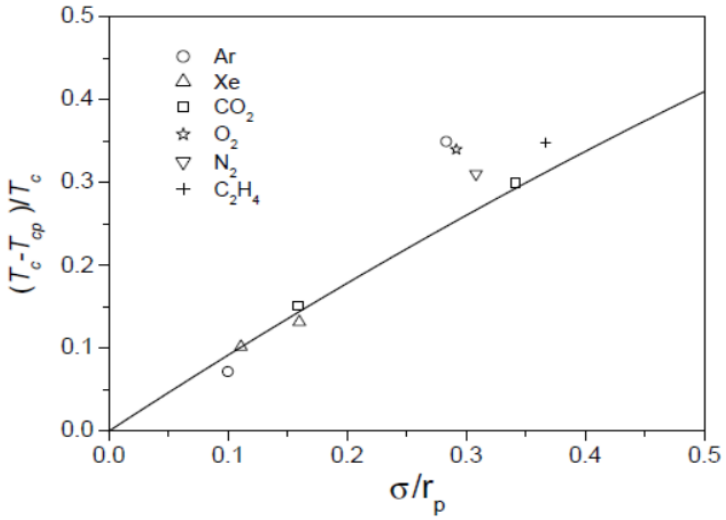

Figure 3.7. This figure shows the shift on the critical properties as a function of the size of the pore[4]. Full line represent the equation derived for the shift in critical properties of confined fluid compared to bulk values[5] and symbols are experimental data (Zarragoicoechea and Kuz, 2004).

Travalloni et al. (2010) suggested an extension of van der Waals EOS in which the effects of pore size and interactions between fluid molecules and pore walls were considered as below:

$$P = \frac{RT}{(v-b_p)} - \frac{a_p}{v^2} - f\left(r_p, \delta_p, \varepsilon_p\right) \qquad (3-1)$$

In which the first part, which is the original van der Waals EOS ($\frac{RT}{(v-b_p)} - \frac{a_p}{v^2}$), represents fluid-fluid interaction potentials and the second part, ($f(r_p, \delta_p, \varepsilon_p)$), represents wall-fluid interaction potentials.

In this model, original van der Waals assumption of considering fluid molecules as hard spheres was combined with assuming adsorbent pores as cylinders with a fixed radius and validity of this model was tested using available adsorption data of pure fluids at low pressures. Figure 3.8

[4] σ is Lennard-Jones size parameter and r_p represents the pore radius.

[5] This equation was derived from relationship of temperature shift and size ratio given by Evans et al. ($\frac{(T_c-T_{cp})}{T_c} \leq \frac{\sigma}{r_p}$) [Evan EVANS, R., MARCONI, U. M. B. & TARAZONA, P. 1986. Capillary condensation and adsorption in cylindrical and slit-like pores. *Journal of the Chemical Society, Faraday Transactions 2: Molecular and Chemical Physics,* 82**,** 1763-1787.].

represents the correlation between results of their study and experimental data (Travalloni et al., 2010b).

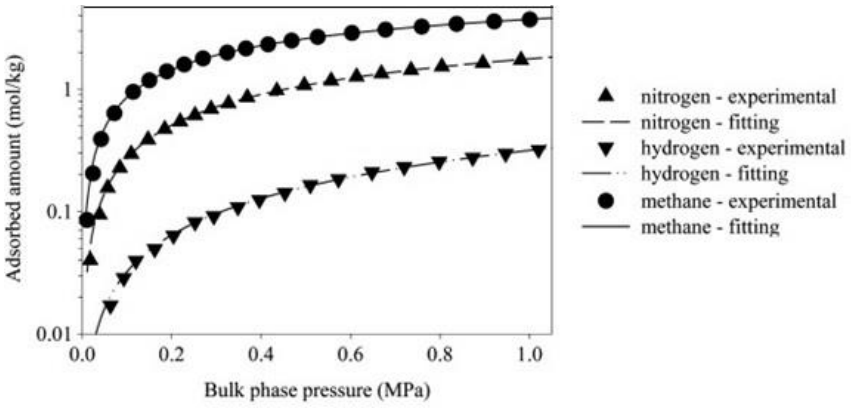

Figure 3.8. Comparison between the generalized van der Waals model and experimental adsorption data for pure gases (Travalloni et al., 2010b).

In another study, they employed the same model to study the critical behavior of a confined fluid and managed to predict either one or two critical points. They conclude that in the case of existence of two critical point, one is attributed to molecule-molecule interactions while the other one is attributed to molecule-wall interactions. The critical density of confined fluid as a function of pore size demonstrated that as the pore size increase, only one of this critical points reaches the bulk value and the other one gradually fades away which means one of this point is predicted for bulk fluid while the other one shows the contribution of adsorption (Figure 3.9) (Travalloni et al., 2010a).

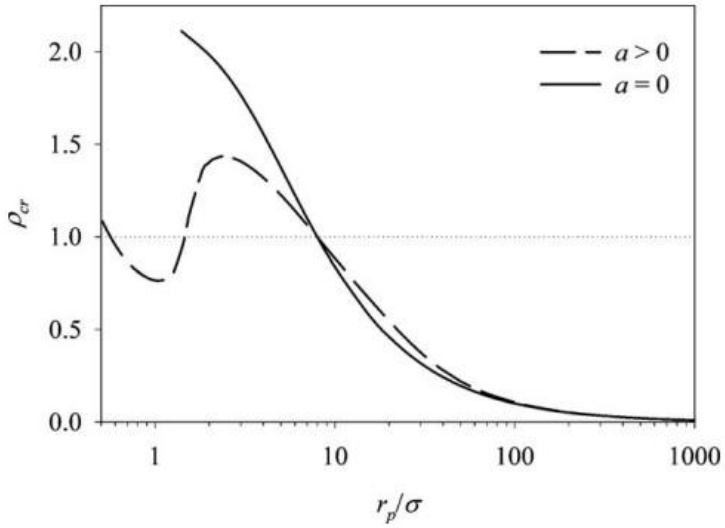

Figure 3.9. Reduced critical densities of confined N_2 as a function of pore radius, with and without adsorption (Travalloni et al., 2010a).

(Ma et al., 2013) modified van der Waals equation of states to make it work for all ranges of pore spaces, from bulk to confined fluids. One term was added to the original van der Waals EOS as a representative of fluid molecules-solid wall interactions:

$$P = \frac{RT}{(v-b)} - \frac{a}{v^2} + \frac{c}{v^2} \qquad (3-2)$$

In which $\frac{c}{v^2}$ represents fluid molecule and pore wall interactions. Figure 3.10 is the representation of the shift in critical temperature as a function of pore diameter

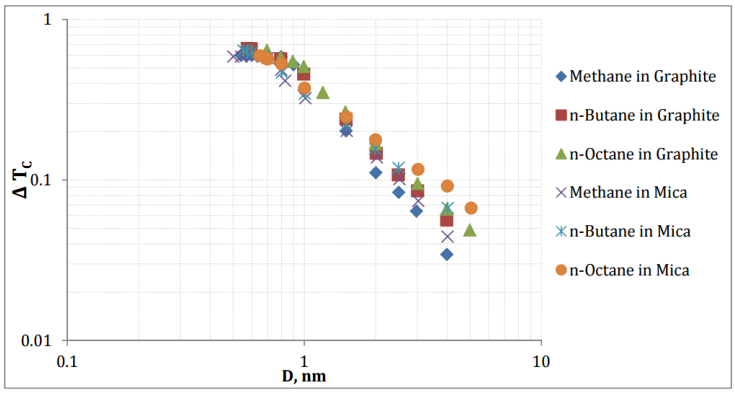

Figure 3.10. The effect of decreasing pore size on critical temperature shift (Ma et al., 2013).

Considering a synthetic mixture of methane (75 mole%), n-butane (20 mole%) and n-octane (5 mole%), they also generated phase envelops for the mixture in different pore sizes using modified van der Waals EOS. As illustrated in Figure 3.11, critical properties of the confined fluids are continuously reduced with the reduction of pore size (Ma et al., 2013).

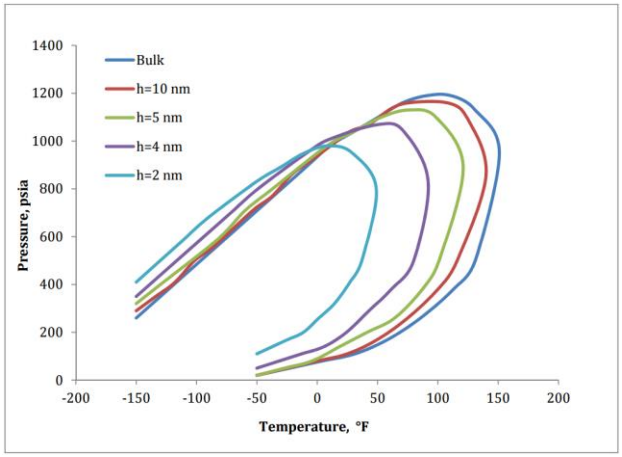

Figure 3.11. Two-phase envelop for a mixture of C1, n-C4, and n-C8 in different pore sizes (Ma et al., 2013).

However, the effect of short-term repulsive interactions between fluid molecules and wall was ignored. To investigate the effect of pore size, as what Singh et al. (2009) did in using Monte Carlo simulation, (Ma et al., 2013) studied the shift in critical behavior of fluid under confinement. They defined the shift of the critical properties of the confined fluid as below:

$$\Delta P_c = \frac{P_{cB} - P_{cP}}{P_{cB}} \qquad (3-3)$$

$$\Delta T_c = \frac{T_{cB} - T_{cP}}{T_{cB}} \qquad (3-4)$$

Where P_{cB} and T_{cB} are critical properties of the bulk phase, and P_{cP} and T_{cP} are the critical properties of the confined phase.

Tan and Piri (2015), employed Perturbed-Chain Statistical Associating Fluid Theory (PC-SAFT) combined with the Young-Laplace equation to investigate the fluid phase behavior in nano-pores. In this study, they believed that molecular approaches are sophisticated and at the same time not considerably applicable to real systems, so they applied PC-SAFT which is a widely used EOS to describe fluid behavior under confinement. PC-SAFT, which is based on the thermodynamics perturbation theory and Helmholtz energy calculations, is free of the drawbacks of other cubic EOS and, at the same time, is computationally less sophisticated than DFT or molecular dynamics (MD). The PC-SAFT/Laplace method they used in this study applies only to the phase transition which occurs in the confined pore space but it does not take into account the adsorption effect which occurs prior to the condensation (Tan and Piri, 2015). The results of this study also confirmed the decreasing shift in the critical properties of a confined fluid compared to those of a bulk fluid.

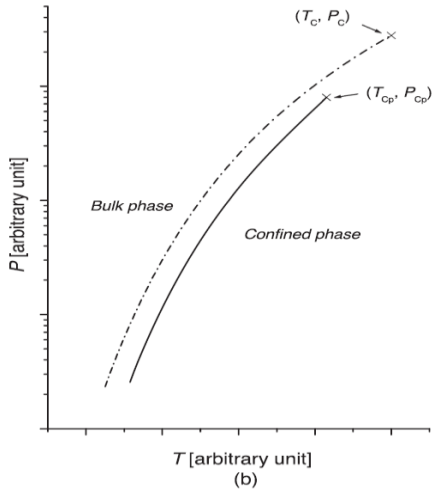

Figure 3.12. P vs T diagram of pure confined fluid using PC-SAFT/Laplace method (Tan and Piri, 2015).

In this study, equilibrium pressures under confinement were also modeled. These equilibrium pressures have negative values for small pore spaces and are positive only in sufficiently large pore spaces at high temperature (Figure 3.13).

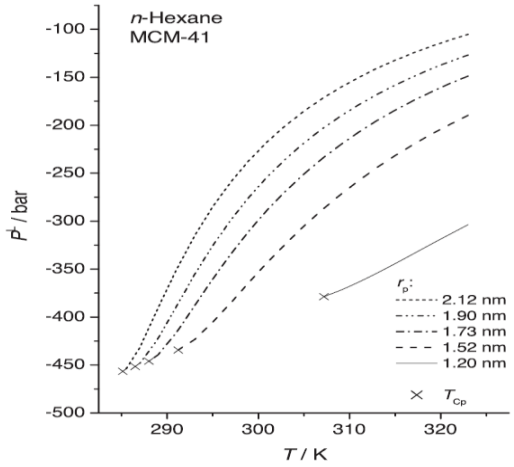

Figure 3.13. P vs T diagram of saturated pressures of the pure n-hexane in MCM-41 (porous medium) (Tan and Piri, 2015).

A recent study by Dong et al., Peng-Robinson equation of state is combined with the capillary pressure equation and adsorption theory to investigate the fluid phase behavior of pure components and mixtures in cylindrical nano-pores. In order to take the effect of adsorption into account, an improved form of Young-Laplace equation is used:

$$P_c = \frac{2\sigma}{r}\, cos\theta \qquad (3-5)$$

To improve the Young-Laplace equation for very small pores and take the effect of interface curvature into account, σ was defined as below:

$$\sigma = \frac{\sigma_\infty}{1 + 2\frac{\delta}{r_e}} \qquad (3-6)$$

Where, $\sigma_\infty$is the flat surface tension of the fluid and δ is the Tolman's length. Tolman's length measures the extent of deviation in surface tension value for a small droplet from planar surface. If we consider the radius of curvature as *R* and the pressure difference between inside and outside of the droplet $(P_l - P_v)$ as ΔP, Tolman's length can be calculated using the following formula:

$$\Delta P = \frac{2\sigma}{R}\left(1 - \frac{\delta}{R} + \cdots\right) \qquad (3-7)$$

Results of Dong et al. study, are then validated using experimental data of Eagle Ford oil.

Based on results of this study, adsorption increases both the VLE constant (K-value) and capillary pressure of the confined fluid. This deviation in actual K-value compared to the calculated one becomes more significant as the pore radius decreases. For the studied Eagle Ford oil, bubble point pressure decreased and dew point pressure, on the other hand, increased as a result of reducing pore sizes. Also, results show that neglecting the effect of adsorption results in overestimating bubble point pressure and underestimating the dew point one.

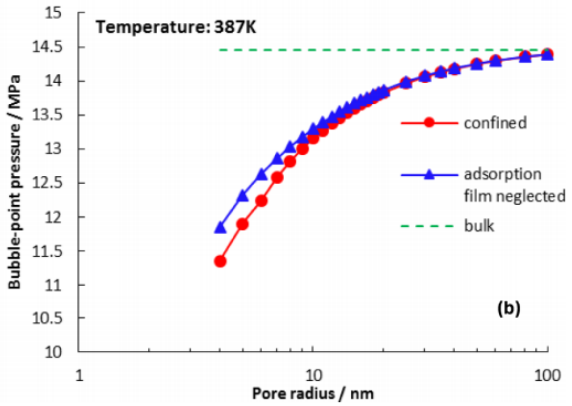

Figure 3.14. The effect of adsorption on bubble point determination for both bulk and confined (in an 8 nm pore) fluid (Dong et al., 2016).

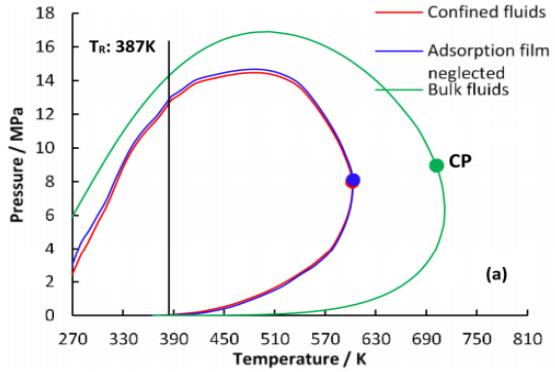

Figure 3.15. The effect of adsorption on the phase diagram for bulk and confined (in an 8 nm pore) fluid (Dong et al., 2016).

3.2.3. Molecular Simulations Methods

As discussed earlier, one of the key features of confined fluids in nano-pores is an inhomogeneous density distribution and a significant effect of fluid molecules-walls interactions. One accurate way to explore the density distribution of fluid molecules inside a small pore space is through the use of Density Functional Theory (DFT). DFT is a very effective approach in analyzing the behavior of an inhomogeneous fluid in any system with any size. Inhomogeneity is a crucial property of any confined fluid, which is a result of the increase in the interactions between fluid molecules and pore walls, leading to a variable density distribution of the fluid. There exist several approaches to approximate DFT such as local density approximation (LDA), weighted density approximation (WDA), modified mean approximation (MMF), fundamental theory (FM), etc. The key assumption of DFT which makes it a suitable tool for statistical thermodynamics is that using DFT, all thermodynamic functions of this system can be represented as integral functions of its density profile.

One of the earliest attempts to model fluid behavior in narrow pores using classical thermodynamics was done by Peterson et al. (1986). The Density profile and grand potential of the fluid (Argon-CO_2) were examined by varying the pore radius under different conditions using

Mean Field Theory (MFT). They observed that gas-liquid transition occurs at pressures below the bulk fluid vapor pressure in all cases. For a fixed temperature, the gas/liquid coexistence curve was shortened with decreasing pore radius. They also found that the strength of fluid-wall forces has a great impact on phase transition.

Kamalvand et al. (2008) conducted a theoretical study on the effect of nano-silt pores on the behavior of confined fluid. They employed fundamental-measure density-functional theory (FM-DFT) to investigate the phase behavior of confined fluids from the molecular point of view. The aim of choosing FM-DFT was to develop a density profile for hard-sphere molecules with various sizes inside a nano-pore. Results of this study show that the density of confined fluids practically approaches its bulk value with decreasing the pore width (Kamalvand et al., 2008).

Peng and Yu (2008), also applied density functional theory (DFT) for a theoretical description of fluid behavior under confinement. They explored surface tension, adsorption and phase transition of a fluid in silt-like pores using MMF-DFT. All of the modeling in this study is based on Lennard-Jones fluid and the results indicate that critical temperature decreases with narrowing the pore sizes. Density profiles provided in this work also illustrate that the density of the liquid phase starts going up again and reaching the bulk value by decreasing the pore size under a specific range (Peng and Yu, 2008).

Singh et al. (2009) conducted a Monte Carlo simulation to investigate a number of thermophysical properties including vapor-liquid surface tension of methane, ethane, propane, n-butane, and n-octane in bulk and silt pores of graphite and mica surfaces. Measured surface tension of the bulk n-alkane in this study was sensibly in agreement with the previous experimental data. They concluded that vapor-liquid coexistence characteristics are less sensitive to the surface characteristics at the smaller pore width and are strangled under confinement (Singh et al., 2009).

Li & Firoozabadi (2009) employed the DFT approach in combination with Peng Robinson equations of state (PR-EOS) to explore the interfacial tension of some pure substances and binary mixtures under confinement. In order to describe the inhomogeneity of the interface, they used the weighted density approximation (WDA) method of DFT. The most significant result of their study was the density profiles of volatile components which represents a higher density of volatile components in the interfacial layer compared to the adjoining bulk phases (Li and Firoozabadi, 2009).

Li et al. (2014) applied DFT to investigate adsorption and phase behavior of both pure substances and their mixtures in nanopores. This study presented the effect of pore size on the adsorption and desorption behavior C_1 and n-C_4 at a temperature of 303.15 K. For C_1, there is no hysteresis[6] because the critical temperature is much lower than 303.15 K. However, for n-C_4 hysteresis (capillary vaporization) moves to lower pressure with reducing the pore size, as illustrated in Figure 3.16 (Li et al., 2014).

[6] Adsorption and desorption pathway is different within a capillary from the outside. This deviation which happens due to non-uniformity of pores is called hysteresis.

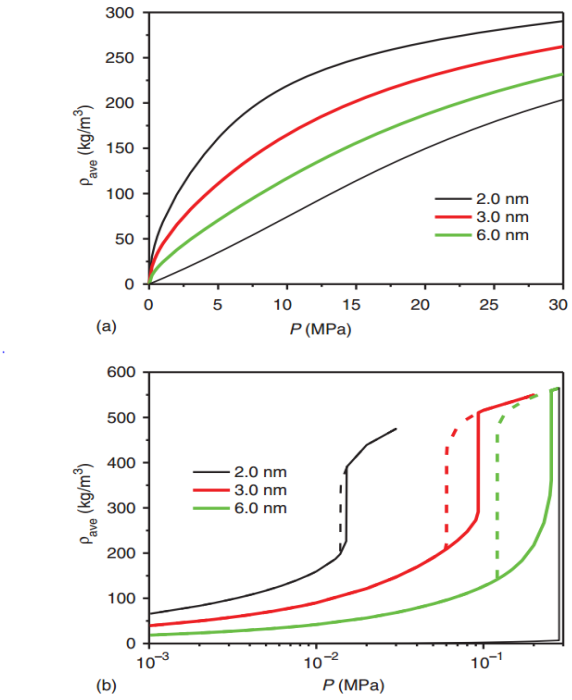

Figure 3.16. The effect of pore sizes on adsorption in carbon-slit pore at 303.15 K for (a) C1 and (b) n-C4. Solid line represents adsorption and the dashed one represents desorption (Li et al., 2014).

This study also revealed that in smaller pores (less than 10 nm) phase transition takes place below saturation pressure and critical temperature (Figure 3.17).

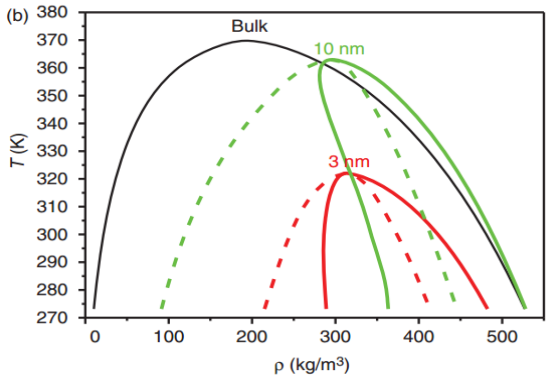

Figure 3.17. The effect of pore sizes on phase transition in carbon-silt pore. Solid line represents adsorption and the dashed one represents desorption (Li et al., 2014).

Another feature of this study is that it provides a P-T diagram for a C_1/C_3 mixture, illustrated in Figure 3.18, which shows that although phase transition still occurs in the 10 nm pore, but it cannot occur in the 3 nm pore. In fact, it says that in a 10 nm pore size, there is still a free region near the pore center in which fluid properties are similar to the bulk. However, in the

3 nm one, the connection of two adsorbed regions occurs before the onset of condensation. As a result, the free region disappears.

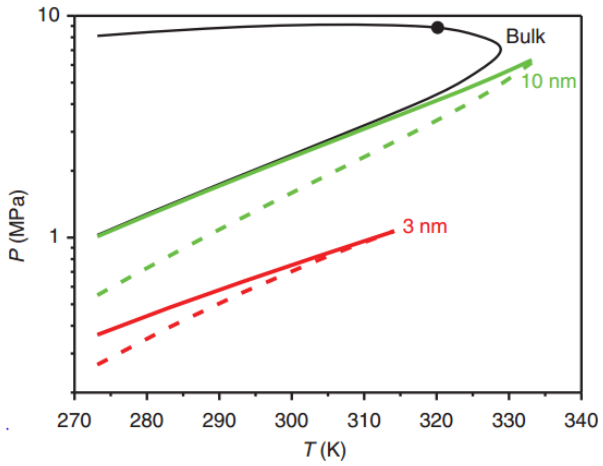

Figure 3.18. P-T diagram showing the effect of pore sizes on metastable phase transition in carbon-slit pore. Solid line represents adsorption and the dashed one represents desorption (Li et al., 2014).

Jin and Firoozabadi (2016) suggested that conventional equations of state such as PR-EOS are useful for describing the phase behavior of fluids in pore sizes larger than 10 nm. The reason is that although in pore sizes less than 10 nm, specifically pores less than 2 nm (micro-pores[7]), saturation pressure of a pure confined component can be reproduced using shifted critical pressure and temperature, densities are considerably underestimated. Hence, densities predicted from PR-EOS using shifted critical pressure and temperature show similar trends as of bulk fluid. However, DFT uses average values of inhomogeneous density of fluid in nano-pores which is significantly lower than that of bulk fluid. Figure 3.19 represents the results of density prediction in 2 nm pore size using both approaches.

[7] Based on IUPAC definition, Micropores have width less than 2nm, Mesopores are in the range of 2-50 nm, and Macrospores are larger than 50nm

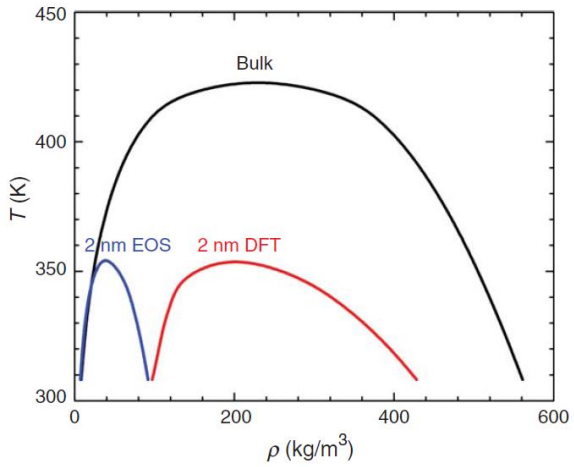

Figure 3.19. Temperature-Density predictions for n-C4 in a 2 nm pore size calculated using both PR-EOS and DFT (Jin and Firoozabadi, 2016).

This study highlights that chemical equilibrium between the fluids inside the small pores, outside fractures, and inside the large pores would be violated by applying an EOS with shifted critical properties; however, this equilibrium is maintained in molecular simulations such as DFT. Nevertheless, as mentioned earlier, their results contradict those of the vast majority of previous studies in which a continuous decrease in critical pressures and temperatures was reported as a result of reduction in pore size (Jin and Firoozabadi, 2016).

Pitakbunkate et al. (2015)studied the changes of PVT properties and phase behavior of pure and binary mixtures of hydrocarbons (Methane and Ethane) under confinement using GCMC (Grand Canonical Monte Carlo) simulation. Results of this study also confirmed changes in critical properties of confined fluids compared to those of the bulk one. These changes in critical pressure and temperature are shown in Figures 3.20 and 3.21 as a function of separation (pore size).

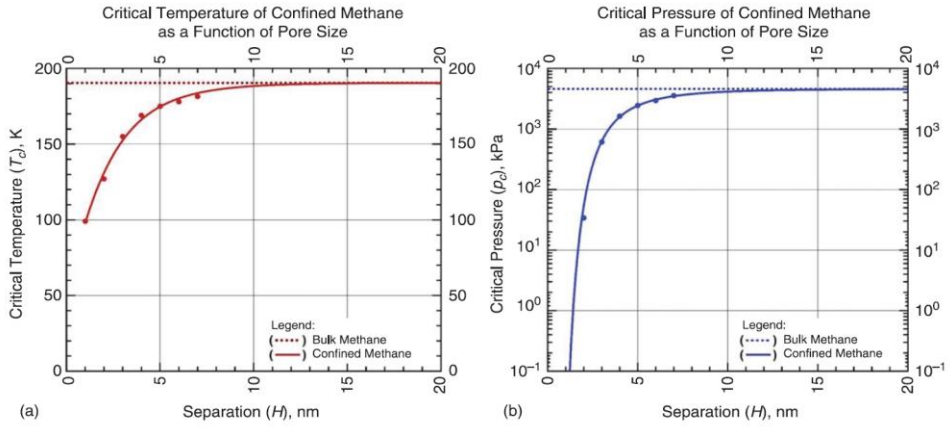

Figure 3.20. Critical temperature (a) and critical pressure (b) of methane as a function of pore size (H) (Pitakbunkate et al., 2015)

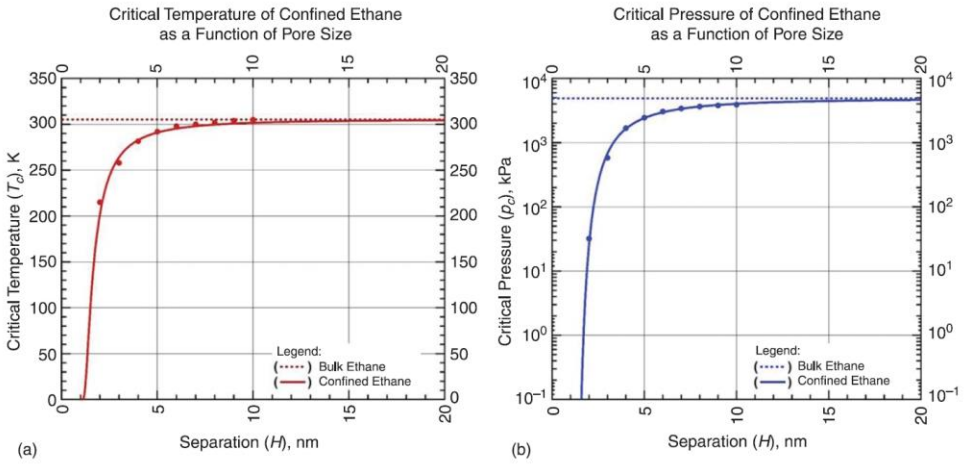

Figure 3.21. Critical temperature (a) and critical pressure (b) of ethane as a function of pore size (H) (Pitakbunkate et al., 2015)

In this study, the phase diagram of a binary mixture of methane-ethane was also simulated under both bulk and confined condition. As illustrated in Figure 3.22, the phase diagram of the binary mixture shrinks as a result of confinement.

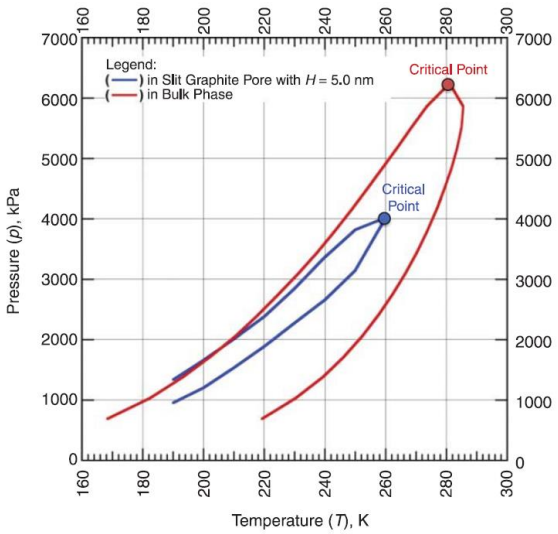

Figure 3.22. P vs T diagram for a binary mixture of methane (30.02%) and ethane (69.98%) in both bulk phase and confined one in separation of 5 nm (Pitakbunkate et al., 2015)

It became evident from the theoretical literature that fluid behavior under confinement has been a controversy among scholars throughout this decade. Although almost of all of them agreed on the different behavior of fluid in nano-pores, there are contradictions and disagreement between the results of different approaches they employed to model this behavior. Lack of experimental data is the main issue in validating these models and results. Some scholars attempted to investigate

this effect experimentally; however, experimental limitations affect most of these studies. We explore some of these experimental studies and their operational limitations in the following section.

3.3. Existing Experimental Studies to Describe Confinement Effect on Phase Behavior

Experiments exploring the effect of porous media on fluid phase behavior can be divided into two main categories, non-visual and visual experiments. Non-visual approaches are those conducted in porous media packed inside metal cells. Visual experiments are those that are accompanied with optic imaging systems and transparent cells, mostly using the Lab-on-a-chip technology.

3.3.1. Non-Visual Experiments

Tindy et al. (1966) conducted one of the first experiments to study the effect of porous media on saturation pressure. They designed a very simple PVT cell, similar to conventional PVT cells, for micrometer to millimeter pore size studies (Figure 3.23). This study intended to explain the probable causes of the difference between the experimental saturation pressure and the real one observed in reservoirs. One of the hypotheses to explain the difference is the influence of the porous medium on the thermodynamic characteristics of a mixture of hydrocarbons (Tindy and Raynal, 1966).

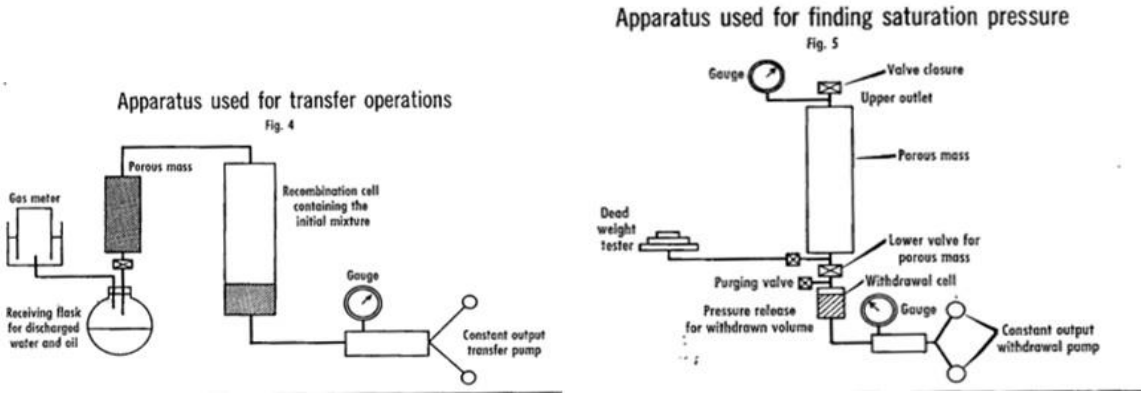

Figure 3.23. Experimental apparatus used by Tindy and Raynal (1966) (top: transferring apparatus, bottom: experimental cell) (Tindy and Raynal, 1966).

In their work, to make sure that the introduced fluid is homogeneous, and no compositional change has occurred during transferring, the mixture was transferred from the combination cell to porous media at a pressure higher than the bubble point. Also, porous media was previously filled with either water or degassed oil. The fluid injection was done from the top and discharge occurred from the bottom of the cell. The speed of liquid withdrawal was adjusted to keep the fluid one phase (5 cc/hr for 2000 cc of mixture). As a result of the experiment, they concluded that the saturation pressures of crude oil in place in porous media are generally above those determined by conventional methods. Also, they found different outcomes for different tests using different compositions; however, the influence of the composition of the fluid was not studied systematically in this work. They also suggested that the grain size of porous media has marked

influence on the capillary phenomena. The composition and characteristics of the media, on the other hand, has influence on the growth of bubbles of gas and adsorption. Their results also showed that the difference of measured saturation pressure is larger for the porous media with larger particle size (Tindy and Raynal, 1966).

Sigmund et al. (1973), investigated the effect of porous media on phase behavior of hydrocarbons using a 32-cm long cell packed with 2.38 mm (diameter) spherical particles. They designed an apparatus to facilitate the comparison of phase behavior in a packed PVT cell with that in conventional PVT cells. They studied the effect of porous media and the influence of interfacial tension on phase behavior experimentally and theoretically. The results of this study which was conducted with the smallest available glass beads at that time, 30-40 U.S. mesh, show that the dew point and the bubble point of the fluid inside porous media are the same as those of the bulk fluid in the absence of porous media. They also studied the effect of curvature on phase behavior using different packing types and interfacial tensions and concluded that this effect is negligible unless the surface curvature is significantly high (radius <10 nm). Although they could not capture the effect of confinement in this study, it was one of the original attempts to appreciate the effect of porous media on fluid properties.

Thommes et al. (1995), investigated the effect of confined geometry on the critical adsorption of a fluid by measuring the physisorption of sulfur hexafluoride (SF6) in a mesoporous controlled-pore glass (CPG) with a mean pore width of 31 nm. The method used for sorption measurement was constant volume (isochoric) measurement of saturation pressure and temperature of the fluid in the cell filled with CPG material versus the one in the other cell with the same size but without any filling material (bulk fluid). Results of these experiments proved that the density of confined fluids decreased because of pore fluid expansion in order to maintain the mechanical equilibrium between the pore fluid and the bulk one. They conclude that this effect strongly depends on adsorption rather than the pore geometry and mostly occurs with adsorbent porous media such as graphitized carbon black and other highly agglomerated colloidal powders. Other experimental studies on the phase behavior of nitrogen, water and carbon dioxide confined in tight spaces also show a significant effect of pore proximity on fluid properties (Arakcheev et al., 2008, Wong et al., 1993, Yusuke and Makoto, 2004).

Luo et al. (2016), used controlled pore-glass (CPGs) with diameters of 38.1 nm and 4.3 nm to model nano-porous media and used octane, decane, and a binary mixture of these two as the hydrocarbon fluid. Differential Scanning Calorimetric (DSC) analysis was employed to observe the effect of pore size on bubble point. DSC technique is usually used to determine thermal properties of materials by comparing the rate of absorption of heat energy into the subjected material with the reference material. Results of this study show that the effect of confinement is negligible in 38.1 nm pores. However, there is a significant change in fluid behavior at the 4.1 nm pore size, bubble point temperature is reduced by 12 K under confinement, also two distinct bubble points are the sign of two populations of evaporating fluid. This conclusion is valid for both pure and binary mixtures of hydrocarbons.

3.3.2. Visual Experiments

The limitations on building a nano-scale porous medium where conclusive results can be obtained directed many scholars to use the Lab-on-a-chip approach for experimental studies of fluid behavior under confinement. Microfluidic devices have been used as a valuable tool of research to study fluid flow and behavior in many other engineering disciplines because it makes it possible to have real time visualization at a small scale. Before visual experiments targeting the study of phase behavior were utilized, many researchers attempted to study the flow in porous media using visual techniques. The goal was to confirm certain theories and/or assumptions as an attempt to explain various macro-scale phenomena and observations. One of the first attempts at such an experiment was conducted in the 1950s.

Chatenever & Calhoun (1952) conducted an exploratory study to visually investigate the fluid behavior in a micro-scale porous medium. The observation apparatus in this study was formed of a single layer of spheres compressed between two flat plates. These single layer of spheres (glass beads with uniform size of 0.007 in) were considered as the porous medium and flat surfaces were used to keep them in place and apply pressure on them. This setup was equipped with a 64 FPS camera to capture fluid flow. These pictures were mainly used for interpreting flow patterns of oil and water. They managed to identify different flow regimes throughout oil and water flooding of the system such as slug flow and channeling effect of water. Figure 3.24 is one of the pictures in which they noticed a perpendicular plane between the spheres. They observed rational movements in the pendular formation (adsorbed phase around particles) and considered these pendular rings as residual oil (Alfred Chatenever; John C. Coulhan, 1952).

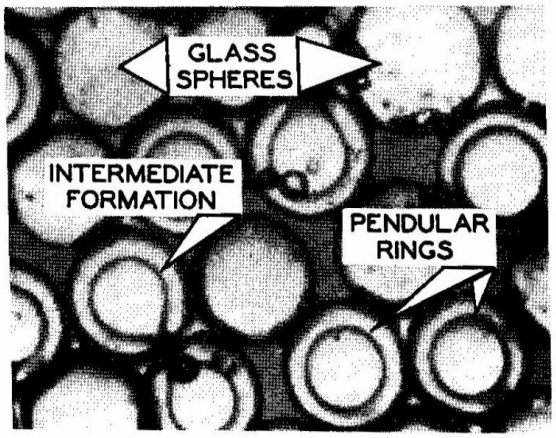

Figure 3.24. Picture of oil/water flow in glass beads medium which shows adsorbed layer of oil around the particles (Alfred Chatenever; John C. Coulhan, 1952).

Lenormand et al. (1983) studied the mechanism of fluid displacement in a transparent microfluidic chip with network patterns. They managed to produce hysteresis profiles to present different phenomena acting at different scales. In this work, different patterns of two phase displacement under different conditions were observed (Lenormand et al., 1983). Feng et al. (2004) studied three phase flow in a glass network micro-model with the minimum pore radius of 5 μm under different conditions. Water Alternative Gas (WAG) displacement was investigated in this

study which proved that mechanism of WAG flow in porous media is much different from that of two phase flow in porous media (Feng et al.). Dawe et al. (2011), studied immiscible displacement of two phases in heterogeneous micro-scale media. They conducted experiments in a rectangular shaped Perspex box which was packed with glass beads with sizes of 300 to 700 µ as heterogeneities. Results of this study indicated that even small heterogeneities in the porous medium can distort the fluid displacement pattern as well as phase saturations (Dawe et al., 2010).

Mostowfi et al. (2012), proposed a novel design for a microfluidic device to ease the process of analyzing phase diagrams of gas-liquid systems by speeding up the equilibrium established in micro-channels. The device consisted of a long serpentine micro-channel with a width of 100 µm and depth of 50 µm, etched on a silicon substrate. To avoid the super-saturation state in the channel, some geometrical restrictions were positioned along the micro-channel to nucleate bubbles. To measure pressure along the channel, they used membrane-base optical pressure sensors placed alongside the channel. This design made it possible to monitor gas bubbles along the tubes and achieve a reduced pressure at the outlet point. The whole setup was equipped with a camera for flow visualization and pressure sensors along the micro-channel. Temperature remained constant to provide the opportunity for measuring the isothermal thermodynamic properties of the mixture. Later, this novel microfluidic design with a width of 114 µm and depth of 57 µm, was used by Fisher et al. (2013) to measure the equilibrium GOR of the reservoirs. Using the long serpentine micro-channels, they managed to monitor fluid flow through micro-channels and identify different flow regimes at different distances from the injection point. These experiments managed to use pressure values as high as 40 bars, however, they were all conducted at room temperature because of the limitation in using the lab-on-a-chip at high temperatures. Results of these studies agreed with the conventional PVT measurements in terms of phase volume distribution (Figure 3.25). The only difference is that the conventional PVT measurements need hours to reach equilibrium while these microfluidic systems make it possible to reach equilibrium in fractions of seconds and can speed up multiphase characterization of systems at equilibrium (Fisher et al., 2013, Mostowfi et al., 2012).

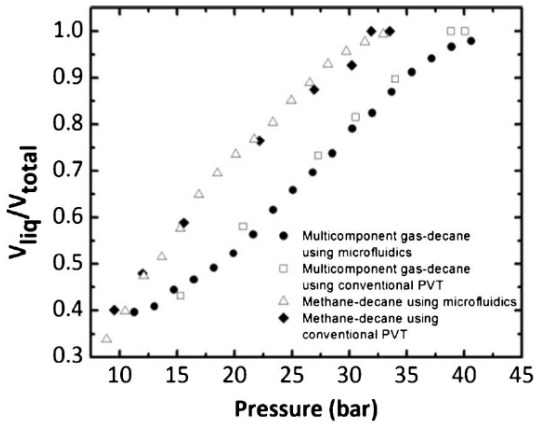

Figure 3.25. Comparison of phase distribution for a multicomponent and a two-component gas mixture using microfluidic and conventional methods (Mostowfi et al., 2012).

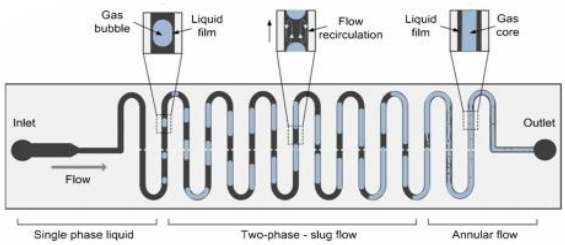

Figure 3.26. Schematic of two-phase flow in a long serpentine micro-channel to observe changes in flow regime (Fisher et al., 2013).

The length of the micro-channel is almost 1 m (can be extended depending on pressure requirements) but because it is fabricated in serpentine form, the length of the microfluidic chip is not exceeding 10 cm.

Wu (2014) studied fluid flow behavior in nanotubes using an optic imaging system. In their design, they added two micro-channels across the nano-channels to control the pressure difference. These micro-channels were also used for fluid injection and, obviously, they were connected to the nano-channels. The micro-channels had equal length in order to balance the pressure drop. The total number of nano-channels located between the micro-channels were 100 and they were arranged in a parallel format to reduce the large hydrodynamic resistance. This study investigated a two-phase system of water and Nitrogen in nano-scale pores under ambient temperature, with a pressure of 15-100 psi. Results of this study presented different observed flow patterns in nano-channels, different water/gas saturation profiles and the extent of capillary effects under these different patterns and saturations in such systems. However, the effect of high pressure and temperature was not considered in this study due to the limitation of the operating conditions that the system could handle.

Pinho et al. (2014), introduced a novel technique to conduct a microfluidic multicomponent phase behavior survey at pressures as high as 200 bar and temperatures up to 500°K. The proposed method was mainly established based on determining bubble and dew point pressure and temperature using optical characterization and using a dynamic stop-flow measurement mode to speed up the investigation of the operating parameters. Phase diagrams and critical locus curves for binary and ternary mixtures were developed as the proof of the concept. In this study, a micro-channel with the total length of 1 m (200 μm width and 100 μm depth) was fabricated based on Mostowfi et al. (2012) established serpentine design. To guarantee mixing quality and fluid temperature, they designed a microsystem with three different zones: inlet-outlet zone, mixing zone and analysis zone. The overall pressure drop was roughly estimated using a Hagen–Poiseuille-based equation (assuming laminar flow in the cylindrical configuration). Multicomponent P–T diagrams were constructed based on bubble and dew point on chip optical detection to determine the phase envelope. At first, a fluid mixture with a particular composition was introduced to micro-channels at equilibrium. Subsequently, under isobaric conditions, temperature was changed to find the bubble and dew points. This process was monitored by visualizing the transitions from the two-phase to the one-phase region. This process was repeated for other pressures till the time maximum cricondenbar point, the maximum pressure of a P–T envelope, was found as demonstrated in Figure 3.27.

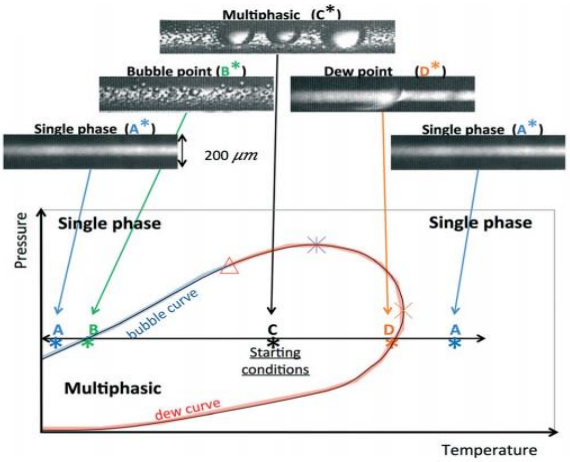

Figure 3.27. General procedure of building a P–T phase diagram through bubble and dew point detection (visualization) and phase envelope construction (Pinho et al., 2014).

As explained above, Pinho et. al used a bypassing line with a larger diameter to have a constant flow and they made the assumption that almost all of the fluid will go through the larger diameter sized tube not the main examination tubes (micro-scale in their study). However, this is a very rough estimation based on Hagen-Poiseuille equation. In real case, particularly in a nanofluidic chip which can be connected to a micro-tube, there always the possibility of having flow in the main tube as well, even in very small amount which can be considerable in nanoscale studies.

Parsa et al. (2015) measured the phase behavior of propane under nanoconfinement using nanofluidic devices. They employed transparent nanofluidic chips with three different channel sizes (two micro-channels and a network of nano-channels in the center same as Wu et al. (2014) design). Experiments were conducted at room temperature to measure the saturation of propane in pore sizes of 500 nm, 50nm, and 30 nm. Results of direct observation of phase change in nano-channels confirms the capillary condensation theory outcome which says vapor pressure (saturation pressure) decreases as a result of decreasing pore sizes (Parsa et al.).

Ally et al. (2016), used a high pressure nanofluidic chip to study the phase behavior of propane and carbon dioxide in a colloidal crystal packed bed. A microchannel packed with beds of silica particles (150 nm in diameter) was used as a porous medium for this study. The fluid was supplied to both ends of the chip simultaneously and the pressure was increased step-wise under ambient temperature. The condensation process was observed visually using a confocal microscope with incident lighting. They experimentally demonstrated that capillary condensation is directly related to the pore size and pore geometry. Results of this study show that capillary condensation happens at higher pressures compared to the calculated dew point pressure in a porous media with an average pore throat size of 17 nm to 33 nm using Kelvin equation for spherical interface. They suggested that this phenomenon not only depends on the hydraulic diameter of the pores, but also it is highly dependent on specific pore geometry and surface properties which are controlling factors for the liquid-vapor interface. This conclusion suggests that aside from pore sizes, differences in geometry and wettability must also be taken into account

when capillary condensation in different media of different materials (glass, shale, sands, spherical packs, and etc.) are compared. Schematic of the experimental apparatus is shown in Figure 3.28.

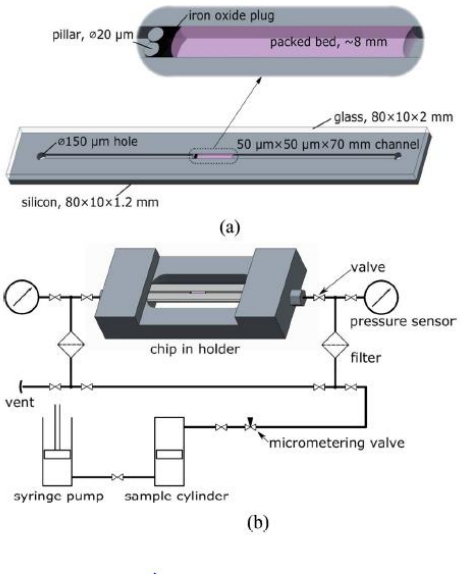

Figure 3.28. Schematic f experimental apparatus used by (Ally et al., 2016).

Lab-on-a-chip technique was employed recently by Alfi et al. (2016) to study fluid phase behavior of some pure hydrocarbon fluids inside nano-channels. Nano-channels with the depth of 50 nm and width of 5 microns were used and the chip was also equipped with thermocouples and a combination of a reverse confocal microscope and a high-speed camera to visualize the fluid behavior inside the channels while controlling the temperature. Fluid was introduced to nano-channels using a syringe pump and temperature was raised gradually at the rate of 12 C/min while pressure was recorded. By visually monitoring the fluid inside the channels using the microscope/camera system, they managed to observe bubble formation and therefore find the corresponding pressure (bubble point pressure). The results of this study for pure hexane, heptane, and octane showed that the there is a good agreement between measured bubble point pressure in 50 nm channels and calculated one using original PR-EOS. It can be concluded from this work that for pore sizes as small as 50 nm, the effect of confinement is negligible and because of that the modified PR-EOS which considers the effect of capillary pressures does not match the experimental data (Figure 3.29).

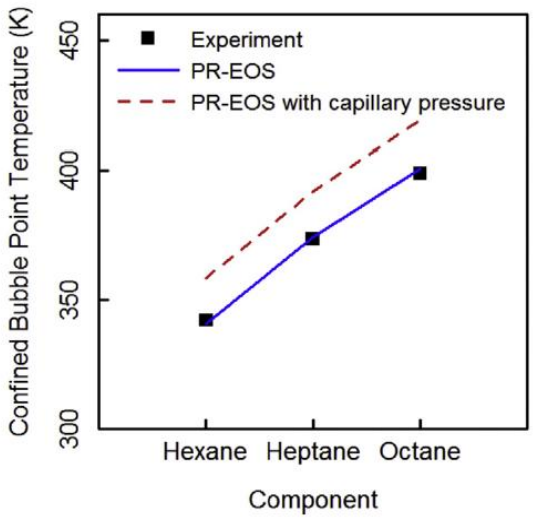

Figure 3.29. Comparison between PR-EOS and experimental results (Alfi et al., 2016).

3.4. Discussions

Shale reservoirs, besides most other unconventional resources, consist of grains with sizes less than 5 microns. Therefore, pores with sizes of 3 nm to 100 nm are abundant in these reservoirs and typical a pore throat diameter distribution is between 0.5 nm and 100 nm. As mentioned in earlier sections, smaller pores (less than 10 nm are referenced by most of the studies) are responsible for deviation in fluid behavior and properties in unconventional reservoirs (Ambrose et al., 2010, Bustin et al., 2008, Sondergeld et al., 2010).

Table 3.1 summarizes the main contributions of scholars toward the simulation and modeling work on the effect of confinement on fluid properties.

Table 3.1. Summary of simulation/modeling works to study the effect of confinement on phase behavior

Reference	Simulation approach	Critical radius[8]	Diagnosed changes with reduction of pore size
Singh et al. (2009)	Monte Carlo (Grand-Canonical Transition Matrix)	0.5- 1.5 nm	Continuous increase in critical pressure shift compared to the bulk value; fluctuation in critical density; critical temperature decreases up to a minimum then it becomes constant
Travalloni et al. (2010a)	Extension of van der Waals EOS	0.5 to 3 times the effective diameter of the	Appearance of two stable critical points in density and temperature profile

[8] Critical radius represents the pore radius below which the changes in fluid behavior and properties happens and above that the behavior and values are the same as those of the bulk one.

		molecule size (depending on the fluid)	
Didar and Akkutlu (2013)	Monte Carlo (NPT-Gibbs & NVT-Gibbs)	3 nm	Decrease in critical pressure and critical temperature
Li et al. (2014)	Density Functional Theory in combination with PR-EOS	10 nm	Phase transition occurs below saturation pressure & critical temperature (capillary condensation)
Ma et al. (2013)	Modified van der Waals EOS	10 nm (in this study, pores between 2 to 10 nm were investigated)	Shrinkage of the two-phase region in phase envelop; continuous increase in bubble- and dew-point pressures (at fixed temperature).
Tan and Piri (2015)	PC-SAFT EOS coupled with Young-Laplace equation	10 nm (only pores less than 10nm were studied in this paper; also, radius of 1.38 nm was introduced as a critical radius below which no phase transition can occur).	Decrease in critical pressure and critical temperature.
Li et al. (2014)	Density Functional Theory (DFT) coupled with PR-EOS	10 nm	Great difference of density profile compared to the bulk; pronounced effect of adsorption.
Jin and Firoozabadi (2016)	Density Functional Theory (DFT) coupled with Monte Carlo (Grand Canonical)	10 nm	Continuous decrease in critical pressure and critical temperature; inhomogeneous density distribution; significant surface adsorption
Dong et al. (2016)	PR-EOS coupled with capillary pressure equation & adsorption theory	20-25 nm (depending on the fluid composition)	Increase in the K-value & capillary pressure; decrease in bubble point pressure & increase in dew point pressure;

Based on the literature and the summary provided in the table above, the need of producing reliable experimental data that would help validate and enhance existing models is evident. Table 3.2 summarizes the most successful attempts in this domain which we explained thoroughly in the previous section.

Table 3.2. Summary of experimental works to study the effect of confinement on phase behavior

Reference	Experimental approach	Experimental pore radius	Diagnosed changes with reduction of pore size
Wu (2014)	Lab on a Chip	100 nm	Two phase flow in nanochannels follow different pattern from the one expected in larger channels; residual gas saturation profiles are altered inside the nanochannels compared to the conventional patterns.
Pinho et al. (2014)	Lab on a Chip	133 µm	-
Parsa et al. (2015)	Lab on a Chip	500 nm 50 nm 30 nm	Capillary condensation (liquification below vapor pressure) happened in both 50 and 30 nm channels; phase transition pressure in 50 and 30 nm channels was lower than the 500 nm one
Luo et al. (2016)	Differential Scanning Calorimetry (DSC)	38.1 nm 4.3 nm	The effect of confinement on bubble point is negligible in 38.1 nm pores; two distinct bubble points diagnosed for the fluid inside 4.3 nm pores and the lower bubble point temperature decreased while the upper bubble point temperature increased.
Ally et al. (2016)	Lab on a Chip (packed beds of silica inside microfluidic device)	33nm 17 nm	The meniscus radius of curvature observed experimentally is smaller than interstitial radius of the packed bed; imbibition happens before full condensation.
Alfi et al. (2016)	Lab on a Chip	50 nm	Bubble point temperature inside 50 nm channels found to be same as the bulk values.

Based on the Table 3.1 and Table 3.2, most of the simulations confirmed that in the pores below 100 nm the fluid phase behavior starts deviating from the behavior observed in the bulk phase. Majority of these studies proposed a radius of 10 nm as the critical radius of confinement below which phase transition and critical properties follow a completely different path from what is expected based on equations of state for bulk behavior. There are some contradictions between the predicted behavior of fluid inside these tiny pores using different simulation approaches and lack of experimental data makes it difficult to validate these models. The number of experimental and mathematical studies for a range of nanoscale pore sizes is summarized in Figure 3.30. Almost all mathematical approaches agree that the fluid inside pores larger than 100 nm has the same behavior as the bulk fluid, therefore, the focus of these simulation studies is on smaller pore radii.

Experimental data are needed for validation of these proposed theoretical models for pores smaller than 10-15 nm. However, to the best of our knowledge, no experimental study has been done so far in the pore radii below 15 nm due to the experimental limitations.

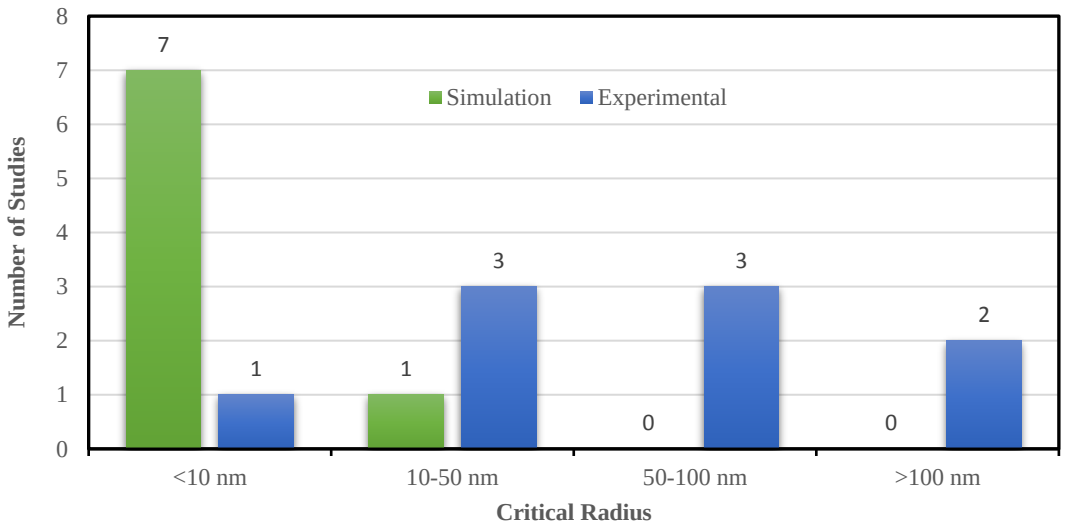

Figure 3.30. Comparison between number of simulation and experimental studies for the reported critical radii

Chapter 4: Experimental Procedure and Results

The provided literature review made it clear that to investigate the effects of nanoconfinement on phase behavior and fluid flow in porous media, we need experimental data to validate existing models. The main purpose of this chapter is to improve the understanding of fluid phase behavior under confinement by focusing on experimental measurements of saturation pressure of gas mixtures in nano-pores. Experimental methodology and detailed procedure are covered and reliable experimental data that helped with validating and enhancing existing models are provided. Further application of these results in reservoir simulation to to study the effect of confinement on phase behavior for pure components and binary mixtures of hydrocarbons experimentally, under both static and dynamic conditions is also covered.

4.1. Experimental Design Fundamentals

The first step in an experimental design is developing a plan with the following three branches (Figliola, 1995):

- Parameter design plan: the test objective, process variables and parameters, and a mean to control those need to be identified and determined.
- System and tolerance design plan: measurement techniques and equipment must be selected, and tolerance limits for associated errors must be determined using sensitivity analysis (uncertainty analysis).
- Data reduction design plan: a plan for analyzing, presenting, and using the anticipated data is needed.

Other considerations for designing a reliable experimental plan with the aim of producing accurate results are summarized below (Figliola, 1995):

4.1.1. Calibration

Calibration is the process of applying a known range of values to a measurement system and observing the output values to establish a relationship between the input known values, referred to as "standard", and the output values.

4.1.2. Uncertainty

There is always a slight difference between the exact value of a variable (true value) and the measured one. Errors associated with any measurement approach, which are the source of this difference between true and measured value, can be categorized into two general categories: random errors and systematic errors.

Random errors are random variations associated with the measured value during repeated measurements, while systematic errors cause an offset between the mean value of the data set and its true value. A system with systematic error shows a high repeatability and might give low random error but it has low accuracy because the measurements are considerably deviated from the true value. On way to minimize systematic errors is to conduct a calibration in order to minimize the offset between the measured values and the true ones. Random errors though, do not show any pattern and are not repeatable; therefore, they can only be minimized by increasing the number of measurements or reducing the measurement increments.

Quantifying the level of accuracy, precision, and reliability of data collected by a particular design or technique is an important part of experimental design. Uncertainty analysis is a numerical

estimation of the possible range of errors associated with measurements. Design-stage uncertainty tends to provide the first estimate of the uncertainty of a test by addressing the sources of possible error, while test stage uncertainty is associated with numerical analysis of the errors based on the identified sources and types of errors at the design stage.

As mentioned earlier, systematic errors are usually eliminated by calibration with a standard value, which can be either an accepted value or a theoretically calculated one. For random error sources, the measured values are randomly above or below the true values but do not skew in one particular direction. Arithmetic mean average, in these cases, gives the best value considering all the measured ones to minimize the associated random errors. In mathematical language, for measured values of x from 1 to N times, the arithmetic mean, $\bar{x}$, is:

$$\bar{x} = \frac{1}{N}\sum_{i=1}^{N} x_i \qquad (4-1)$$

If at any stage of measurements, one needs to find how much one individual measurement is scattered about the mean, standard deviation formula can be applied to quantify that.

$$\sigma = \sqrt{\frac{\sum_{i=1}^{N}(x_i - \bar{x})^2}{N-1}} \qquad (4-2)$$

If the uncertainty of a results depends on several variables, propagation of uncertainty or error propagation is used to analyze the error. First-order Taylor series expansion is one the widely used equations to quantify error propagation. If the measured result *f* is a function of physical variables *x*, y, z,… that have uncertainties of $\sigma_x, \sigma_y, \sigma_z$, …, then the uncertainty of *f* is calculated from the below equation:

$$\sigma_f^2 = \sigma_x^2(\frac{\partial f}{\partial x})^2 + \sigma_y^2(\frac{\partial f}{\partial y})^2 + \sigma_z^2(\frac{\partial f}{\partial z})^2 + \cdots \qquad (4-3)$$

To evaluate the total experimental error, all unrelated sources of errors and uncertainties need to be considered and combined. In this situation, uncertainty analysis of unrelated or independent errors need to be applied. The overall equation for this uncertainty is given by:

$$\delta = \sqrt{(\delta_1^2 + \delta_2^2 + \cdots + \delta_n^2)} \qquad (4-4)$$

Where, *x* with overall uncertainty of δ has *n* unrelated sources of uncertainty of $\delta_1, \delta_2, \ldots, \delta_n$.

4.1.3. Experimental Design and Optimization

To plan experiments that can examine a problem systematically and provide reliable data, performing random experiments that result in random obtained outputs must be avoided. Experimental optimization methods are the tools that help us to plan and perform experiments systematically in order to maximize obtained information from a minimum number of experiments (Lundstedt et al., 1998).

Some of the most popular experimental design approaches are summarized below:

- Classical design (one-factor at a time):
  Experiments can be design in a way that only one-factor at a time is investigated while all other independent factors are held constant. Repeatability is a measure of precision in classical design; which means that by repeating the trials under the same conditions and

analyzing the results, experimental error and the effect of other factors are minimized (Lazić, 2004).

- Factorial design:
  To consider the influence of all experimental variables, conditions, and their interactions with responses, factorial design is widely used. If a combination of *k* factors at two levels are investigated, the optimum number of needed experiments is 2^k based on the factorial design. If the number of influencing factors in an experiment is large (*k* is really big), then based on factorial method, the experiments need to be conducted are numerous. To proceed with manageable number of experiments and still be in the optimum range, fractional factorial design is used (Lundstedt et al., 1998).
- Fractional factorial design:
  As mentioned above, the factorial design involves the estimation of all the main effects, two-way interactions, three-way interactions, …, and k-way interactions. Nevertheless, fractional factorial design suggests that higher order interactions (3 or more in most of the cases) can be estimated by confounding them together. If *k* factors at two levels are investigated and *P* is the number of interactions that can be confounded together, then the optimum number of needed experiments is reduced to 2^{k-p} based on the fractional factorial design (Lundstedt et al., 1998).

Based on the provided explanation of the methods, classical experiment design is unable to account for uncontrolled changes, errors resulting from material variation, and errors resulting from the sequence of the tests. However, for special cases where individual effect of certain factors needs to be understood, a classical approach is the best choice. On the other hand, where the effects of several factors on the obtained result is studied or the results of test as a whole system in an organized, time-effective, and cost-effective way is needed, multi-factor designs work best (Lazić, 2004).

The methods mentioned above, are the tools used for designing experiments. Once the experiment is designed, in cases that no mathematical model is available for the research subject, strategies for optimization of the experiments are used (Lundstedt et al., 1998). One of the most popular strategies for optimization purposes in design of experiments is Response Surface Optimization (RSM). This methodology is a way to provide a graphical representation of the relation between experimental variables and responses and to determine an optimum. The requirement of using this methodology is having a polynomial function that contains quadratic terms and the process involves two phases: fitting a linear regression model to the data points up to the point that the linear regression model becomes ineffective; then, to proceed by fitting a non-linear quadratic regression equation to this new area of data points until the optimum region is found (Lazić, 2004). In experiments that are designed based on preliminary simulations, such as our designated experiment, the optimum region/point for conducting the experiment can be easily identified based on simulation results. Basically, a simulator helps us to simulate a number of different experiments by varying inputs and choosing our desired condition based on the outputs (Robert et al., 2012).

4.2. Experiment Design

4.2.1. Design Objectives

The objective of this research, as stated so far, was to experimentally investigate the effect of pore space size (confinement) on the saturation pressure of the fluid. To accomplish this ultimate objective, the following steps were taken in designing the system:

1. Building a new apparatus that complies with the following requirements:
    - Pressure and temperature resistance of the system need to comply with the required range based on the preliminary simulation results considering a safety factor of 1.5.
    - Pressure readings need to be precise, continuous, high-speed, and automated; temperature must remain constant at each stage of the isochoric process.
    - Easy access to any part of the apparatus is required for maintenance purposes.
2. Testing the apparatus with nitrogen prior to conducting hydrocarbon mixture experiments in order to:
    - Assure that the entire system is leak-proofed.
    - Determine all the volumes (bulk, packed, and dead volumes) accurately.
    - Assure that each part of the system is calibrated and works/measures properly.
3. Collecting the PVT data for both confined and bulk fluid system at the same time and under the same condition for the sake of accurate comparison.
4. Comparing the experimental outputs with the simulation results and validating the existing models accordingly.

4.2.2. Experimental Apparatus

As discussed in chapter 3, two possible experimental approaches for investigating the effects of phase behavior of confined fluid are visual and non-visual methods. Visualization is generally applicable for low pressure and temperature studies. Nevertheless, as mentioned earlier, the permeability of shale reservoir strongly depends on the pore pressure within the reservoir and pore throats which has been overestimated in low-pressure laboratory tests. In fact, as reservoir pressure decreases, viscous flow becomes negligible. At this point, slip flow and Knudsen diffusion (details provided in Appendix E) are becoming the dominant flow regimes. To effectively measure PVT characteristics at high pressure and temperature with visual methods, special designs and reinforcement are required to make the entire system, including transparent tubes, compatible with high pressure and resistant to high temperature which requires a huge investment on advanced micro-reactor design technologies, is complicated, time-consuming and very expensive.

Non-visual designs are mainly accompanied through application of nanoparticles and opaque tubes (metal tubes). They are commonly used for high pressure/high temperature studies. Conducting accurate and informative non-visual experiments, is in need of either finding or synthesizing porous media with a range of desired nano-pores to represent the behavior in tight formations and illuminate the degree and direction of PVT properties deviations. However, preparation of a well-packed porous medium with nano-scale porosities to operate under high pressure and temperature is needs a precise novel design.

In widespread PVT labs, manually operated chilled mirror dew point meters are mostly used to identify the dew point of hydrocarbons. These instruments have a metallic mirror surface inside a high-pressure cell which is equipped with a transparent glass port that is mainly used to observe the mirror surface and formation of liquid dropouts. The main problem of this method which relies on observing first signs of condensation is that most natural gas condensates are colorless with low surface tension which makes the liquid dropouts through condensations almost

invisible to the operator/camera. In the non-visual PVT cells, usually a known composition mixture is introduced into the cell and variations of one of the quantities are measured while the other one is kept constant. Measurements are normally made through isobaric or isothermal conditions. Although using isochoric measurements is less popular in petroleum and natural gas PVT studies, they make it possible to find saturation pressures needles of visual observations and phase separation processes. Working with a packed porous medium to investigate the effect of porous media on phase behavior is in need of having a well-packed porous medium with constant volume. Therefore, isochoric approach is selected for this work because of the convenience in conducting from experimental point of view and accuracy of results from the mathematical point of view. Also, because of constant composition condition, density measurements are more promising using isochoric approach and it better reflects real production through a control volume in which both pressure and temperature are subjected to change (Velez et al., 2010, Zhou et al., 2006).

Ideally, the isochoric cell volume must remain constant during the experiment. However, almost all materials are subjected to compression and expansion due to temperature change. Hence, the material which is used in making an isochoric cell needs to have low coefficient of thermal expansion; also, in order to handle the wide range of high pressure and temperature, the selected material must have a very high tensile strength. Although a high thermal conductivity is desired for the experimental cell to achieve uniform temperature across the cell and from this point of view metals like aluminum with conductivity of 3 J/s.cm.K seem more desirable, nevertheless, type 316 of stainless steel (with conductivity of 0.16 J/s.cm.K) is the best choice for our purpose because of more thermal and tensile resistance compared to other metals.

A PVT cell similar to a conventional PVT cell but with more capacity is built using stainless steel accumulators. Two SS accumulators are used for this purpose, one of them is the actual PVT cell which is packed with porous media (including extremely fine particles that can produce nano-scale pores) and the other one is basically bulk experiments cell. Commercial stainless still quarter turn-plug valves (316 SS) are used to isolate different parts of the system including packed cell from the sample cell. Both sample and main PVT cells are equipped with a piston inside them which can move upward by injecting a fluid (PG1 Oil or water) through Isco 500D syringe pumps from the small connections at the bottom of the cells. The major advantages of syringe pumps are the ability of continuous injection of the fluid with constant rate or constant pressure with high precision. A schematic of the design is shown in figure 4.1.

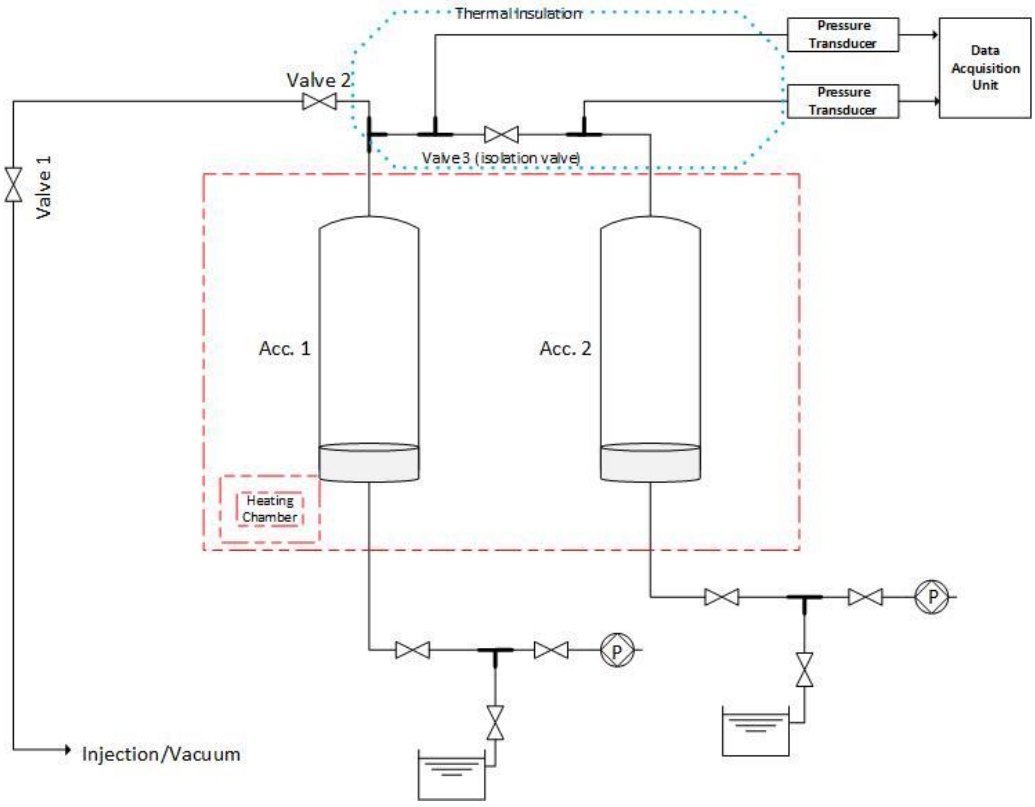

Figure 4.1. Schematic representation of the experimental set-up for isochoric experiment in bulk phase

4.2.3. Measurement Techniques

During the isochoric experiment the mass and volume of the system remain constant (we have a control volume that can only exchange energy with the environment). However, if at any point of the experiment, volume measurement was needed, it could be calculated based on the flow-rate readings on the Isco syringe pumps. Pressure data are collected using pressure transducers (that converts measured pressure into electrical signal) and a data acquisition system (DAQ) is used to record, monitor, and store data. For this purpose, the entire system is connected to a data acquisition and control system; NI 9205 on a NI Compact DAQ Chassis. LabVIEW program provides automated data acquisition and control; pressure transducers communicate with the computer through the DAQ and are converted into meaningful data through the LabVIEW program.

Two pressure transducers used in our case, are 1500 and 5000 psi pressure transducer (S-series Swagelok) with voltage range of 0 to 5 volts and have been calibrated using a dead-weight tester. The accuracy of transducers 0.25% of the range which brings us to the error range ± 0.0125 volts .To measure the pressure, pressure transducers are directly connected to the main PVT cells from the top connections, thus, they are in direct contact with the fluid sample and send real-time pressure values to the computer. Temperature is controlled by a heating chamber (VWR® Gravity Convection Ovens, 6.2 cu.ft., 120V) which provides a wide range of temperature control (with

accuracy of ±1 C) and heat transfer to the accumulators and is capable of holding the temperature constant at the predefined value throughout each stages of the test.

An HMI (Human Machine Interface) has also been designed to provide control and monitoring options for the entire system. All related programming is done using LabVIEW 2014 from National Instruments (Appendix F). The data are sampled every tenth of a second for pressure measurements during all stages of the experiment. Observing pressure and temperature, equilibrium condition is monitored and once it is achieved, the actual experimental procedure begins by changing the temperature stepwise resulting in a pressure change in both bulk fluid and the one inside the porous medium.

4.2.4. Identifying Error Sources

The Design-stage uncertainty aims to provide a preliminary estimate into the uncertainty of the test by preparing a checklist of common errors as below:

- Calibration errors: calibration of a variable against a standard value does not eliminate the system error entirely. Calibration errors are associated with three sources; the standard value itself, the calibration instrument or system, and the calibration process. As mentioned earlier, pressure transducers used for our experiments are calibrated using the dead weight tester (DWT); pressure producing and pressure measuring device. It is used to calibrate pressure gauges. The calibration process was performed with extra cautious and DWT was in good condition. Therefore, calibration errors can safely be assumed to be zero.
- Data-Acquisition (DAQ) errors: these are errors arising during acquiring data. These errors include system and instrument errors that are not already accounted for calibration; such as unknown changes to the measurement system conditions, sensor installation, sensor failure, etc. These errors are eliminated by calibrating pressure transducers first with DWT and then through the DAQ settings in Labview.
- Data-reduction errors: curve-fits and correlation of data may cause data-reduction errors in test results. Truncation errors, interpolation errors, and assumed models and functional relationships errors also fall into this category. Extra caution in data reduction strategies and interpolations must be taken to minimize these errors.
- Random errors: repeated measurements under fixed operating conditions is the strategy to be taken in order to observe possible random errors and minimize them.
- Systematic errors: as discussed before, systematic errors remain constant through repeated measurements under fixed experimental conditions. However, they are observable as a high or low offset in the measured values compared to the standard ones. In our experiment, running the entire test for the bulk phase (which can be accurately predicted by EOS) and comparing the results with standard values obtained from the simulations is a measure of identifying systematic errors, if they exist.

A thorough uncertainty analysis for the entire experiment as a whole system and for the experimental quantity (saturation pressure in our tests) is provided in later sections.

4.3. Fluid Selection

To examine the effect of confinement on the phase behavior of different mixtures of fluid; including pure and binary mixtures of hydrocarbons with different compositions, the experimental system explained in the previous section is used. At the beginning, a mixture with the most visible deviation in P-T behavior in the two-phase region compared to the single-phase one is used as a proof of concept to help with evaluating the entire procedure and conducting error analysis. The first phase of experiments is therefore to investigate the bulk phase saturation pressures in order to compare with the mathematical model for phase behavior simulation. Flash calculation for various two component hydrocarbon systems were carried out, followed by the generation and comparison of simulation results with experimental design requirements to choose the best composition considering the experimental limitation (pressure/temperature tolerance of the system).

WinProp module of CMG software, for characterizing the heavy ends of the petroleum fluids, lumping of components, matching laboratory PVT data through regression, simulation of first and multiple contact miscibility, phase diagrams construction and more, is used for the simulation stage of our work. WinProp has options to select from various equations of state for the oil and gas phases including Peng-Robinson (both the original (1976) and the modified (1978) one) and Soave-Redlich-Kwong (both the original (SRK) and the modified SRK(G&D) one). In this work, we compare the results from PR (1978) and SRK(G&D) with the experimental results in the next sections.

Values for vapor phase z-factor, vapor phase volume percent and vapor phase mole percent at each temperature and pressure were obtained from flash calculations for various two component hydrocarbon systems including Ethane – Butane, Ethane – Pentane, Ethane – Hexane, and Ethane – Heptane with varying compositions. A two-phase envelope was also generated by simulation for the mentioned mixtures. Based on the designated approach for isochoric experiment, calculations were carried out to get the pressure values at the experimental temperatures. The total volume of the system was kept constant at 25 cubic centimeters or 0.000883 cubic feet (calculations for isochoric test are independent of the volume and the actual volume of the system can easily be updated after running the first test with nitrogen and calculating the volume). Initial pressure and initial temperature were reference conditions identified on the phase diagram based on the fact that the system has to be in single gaseous phase at the beginning of each experiment. Real gas equation of state (compressibility equation of state) was used to get the total number of moles for the system according to the conditions and flash calculation data using the following equation,

$$PV = ZnRT \qquad (4-5)$$

Consequently,

$$n = \frac{PV}{zRT} \qquad (4-6)$$

This equation for only the gas phase, from flash calculation, can be re-written as:

$$\frac{Pv_g}{zn_g} = RT \qquad (4-7)$$

From the above equation, $\frac{Pv_g}{zn_g}$, is calculated for each temperature step and a plot of $\frac{Pv_g}{zn_g}$ versus pressure is generated (figure 4.2) based on which, the corresponding pressure is determined; here therefore, a matrix of pressure-temperature values is generated to plot the isochoric line associated with that specific composition on top of its phase envelop (figure 4.3). This process was repeated for all the mixtures mentioned above and for different composition of those; after running the phase behavior analysis for all, it was possible to choose the feasible zone on the phase diagram based on experimental limitations and from there, to choose the desired composition. The details of calculations and results are not provided here for all tested mixture composition and only for the selected composition is presented. The selected composition for the initial testing was identified to be %70 Ethane- %30 Pentane due to the following reasons:

- The choice of initial temperature and pressure is practical considering the experimental constraints (some of these mixtures and compositions require temperature/pressure condition out of the experimental system tolerance)
- The change in slope of the isochoric process clearly demonstrates the transition from single- phase (gas) to the two-phase region. This makes experimental detection of this transition possible considering experimental errors and limitations.

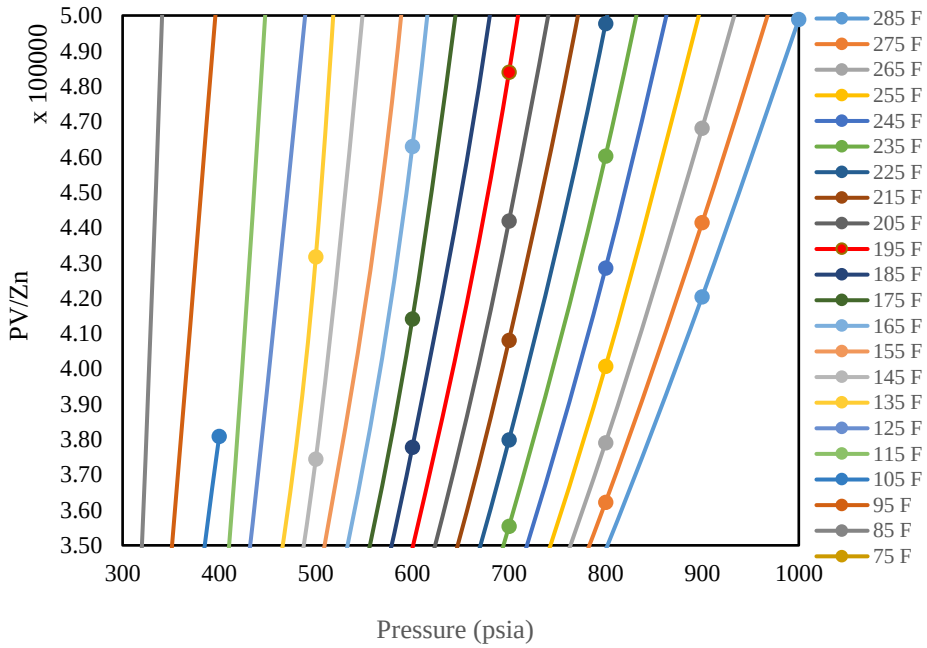

Figure 4.2. a plot of $\frac{Pv_g}{zn_g}$ versus pressure based on the data from flash calculation for the mixture of 70% C_2 and 30% C_5

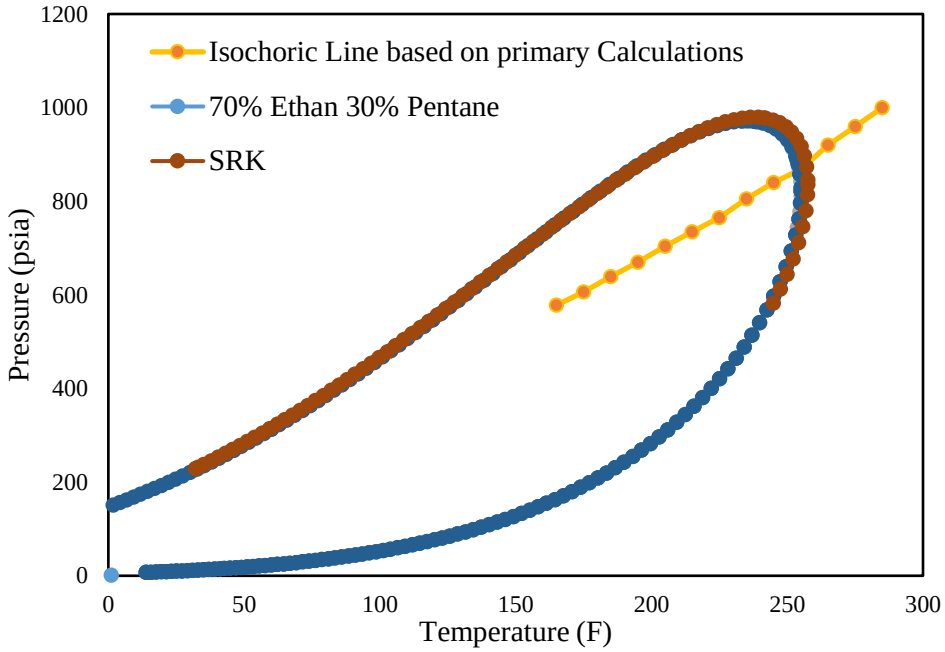

Figure 4.3. Phase envelop (generated by both PR- and SRK- EOS) and predicted isochoric direction for the mixture of 70% C_2 and 30% C_5

Based on these pre-calculations, the hydrocarbon sample of interest for the first experiment in the bulk phase is identified as a binary mixture of C_2 (%70) and C_5 (%30).

4.4. Isochoric Experiment Procedure for Bulk Fluid

In this section, the sample preparation and experimental procedure for the bulk fluid isochoric PVT test is explained systematically.

4.4.1. Volume/Leak Test

After mechanical preparation of the system and before conducting the actual PVT test, the entire system is tested with nitrogen for a period of 1 week (the approximate needed time to complete one full round of experiment) to make sure system is leak-proof through monitoring the pressure for any possible drop. Also, to make sure the system is working properly, and all the connection and parts are in working condition before loading hydrocarbon mixtures. At this stage, volume calculation is also performed through injection of water by a syringe pump and monitoring the pressure response of the system. The pressure fluctuations in the entire system over a period of one week (while it was pressurized with nitrogen under 400 psi) happened to be less than 1 psi on average which means the system was acceptably leak-proof. Volume calculations for the system is provided below:

Pressure is recorded as function of time and the system is closed meaning that number of moles remains constant. Water is injected at constant imposed flowrate using the syringe pump from the bottom of accumulator (isolated from the top by a piston and the top part is filled with nitrogen). Therefore, the following relation can be derived from the gas compressibility equation

considering the fact that nitrogen compressibility factor can be considered 1 at room temperature without affecting the results significantly.

$$P(t)V(t) = nRT \qquad (4-8)$$

$$P(t)(V_i - qt) = nRT \qquad (4-9)$$

$$\frac{1}{P(t)} = \frac{V_i}{nRT} - \frac{qt}{nRT} \qquad (4-10)$$

From equation (4-10), which is linear relationship between $\frac{1}{P(t)}$ and time, we can see that the plot of $\frac{1}{P(t)}$ versus time is a line with the slope of $\frac{q}{nRT}$ and intercept of $\frac{V_i}{nRT}$. V_i or the initial volume of the system before injecting water, gives us the volume of our interest (volume of each one of the accumulators or the volume of the entire system while connected if the isolation valve is open).

Based on the process explained above, volume of each accumulator without the tubing connecting it to the isolation valve between the two, is 1000 cc (details of calculation provided in Appendix G) which approves the manufacturing design criterion of 1 liter. The volume of the tubing in total is 9.5 cc. So, the entire volume of the system is 2009.5 cc.

4.4.2. Sample Preparation

Upon releasing the nitrogen, in preparation for injecting the actual testing mixture, the entire system is vacuumed for a period of two hours to make sure no air or contamination stays in any part of the system.

The amount of needed pentane in grams based on the total volume of the system is calculated considering the molar volume of pentane. The needed amount is then directly transferred to the test accumulator which was under vacuum. The needed volume of ethane is also calculated based on the total number of moles needed and the volume of the accumulator. One of the accumulators was used as a loading system (injecting piston) for ethane. After loading the entire sample, the composition is recalculated based on the injected amount. The loaded mixture composition is reported as %30.04 pentane and %69.96 ethane. The phase envelope and simulated isochoric lines are updated accordingly. Table 4.1 summarizes simulation results for isochoric process based on these updates.

Table 4.1. Isochoric process data-point based on simulation

Temperature (F)	Pressure (psia)
122	459
158	572
176	637
194	698
203	731
221	790
230	823
239	856
248	890
255.2	921
262.4	956
269.6	991
282.2	1050

Upon completion of the sample preparation and loading stage, we close the isolation valve between the two accumulators to prepare the system for the isochoric experiment in the bulk phase.

4.4.3. Isochoric Test for the C_2-C_5 Mixture in Bulk

As mentioned earlier, the isochoric experiment starts from single-phase and ends up in the two-phase region. As a result, we run the heating chamber at the maximum needed temperature (the pre-defined start points on the single-phase; in this case 139 ^{0}C) while the pressure is monitored to assure reaching the stability, this might take up to several hours.

After reaching the equilibrium condition (constant pressure and temperature for two hours), the starting temperature and its corresponding pressure are recorded as the first data point of our isochoric line. Then the oven temperature is reduced to the second highest temperature point defined based on the simulation and again pressure monitoring process for several hours begins until the system shows acceptable stability (less than 1 psi pressure fluctuation over few hours) which is considered as the equilibrium condition and the data is recorded accordingly. This process continues up to the lowest selected temperature point which is in the two-phase region (50 °C, in our case).

These collected data points are reported as a table (Table 4.2) and then plotted on the simulated phase envelop (figure 4.4) to identify the dew point and compare it with the simulation result.

Table 4.2. Isochoric process data-point based on experiment

Temperature (C)	Temperature (F)	Pressure (psia)
50	122	443.8
70	158	569
80	176	624.7
90	194	687
95	203	719.3
105	221	782.7
110	230	817.8
115	239	847
120	248	887
124	255.2	917
128	262.4	950.3
132	269.6	984
139	282.2	1050

Based on these results, the saturation pressure for a mixture of %69.96 C_2 and %30.04 C_5 at the temperature of 253.616 F and the pressure of 899.0344 psia; and the saturation pressure for this mixture at 253.616 F from the simulation results of isochoric process using PR-EOS is equal to 897.353 psia. If we consider the simulation value as our reference value and the experimental one as the measured one, the relative accuracy of the experimental measurement can be calculated as:

$$e = \frac{|Measured\ value - True\ value\ (Reference\ value)|}{True\ value\ (Reference\ value)} \times 100 \qquad (4-11)$$

$$e = \frac{|899.0344 - 897.353|}{897.353} \times 100 = 0.1874\%$$

As calculation shows, the difference between the experimentally measured value and the simulation driven one is less than 0.2% which is in the acceptable range for our experiments (<1%). This small difference might be due to some experimental uncertainties including component impurities (pentane used in this experiment is ≥99% purity from Sigma Aldrich and ethane is 99.99% purity from Airgas), weighting errors (the scale accuracy is 0.01 g) or loading process errors (since pentane is highly evaporable).

To minimize this error for the next stage of experiment where confined fluid saturation pressure is compared to the bulk one, the mixture introduced to both sides (bulk experiment test and packed experiment test) needs to be the same, loaded at the same time, and distributed at a single-phase of gas to ensure that aside from the confinement effect, no other factor can affect the measured saturation pressure.

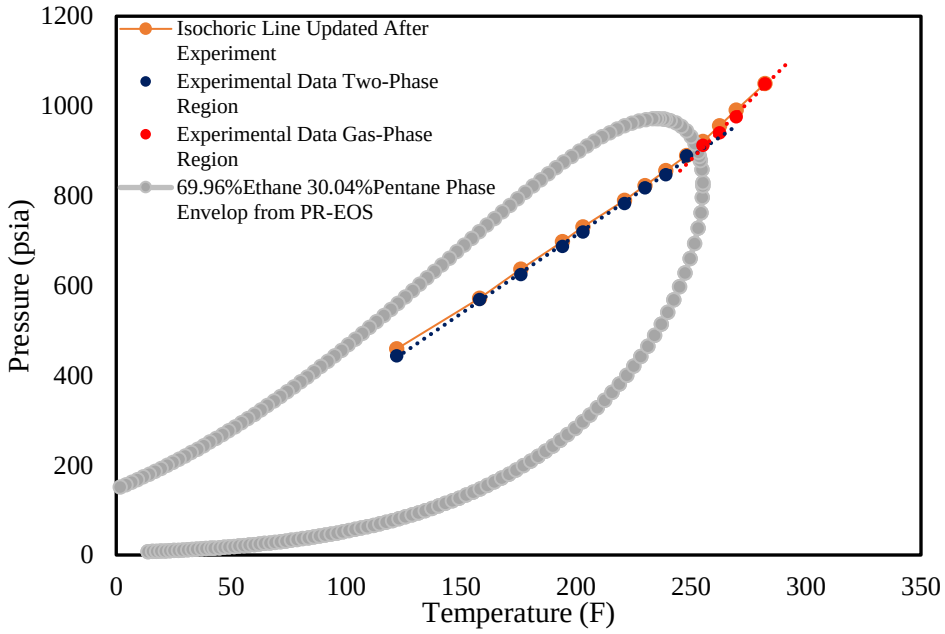

Figure 4.4. Phase envelop (generated by both PR-EOS) and predicted isochoric using compressibility EOS versus the isochoric experimental results for the mixture of %69.96 C_2 and %30.04 C_5

To assure that data are accurate, free of random errors, and the experiment is repeatable, after finishing the experiment and getting back to the ambient condition under equilibrium, the entire process is repeated. This time, the lowest temperature step (50 °C) is set as the start point and temperature is raised stepwise to the highest one (139 °C). In figure 4.5, the results of this round of experiment are plotted on top one the one presented in figure 4.4 to prove the repeatability of the experiment.

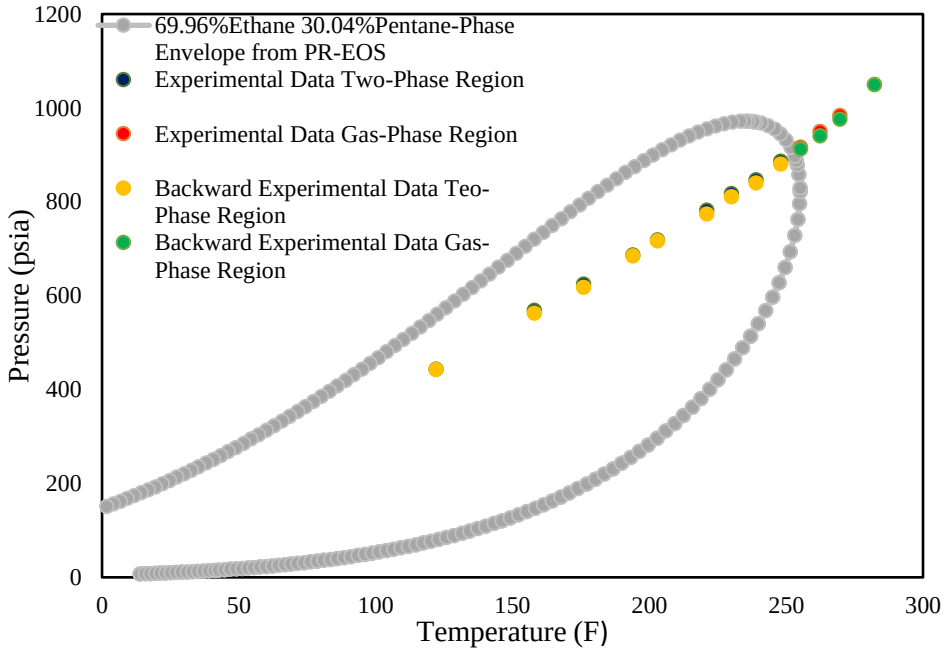

Figure 4.5. Repeatability of the isochoric experiment for the mixture of %69.96 C_2 and %30.04 C_5

As shown in figure 4.5, collected data on the second round of isochoric experiment (presented as "backward" because on contrary to the first experiment, the second one started from the lowest temperature step to the highest one) with the same sample in the bulk phase illustrate good agreement with the first round of isochoric experiment. The different between the values measured during the second round and the ones measured in the first-round ranges between 0.5 to 10 psia which brings it to less than 1.5% error.

This preliminary result and investigation provide us with the confidence in the method itself and the system built for the experimental purposes. Collected experimental data agreement with simulation results as well as reproducibility of the data through different runs of the experiment, is an indication of system's acceptable accuracy. Having said that, the next step is to design and build synthetic porous media to investigate the effect of that porous media on the measured saturation pressure from the isochoric experiment.

4.5. Isochoric Experiment Procedure for Confined Fluid

The scope of this stage of experiments is to provide comparative results of saturation pressure measurements for a fixed fluid mixture under both bulk-phase condition and packed phase condition. A schematic of the design for this experiment is shown in figure 4.6.

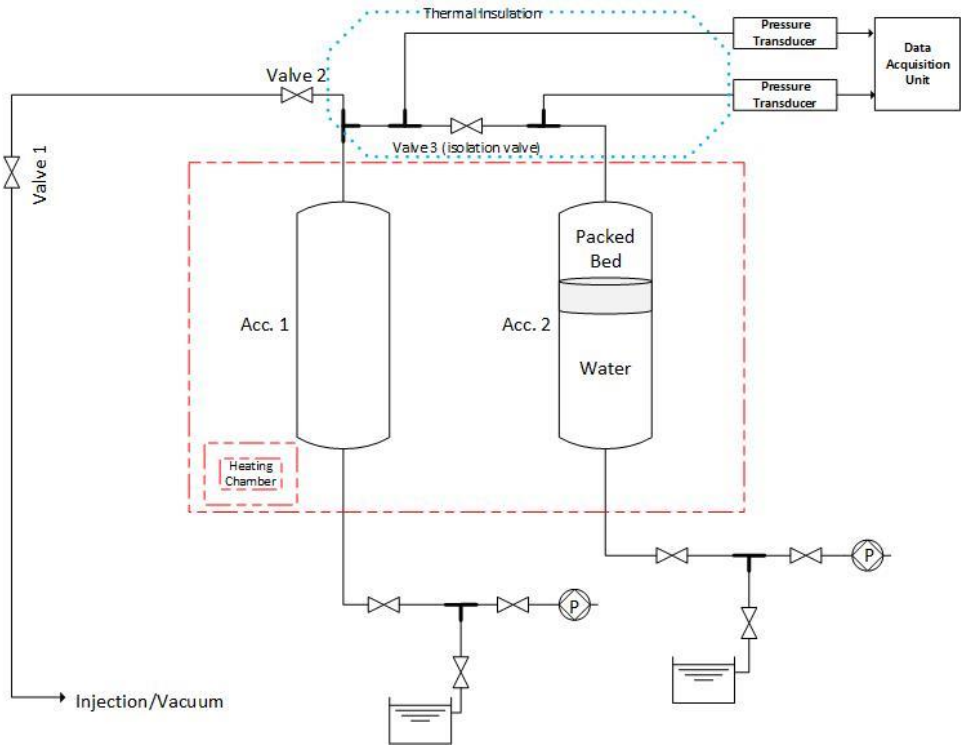

Figure 4.6. Schematic representation of the experimental set-up for isochoric experiment in both bulk and confined phase

Based on the schematic above, the fluid sample is prepared and loaded into accumulator 1 while the isolation valve between the accumulators (valve 3) is closed. Needless to say, leak test is completed first followed by vacuuming the entire system for a period of 2 hours to make sure no air or impurity remains inside any part of the system. The procedure for this stage of loading is the same as bulk test explained in section 4.4.2. Upon completion of the preparation and loading stage, the heating chamber is started (accumulators are still isolated, and the packed side is under vacuum) to raise the temperature to the required level while fluid is in single-phase now. Isolation valve will be opened afterwards to provide communication between the accumulators and pressure is monitored till equilibrium condition is stablished. From there, accumulators are isolated once again, and isochoric test is started by changing the temperature to the next desired temperature level. The required steps in completion of this procedure are explained comprehensively in the following sections:

4.5.1. Synthesizing Nano-Scale Porous Media

Nanoparticles needed for synthetizing porous media are chosen based on their size, temperature and pressure tolerance, wetting and adhesion properties, and chemical stability. After thorough investigation of available options, Barium Titanate ($BaTiO_3$) powder is selected for our experiments. Barium Titanate powder is usually used in designing nanoscale modules for the assembly of electronic devices, such as detectors, capacitors, and sensors. It has high resistance against pressure and temperature, is insoluble in water, alkalis and hydrocarbons but is soluble in

acids. The powders are provided by TPL, Inc in two controlled sizes of 400 nm (in diameter) and <100 nm; the key properties of the used $BaTiO_3$ powders are listed in table 4.3.

Table 4.3. Key properties of Barium Titanate Nano-powders from TPL, Inc.

Appearance	White powder
Melting point/ freezing point	1625ºC
Relative density	5.7 g/ml
Solubility	Insoluble in water/Alkanes
Incompatible materials	Strong oxidizing agents, Strong acids
Molecular Weight	233.19 g/mol

Barium Titanate is adhesive to metals and is not hydrocarbon/water wet and only its electrical properties are sensitive to water. This helps us to remove this effect from our experimental data to only focus on pore size factor and its related consequences.

The efficiency of our experiments relies on how good of a packing these particles can provide us. Two common methods for packing particles in the form of a well-packed solid disc or column are: dry packing, and wet or slurry packing. Particles that cannot be dry-packed as they get clumpy or they are too delicate to be mechanically pressurized to get well-packed, must be suspended in a liquid and introduced to their cell as a slurry. Once they are suspended in a liquid, they can be transferred and packed to the medium using a high-pressure pump. Then the stationary phase (solid particles) and the suspension liquid are homogenized, and liquid is removed with compatible methods and procedures to leave the packed solid particles behind.

The particles we are using ($BaTiO_3$ powders) are mechanically stable which makes them a great candidate for dry packing. There are different dry packing methods in the literature, a modified version of soil compaction method (applying downward force to compress the particles) using static force is developed for packing the needed porous media using $BaTiO_3$ particles in our experiment. Packing procedure is thoroughly explained below.

Figure 4.7. $BaTiO_3$ powders; particles with nominal diameter of 400 nm before packing

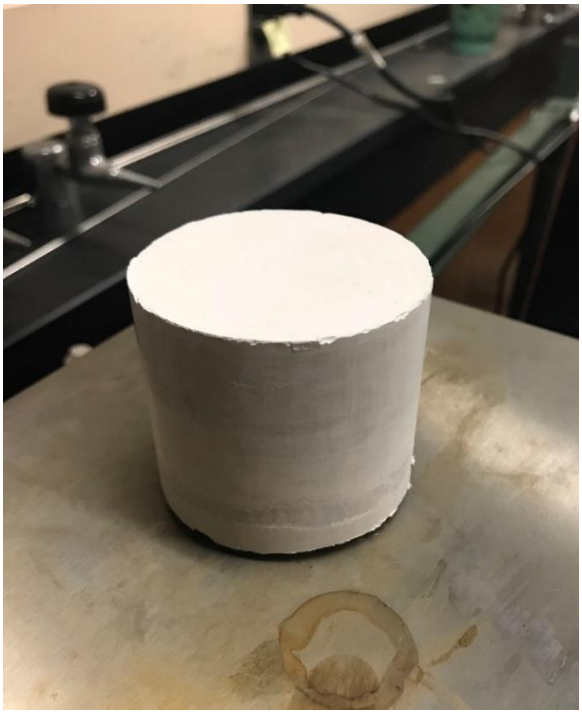

Figure 4.8a. Synthetized porous media; BaTiO3 powders (400 nm) after packing process

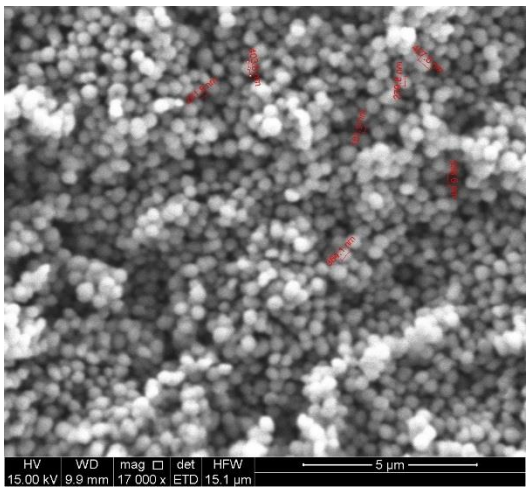

Figure 4.8b. SEM picture of the synthetized porous media; BaTiO3 powders (400 nm) after packing process, showing the pores and particles

The porous core presented in figure 4.8 is 2.35 inches in length and 2.45 inches in diameter which gives a bulk volume of 181.55 cc.

To get an estimation of the porosity, the core was saturated with water, weighted, then dried in oven for 48 hours and weighted again. As shown in figure 4.9, the difference in the weight between saturated and dried sample is 51.09 g.

Figure 4.9. Synthetized core weight saturated with water (left) and dry (right)

$$\varphi = \frac{V_{pore}}{V_{total}} = \frac{m_{water}/\rho_{water}}{V_{total}} = \frac{51.09}{181.55} = 0.28 \qquad (4-12)$$

Based on equation 4-12, the porosity of the BaTiO3 porous core sample is %28. If we consider particles as perfect spheres, this porosity value means the arrangement of the particles is one the tightest arrangements. Closest packings of the crystalline particles with average porosity of 26 to 28 percent, are hexagonal closed pack (hcp) or face-centered closed pack (fcc) (Conway, 1999). For either of this packing structures, the average hydraulic diameter of the pore throat can be estimated from equation 4-13 (Ally et al., 2016).

$$D_{h-pore\ throat} = \frac{2\sqrt{3}-\pi}{\pi} D \approx 0.103D \qquad (4-13)$$

Therefore, the average pore throat radius of our packed bed of BaTiO3 nanoparticles of 400 nm, is around 20.6 nm.

Upon synthetizing packed bed of BaTiO3 powders, the system is prepared for the leak test followed by isochoric experiment.

4.5.2. Volume/Leak test

Cell 1 is equipped with a piston isolating the top and the bottom portion of the cell. Therefore, the gas occupying the top portion could be pressurized by injecting fluid (water in this case) from the bottom. The bottom of cell 1 is connected to a syringe pump (Isco 500D) which injects water at a constant rate of 10 cc/min into the cell while the changes of gas pressure are recorded as a function of time. Helium is used for the purpose of volume measurement because its behavior is practically ideal at room temperature and the compressibility factor is almost 1. The real gas equation is rearranged as a function of time for this process assuming Z=1.

$$\frac{1}{P(t)} = \frac{V_i}{nRT} - \frac{qt}{nRT} \qquad (4-14)$$

The plot of $\frac{1}{P(t)}$ versus time is a straight line with the slope of $\frac{q}{nRT}$ and the intercept of $\frac{V_i}{nRT}$. Vi or the initial volume of each part of the system is then determined. By isolating different parts of the system and repeating the above procedure, volumes of different sections of the system are measured (Table 4.4).

Table 4.4. Volume characterization of the experimental apparatus

Volume of Cell 1 (V1)	1070 cc
Volume of Cell 2	173.75 cc
Dead Volume (V2)	11.111 cc
Pore Volume (V3)	74.64 cc
Total Volume	1155.751 cc

After measuring the volumes, pressure was monitored for almost 72 hours. After this period, pressure fluctuation remained under 1 psi which proved that the system is leak-proof.

Upon preparation of the porous media inside the experimental cell designed for holding the packed bed (cell 2), system (V1+V2+V3) is vacuumed for a period of 48 hours prior to loading the gas sample into the experimentation cells (cells 1 & 2). Once sample is loaded into cell 1 at room temperature and desired pressure, it expands into cell 2 by opening the connecting valve between the cells. After pressure stabilization, the isolating valve between the cells is closed and the corresponding pressure on both sides is recorded. Then, the temperature is increased stepwise to a maximum of 423.15 K and the corresponding stable pressure values are recorded at each temperature.

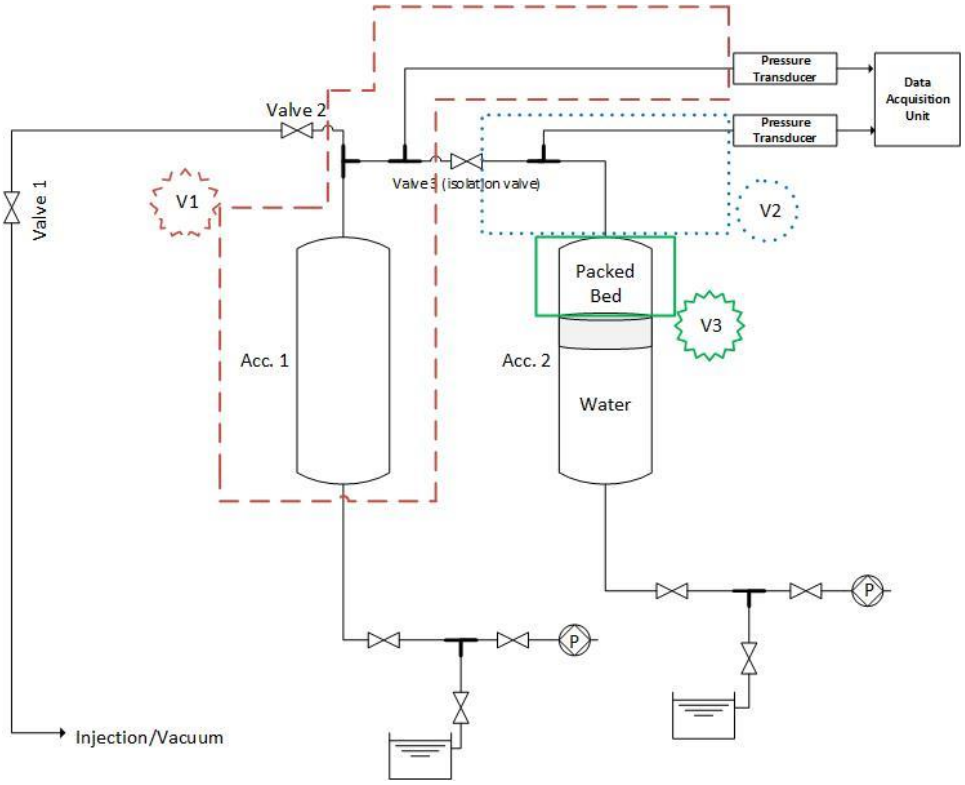

Figure 4.10. Schematic of the experimental setup for isochoric test representing different volumetric sections of the system.

4.6. Behavior of Pure Gases under Confinement

Compressibility factor (Z-factor) is simply a correction factor inserted into the ideal gas equation to make it match the behavior of real gases and is defined as the ratio of the volume occupied by a real gas in a container to the volume that it would occupy at the same pressure and temperature if it was an ideal gas. Z-factor is not a constant and is a function of the gas composition, temperature and pressure. Other equations of state were formulated to correct the ideal gas law for real gases in a way that non-ideality could be assumed constant (McCain, 1990).

Attempts to capture the non-ideality of real gases using mathematical calculations started by van der Waals (1873) who proposed the addition of two terms to account for the "attraction between molecules" and the "volumes occupied by the molecules" to the original ideal gas equation. These proposed molecular attraction and volume correction terms were modified by several scholars throughout the years to make correlation results more compatible with the experimental ones (Danesh et al., 1991).

Using compressibility factor EoS, makes it possible to find Z-factor knowing that it should be equal to unity for ideal cases. Although Z-factor could be directly obtained from the compressibility EoS, its accuracy is limited by the level of accuracy in determining exact values of V and n (Waxman and Hastings, 1971). These uncertainties along with the difficulties of experimental determination of Z-factor using Burnett apparatus (Waxman and Hastings, 1971)

encouraged researchers to derive Z-factor of pure components from commonly used equations of state whose accuracy was proven to be acceptable for pure gases, including van der Waals (VDW), Redlich-Kwong (RK), and Peng-Robinson (PR) equations of state (Danesh, 1998, McCain, 1990, McCain, 2010).

Recent complications faced by the industry in producing from unconventional formations and the failure of stablished mathematical correlations in explaining these complications, brought up the need of revisiting some fundamental correlations. From the literature review on the confinement effect it is evident that, aside from the theory of deviation in saturation pressures of the confined fluid mixtures compared to the bulk, critical properties, density and compressibility factors of pure gases are also affected by the confinement

Travalloni et al. (2010a) studied the critical behavior of pure confined fluid using an extension of van der Waals equation of states. They concluded that reduced pore size affects the critical properties of the pure confined fluid (nitrogen in their study), hence reduced properties of the gas in also affected. This effect is noticeable when the pore radius is less than 50 times of the fluid molecule diameter (nitrogen molecule size is 0.155 nm; so, this effect is distinguishable at pore radius of 7.75 nm or less). The modified equation proposed by Travalloni et al. (2010a) and its parameters are listed below:

$$P = \frac{RT}{v - b_p} - \frac{a_p}{v^2} - \theta \frac{b_p}{v^2}\left(1 - \frac{b_p}{v}\right)^{\theta - 1}\left(1 - F_{pr}\right)\left(RT\left(1 - \exp\left(-\frac{N_{av}\varepsilon_p}{RT}\right)\right) - N_{av}\varepsilon_p\right) \quad (4-15)$$

Where,

$$F_{pr} = \frac{(r_p - \frac{\sigma}{2})^2 - (r_p - \frac{\sigma}{2} - \delta_p)^2}{(r_p - \frac{\sigma}{2})^2}$$

$$a_p = a\left(1 - \frac{2}{5}\frac{\sigma}{r_p}\right)$$

$$b_p = \frac{N_{av}}{\rho_{max}}$$

$$\theta = \frac{r_p}{\delta_p + \frac{\sigma}{2}}$$

$$\sigma = \sqrt[3]{1.15798\frac{b}{N_{av}}}$$

$$\rho_{max}\sigma^3 = c_1 - c_2 \exp\left(c_3\left(0.5 - \frac{r_p}{\sigma}\right)\right) + c_4 \exp\left(c_5\left(0.5 - \frac{r_p}{\sigma}\right)\right)$$

r_p is the pore radius, σ is the fluid molecule diameter, δ_p is the distance between the center of the fluid molecule and pore wall (in fore field potentials it is usually shown by *r* and typically

gets the value of 0.2 nm for gases), N_{av} is the Avogadro number, ε_p is the energy parameter of the molecule-wall interactions (can be calculated based on force field potentials, Travalloni et al. (2010a) used square-wall potential which gives the value of $\varepsilon_p = 1.31 \times 10^{-21}\, J$), a_p and b_p are adjusted van der Waals parameters (same as a and b in original van der Waals), and ρ_{max} in the density of close packed molecules in a fluid based on van der Waals interactions which constants are provided below:

C_1	1.15798
C_2	0.479264
C_3	0.620861
C_4	0.595114
C_5	4.01377

The effect of confinement on compressibility factor of methane was also studied by Devegowda et al. (2012) for the pore size of 2, 4, and 5 nm. They also stated that a correction of z-factor under confinement is needed because the critical properties are shifted. Sanaei et al. (2014) proposed some correlation to determine the shift in critical properties of pure fluid and based on those corrections, determined z-factor of methane (as a pure gas) under confinement for different pore sizes ranging from 1 to 50 nm. As shown in the figure 4.11, the values of compressibility factor tend to reach to the bulk values for pore radii of 50 nm or above.

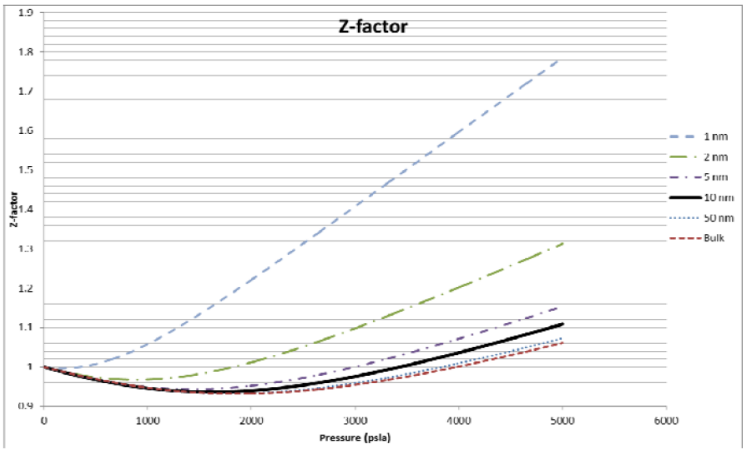

Figure 4.11. Effect of confinement on the z-factor of methane at 180 F (Sanaei et al., 2014).

The effect of pore size on the compressibility factor of methane was also explored by Nagy and Siemek (2014) using PR-EOS with modified critical properties and their results also approve the change in compressibility factor as a function of pore size for pore sizes less than 100 nm; these values tend to reach the z-factor value of bulk phase for pore sizes above 100 nm.

Van der Waals, Redlich-Kwong, and Peng-Robinson equations of state are known as comparatively precise correlations for predicting vapor pressure of non-polar or slightly polar fluids in both industrial and scientific calculations (Ahmadi and Bahadori, 2017, Mesbah and Bahadori, 2017). These equations of state in terms of gas compressibility, by considering the first

and second derivatives of the original equations equal to zero at the critical point, are written in the following forms (Danesh, 1998, McCain, 1990):

Van der Waals EoS:

$$Z^3 - (1 + B)Z^2 + AZ - (AB) = 0 \qquad (4-16)$$

Where, $A = 0.421875\frac{P_r}{{T_r}^2}$ and $B = 0.125\frac{P_r}{T_r}$.

Redlich-Knowng EoS:

$$Z^3 - Z^2 + (A - B - B^2)Z - (AB) = 0 \qquad (4-17)$$

Where, $A = 0.42747\frac{P_r}{{T_r}^{2.5}}$ and $B = 0.08664\frac{P_r}{T_r}$.

Peng-Robinson EoS:

$$Z^3 - (1 - B)Z^2 + (A - 3B^2 - 2B)Z - (AB - B^2 - B^3) = 0 \qquad (4-18)$$

Where,$A = 0.45724\,\alpha\frac{P_r}{{T_r}^2}$, $\alpha^{0.5} = \left(1 + m(1 - T_r^{0.5})\right)$, $m = 0.37464 + 1.5422\omega - 0.26992\omega^2$, $B = 0.07780\frac{P_r}{T_r}$ and ω is the Pitzer acentric factor. α is assumed to be 1 where the temperature dependency of attractive forces is ignored.

Different modifications of equations of state proposed by scholars in an attempt to explain the deviation of confined gas behavior compared to the bulk may be found in literature. The three selected models to compare with our experimental data are listed below:

Modified form of the van der Waals equation of state by Ma et al. (2013), suggests the following corrections to the critical properties of the confined fluid:

$$\Delta T_c = \frac{T_{cB} - T_{cP}}{T_{cB}} = 1.1775\left(\frac{D_p}{\sigma}\right)^{-1.338} \qquad (4-19)$$

$$for\ \left(\frac{D_p}{\sigma}\right) \geq\ 1.5 \quad (\Delta T_c = 0.6\ for\ \left(\frac{D_p}{\sigma}\right) <\ 1.5)$$

$$\Delta P_c = \frac{P_{cB} - P_{cP}}{P_{cB}} = 1.5686\,(\frac{D_p}{\sigma})^{-0.783} \qquad (4-20)$$

Where, T_{cB} and P_{cB} are the critical properties of the bulk fluid and T_{cP} and P_{cP} are the critical properties of the confined fluid. D_p, is the pore diameter, and σ is the fluid molecule diameter.

Pitakbunkate et al. (2015) evaluated the effect of pore size reduction on critical properties of pure gases using Lennard-Jones potential parameters that could characterize van der Waals interactions between the molecules. They used molecular simulation (Grand Canonical Monte

Carlo) and their calculations did not involve the use of any equations of state. However, their results show that for pore sizes less than 10 nm, the critical properties of the confined fluid are suppressed compared to the bulk and this suppression increases as the pore size decreases. The shifts in the critical properties of confined methane and ethane for pore sizes between 1 to 10 nm are reported in their study.

Sun et al. (2018) proposed another correction to the critical properties of confined fluids based on the fitting an equation to their molecular dynamic simulation results. Their proposed correction is very similar to the one used by (Ma et al., 2013, Sanaei et al., 2014)); however, another term to account for the adsorption layer effect on the critical properties is added in their corrections. If the thickness of the adsorbed layer of gas is considered zero, their proposed correlation for calculating the shift in critical properties of the fluid can be written as below:

$$\Delta T_c = \frac{T_{cB} - T_{cP}}{T_{cB}} = 1.2\left(\frac{D_p}{\sigma}\right)^{-1.13637} \qquad (4-21)$$

$$\Delta P_c = \frac{P_{cB} - P_{cP}}{P_{cB}} = 1.5\left(\frac{D_p}{\sigma}\right)^{-0.625} \qquad (4-22)$$

Where, σ is the Lennard-Jones potential parameter for the confined gas.

A comparison between the shift in critical properties using the above-mentioned models is provided in Figure 4-121a for methane in the pore sizes of 1 to 10 nm and in Figure 4-11b for ethane confined in the pore sizes of 1 to 20 nm.

TcB and PcB are the critical properties of the bulk fluid and TcP and PcP are the critical properties of the confined fluid.

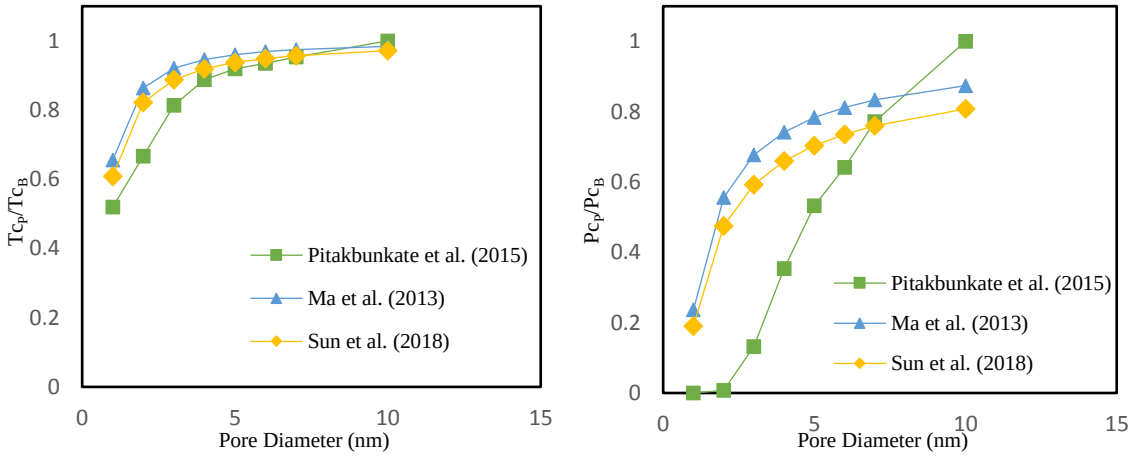

Figure 4.12a. The shift in the critical properties of methane; left: critical temperature ($\frac{T_{cB}}{T_{cP}}$), right: critical pressure ($\frac{P_{cB}}{P_{cP}}$).

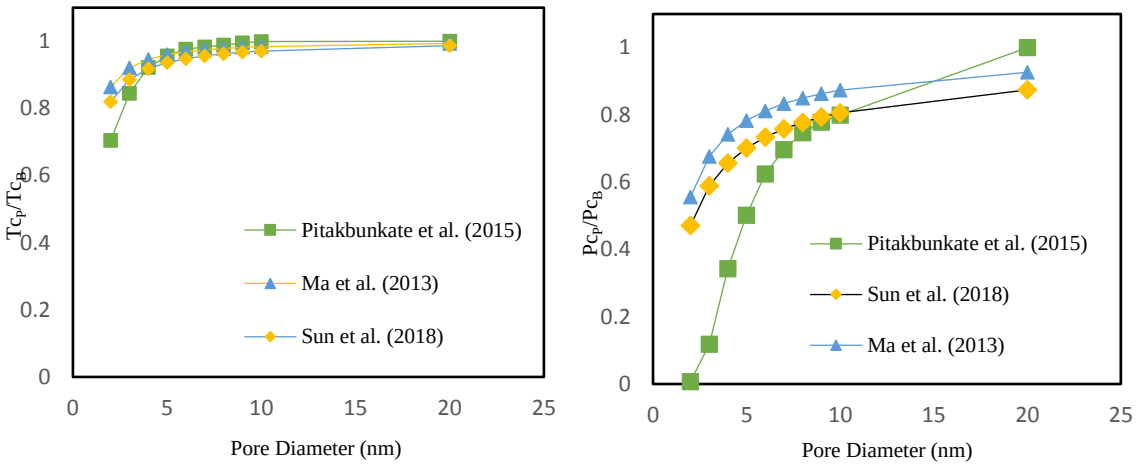

Figure 4.12b. The shift in the critical properties of ethane; left: critical temperature ($\frac{T_{cB}}{T_{cP}}$), right: critical pressure ($\frac{P_{cB}}{P_{cP}}$).

As illustrated in the Figures 4.12a & b, there is a smoother change in the critical properties of ethane and methane as a function of pore sizes using the proposed corrections by Ma et al. (2013) and Sun et al. (2018). These two correlations are used in the later sections for comparing the experimental data collected for the confined gas in comparison to the bulk.

This brief literature review shows that even pure gases show a different behavior under confinement compared to the bulk behavior and the degree of this effect is a function of pore size. However, limited experimental data are available to validate most of these models. Therefore, it is informative to explore the effect of pore sizes on behavior and properties of pure gases like nitrogen before diving into saturation pressure studies for hydrocarbon mixtures using isochoric approach. The experimental procedure for this test is explained below.

The compressibility factors of target gases for this study, helium, nitrogen, methane, and ethane, at the predetermined temperature and pressure steps are calculated using all of the three mentioned equations of state. From there, the graphs of Z-factor versus pressure and RT= ($\frac{Pv_n}{Z}$) versus pressure are generated. Pressure values corresponding to each temperature step are derived from the real gas equation (RT vs P graph generated based on $PV = ZnRT$) and the isochoric (P-T) lines based on each EoS is plotted afterwards (Salahshoor and Fahes, 2018). These results are compared with the experimentally measured pressure values at each temperature to examine the accuracy of these equations in predicting pure gas behavior at the bulk condition. This methodology is based on real gas equation (compressibility EoS) and values of Z-factors are derived using several mathematical approaches to highlight the sensitivity of the behavior of real gases to the values of Z-factor.

4.6.1. Fluid Selection

Two hydrocarbon and two non-hydrocarbon gases are selected for this study. Based on the literature, methane and ethane are two of the frequently studied gases that are abundant in tight

formations. Nitrogen is also studied as one of the non-hydrocarbon gases with significant variation in its properties in the presence of porous media. Helium, on the other hand, is known to be a semi-ideal gas which has a gas compressibility factor of nearly 1 over a decent range of pressures and temperatures. Helium was used at three different initial pressures (150 psi, 300 psi, and 500 psi) to conduct the isochoric experiment as a proof of concept. Helium has small molecules and a very low critical pressure and temperature (listed in Table 3) and very small change in its critical properties is predicted by different models.

Increasing the temperature stepwise by 20 K from room temperature (293.15 K) up to 423.15 K, no changes are observed in pressure readings between the confined helium compared to the bulk.

Properties of these gases, including critical properties, molecule sizes, and Lennard-Jones potentials, are listed in Table 4.5 (Ben-Amotz and Herschbach, 1990, McCain, 1990, Pitakbunkate et al., 2015, Talu and Myers, 2001).

Table 4.5. Molecular and critical properties of studied gases

Gas	LJ Parameter (nm)	Effective Molecule Diameter nm)	Critical Pressure (psi)	Critical Temperature (K)
Helium	0.264	0.271	33.20	5.2
Nitrogen	0.361	3.451	492.31	126.2
Methane	0.373	3.835	668.62	190.6
Ethane	0.429	4.240	706.65	305.3

4.6.2. Experimental Results for Pure Fluids

The temperature steps to conduct all the tests using all gases are defined (in Kelvin) to be: 293.15, 323.15, 343.15, 363.15, 383.15, 403.15, 423.15. For the preliminary tests, helium is loaded into the system at three different initial pressures: 150 psi, 300 psi, and 500 psi. To collect P-T data each of these three preliminary tests, both confined and bulk helium undergo the same isochoric process starting from the same initial pressure while cells 1 & 2 are isolated. Collected data are reported on P-T graphs in Figures 4-13a to 4-13c. From these graphs, it is evident that the corresponding pressures of helium at each temperature step remain the same for both bulk and confined condition.

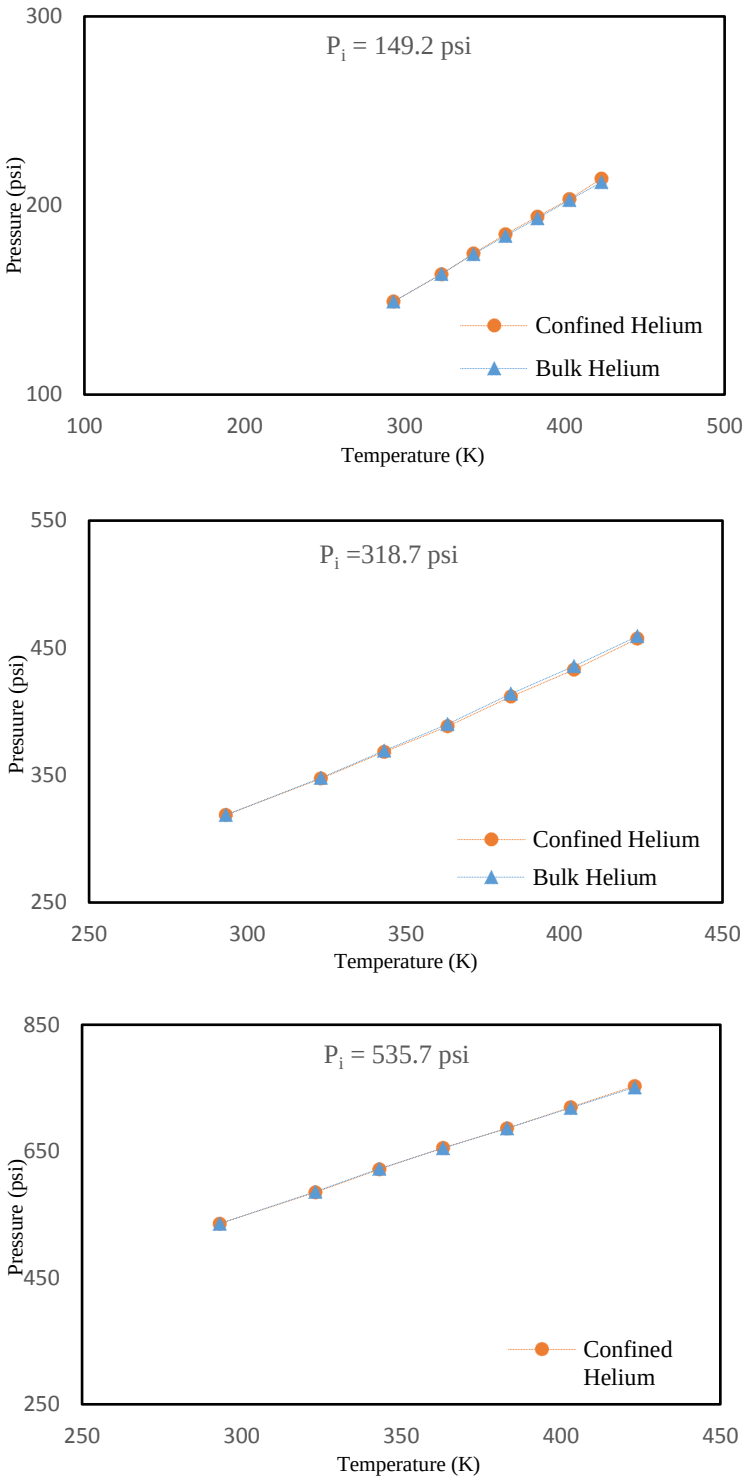

Figure 4.13a-c. Pressure-Temperature data collected for helium under both bulk and confined phases undergoing simultaneous temperature increase.

The experimental data presented in Figures 4.13a-c, are compared with the calculated data using vdW-, RK-, and PR- EoS. Figure 4.14 presents P-T behavior of bulk and confined helium

from the experiment along with equations of state calculated data points. Based on this graph, PR-EoS gives the most congruent data with the experimental results while RK-EoS deviates notably from the measured experimental data at higher pressures. Both correction for the confinement effect (Ma et al., 2013, Sun et al., 2018), predict small shift in the critical properties of helium as a result of confinement and their predicted pressure values show good agreement with the experimentally measured ones. Overall, helium behavior and properties are not noticeably altered as a result of confinement and almost all of the equations of state can predict its P-T behavior with acceptable accuracy.

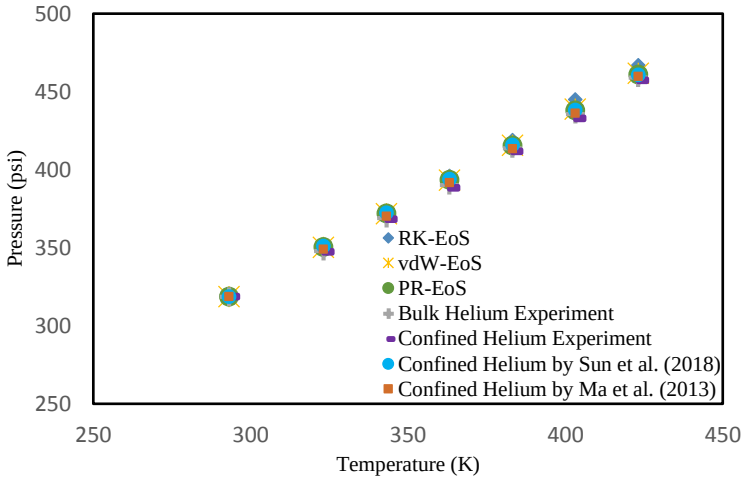

Figure 4.14. Experimental and EoS calculated P-T data for helium (Pi=318.7)

For the next set of tests, nitrogen is used at initial pressures of 150 psi, 300 psi, and 500 psi. Unlike helium, nitrogen shows higher pressure readings for the confined system at each temperature step compared to the bulk. This pressure difference between the bulk and confined nitrogen increases with the rising temperature and is more pronounced for the test with 500 psi initial pressure (22.5 psi @ 423.15K). This difference is 13.7 psi and 13.5 psi at 423.15 K for the tests with 300 psi and 150 psi initial pressure respectively. Figures 4.15a-4.15c illustrate the experimentally measured pressures at each temperature step for both confined and bulk nitrogen.

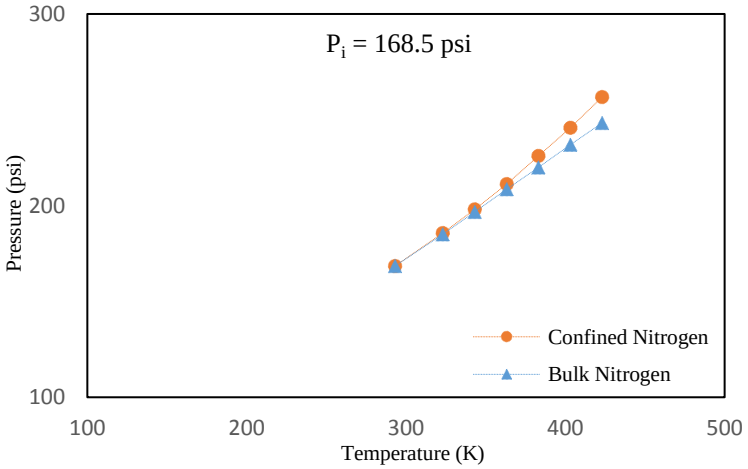

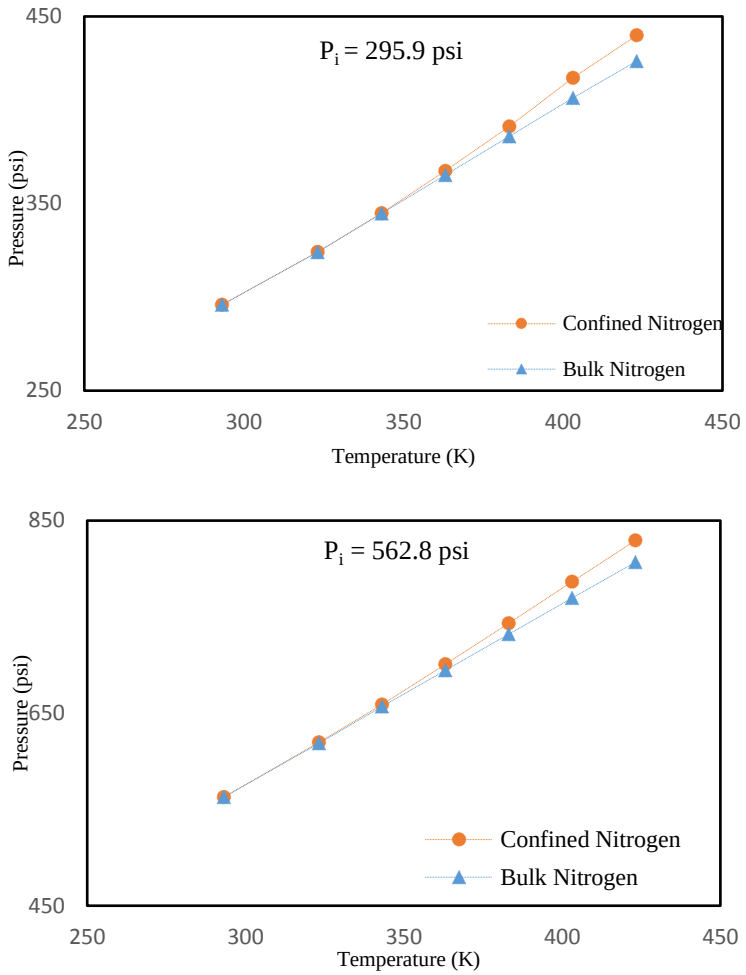

Figure 4.15a-c. Pressure-Temperature data collected for nitrogen under both bulk and confined phases undergoing simultaneous temperature increase.

Based on figure 4.15b and the plots for helium, we conclude that initial pressure of around 300 psi, would be a good choice to identify the shift in the behavior of confined gas compared to the bulk, if there is any. This conclusion is also verified using one hydrocarbon gas (methane) whose P-T graphs are provided in Figure 4.16a-b. Therefore, for the rest of analysis using methane, ethane, and nitrogen, the datasets with initial pressure of 200 to 300 psi are selected.

The graph of P-T isochoric line for the ethane experiment with the initial pressure of 240.5 psi is provided in Figure 4.17. As demonstrated in this figure, the shift in P-T behavior of confined ethane is also increasing with temperature increase (19 psi @ 423.15 K).

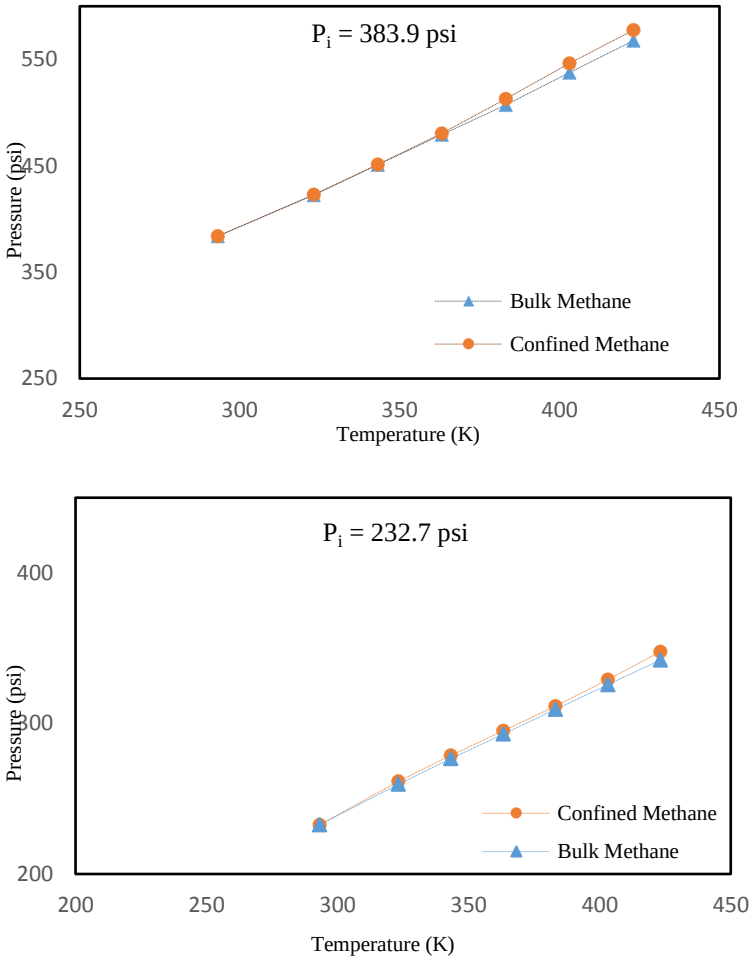

Figure 4.16a-b. Pressure-Temperature data collected for methane under both bulk and confined phases undergoing simultaneous temperature increase.

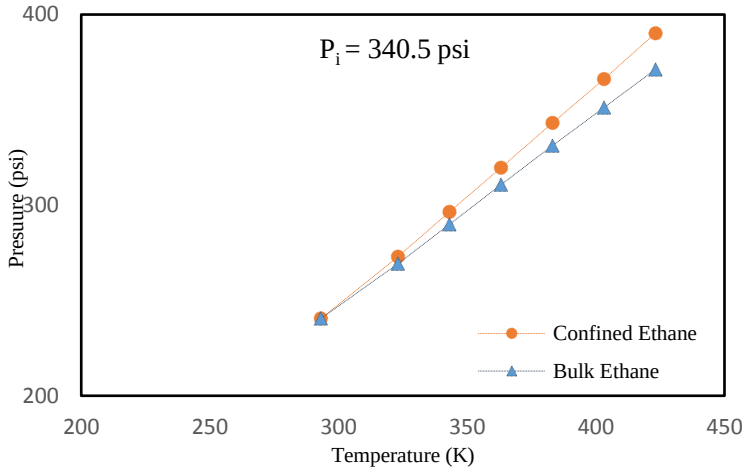

Figure 4.17. Pressure-Temperature data collected for ethane under both bulk and confined phases undergoing simultaneous temperature increase.

4.6.3. Modeling Behavior of the Bulk Gases using Various EoSs

For the selected range of pressures and temperatures based on the experimental design, the P-T behavior of each of the studied gases is extracted based on vdW-, RK-, and PR-EoS for that specific pressure and temperature range. Figures 4.18a-d show this analysis for the bulk behavior helium, nitrogen, methane and ethane respectively.

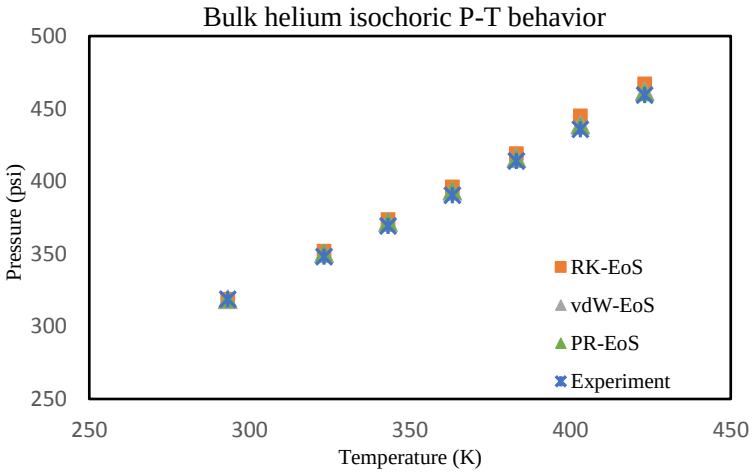

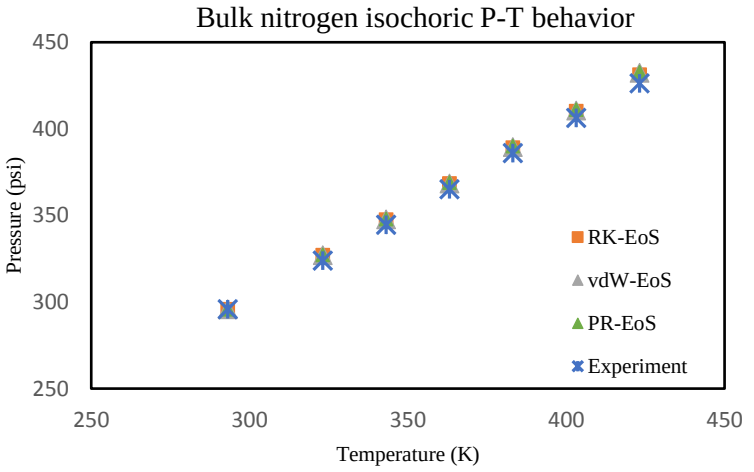

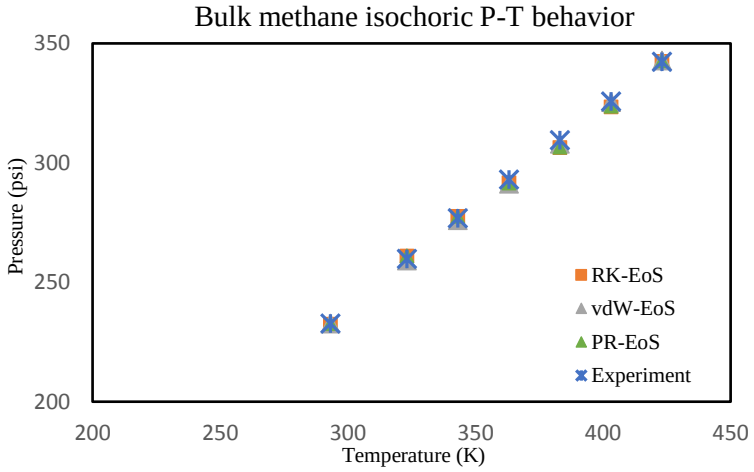

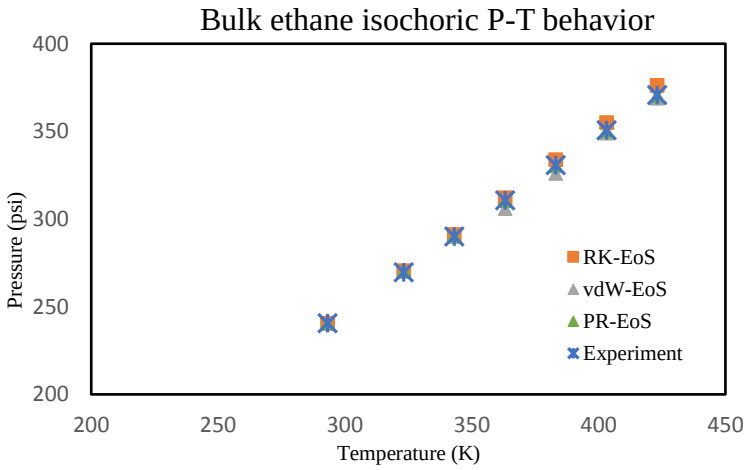

Figure 4.18a-d. Comparison between experimental and EoS derived isochoric P-T line for the bulk (a) helium, (b) nitrogen, (c) methane, and (d) ethane

As illustrated in figure 4.18a-d, all equations of state can predict the pressure of pure gases as a function of temperature with an acceptable accuracy (less than 5 psi difference with the experimentally measured pressures). However, Peng-Robinson EoS is the one providing the most accurate pressure values compared to the experimental data; RK-EoS tends to overestimate the pressure at higher temperatures while vdW-EoS tends to underestimate it. Therefore, PR-EoS is selected for analyzing the behavior of these gases under confinement using the suggested corrections in the literature.

4.6.4 Modeling Behavior of the Confined Gases using Various Modified EoSs

Shifted critical properties of the studied gases using equations 4-19 to 4-22 are listed in Table 4.6. Average pore throat diameter for all calculations is assumed 20 nm based on the particles and packing properties. Effective molecule diameters and Lennard-Jones constants used for the calculations are also same as Table 4.5.

Table 4.6. Original and shifted critical properties of pure gases

Gas	Original Critical Properties		Shifted Critical Properties (Ma et al., 2013)		Shifted Critical Properties (Sun et al., 2018)	
	Critical Pressure (psi)	Critical Temperature (K)	Critical Pressure (psi)	Critical Temperature (K)	Critical Pressure (psi)	Critical Temperature (K)
Helium	33.20	5.20	32.18	5.19	31.04	5.18
Nitrogen	492.31	126.20	472.58	125.90	453.37	125.50

Methane	668.62	190.60	641.06	190.15	614.63	189.47
Ethane	706.65	305.32	675.14	305.21	644.38	303.20

The isochoric lines for the confined helium, nitrogen, methane, and ethane are illustrated in Figure 4.19a-d. The results of calculated pressure values using vdW-EoS with shifted critical properties through Ma et al. (2013) proposed corrections are indicated by "Modified EoS-1" and the ones calculated using PR-EoS with shifted critical properties by Sun et al. (2018) proposed corrections are identified as "Modified EoS-2".

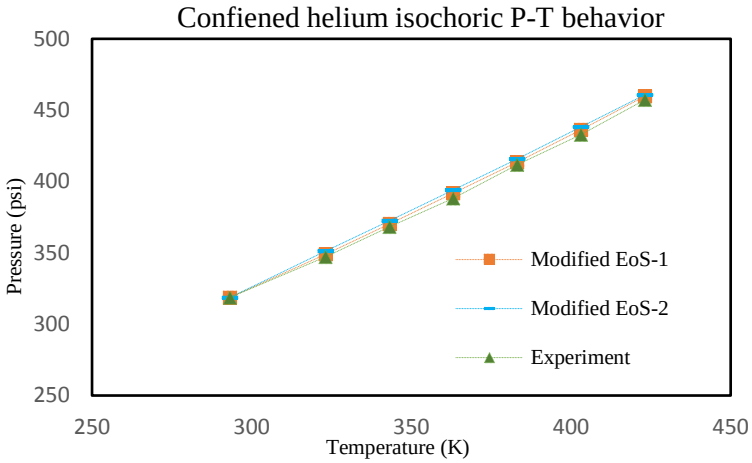

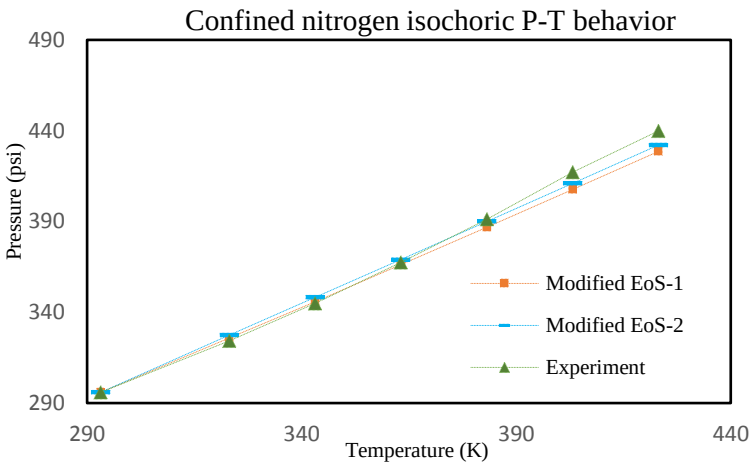

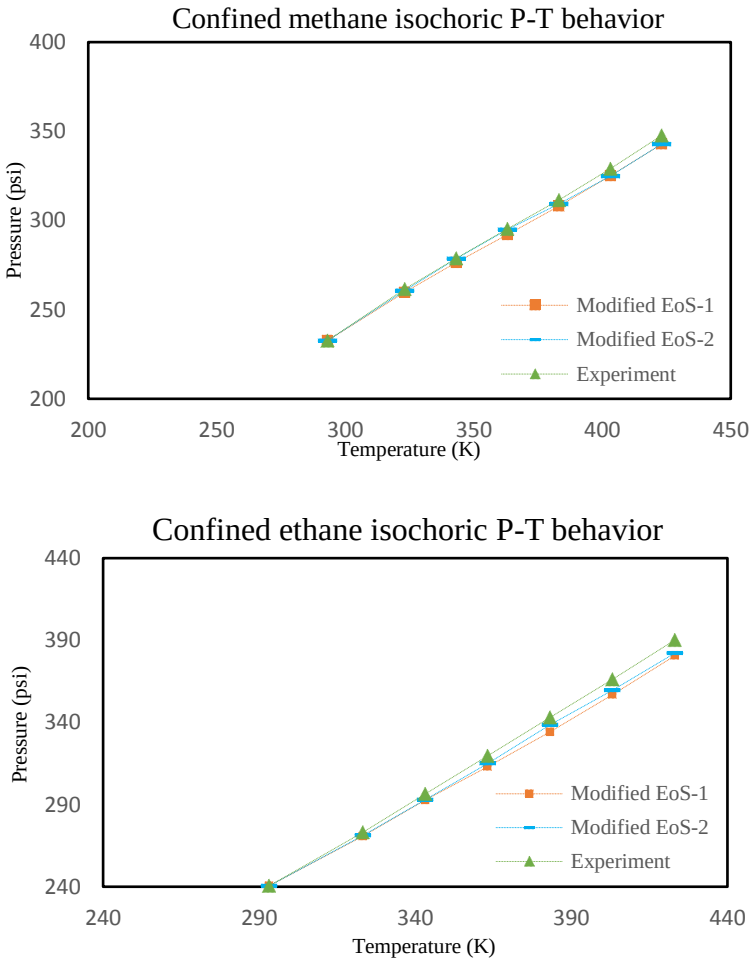

Figure 4.19. Comparison between experimental and EoS derived isochoric P-T line for the confined (a) helium, (b) nitrogen, (c) methane, and (d) ethane

Based on the figure 4.19a-d, we conclude that the proposed correlations by Sun et al. (2018) for estimating the shift in critical properties of the confined fluid provides a better match with the experimentally measured pressures (Table 4.7). Therefore, the intermolecular potential parameter (σ), also known as Lennard-Jones potential parameter, gives a more accurate value for the shift in critical properties (maximum error of %1.3) compare to the effective molecule diameter (maximum error of %2.6). Also, it is evident that adjusting the constant in the critical properties shift equation would improve the compliance of the correlation data with the experimental results. This could be achieved by modifying the temperature dependent term in the original PR-EoS (α) or by driving a new Z-factor correlation to calculate Z and insert it in the real gas equation.

The experimental data comparing behavior of pure gases in a decent range of pressures and temperatures for both bulk and confined condition prove that there is change in the properties and behavior of fluid caused by the porous media and pore size effect. Most of the published models in the literature agreed on the effect of confinement on fluid behavior. However, there are discrepancies in measuring the extent of this effect for various gases and different pore sizes using these correlations or models. This experimental procedure uses pressure measurements for pure

gases (both hydrocarbon and non-hydrocarbon) undergoing the same heating process to evaluate present models and correlations in terms of their accuracy in capturing the level of the change in the behavior of confined fluid. Results show that although using correlation involving shifted critical properties of the fluid as a function pore and fluid molecule sizes are correct in terms of providing the direction of the shift, they do not show enough accuracy at higher temperatures. This effect needs to be further investigated to develop a new all-inclusive model or correlation that could be applied to a wide range of pore radii and molecular potentials for different pressure and temperatures.

Table 4.7. Experimentally measured pressures and calculated pressures from modified equations of state using shifted critical properties

Confined gas	Helium		
Temperature(K)	Experimental Pressures (psi)	Pressures (psi) derived from Ma et al. (2013)	Pressures (psi) derived from Sun et al. (2018)
293.15	318.7	318.7	318.7
323.15	347.3	349.1	350.2
343.15	368.3	370.3	371.6
363.15	388.3	391.8	392.8
383.15	411.7	413.6	413.7
403.15	432.9	436.3	436.0
423.15	457.3	459.8	458.1
Confined gas	Nitrogen		
Temperature(K)	Experimental Pressure (psi)	Pressures (psi) derived from Ma et al. (2013)	Pressures (psi) derived from Sun et al. (2018)
293.15	295.9	295.9	295.9
323.15	324.2	325.94	327.6
343.15	344.9	345.86	348.4
363.15	367.4	366.2	369.3
383.15	391.2	386.88	390.2

403.15	417.2	407.7	411.3
423.15	439.9	428.6	432.6
Confined gas	Methane		
Temperature(K)	Experimental Pressure (psi)	Pressures (psi) derived from Ma et al. (2013)	Pressures (psi) derived from Sun et al. (2018)
293.15	232.7	232.7	232.7
323.15	261.5	259.8	260.6
343.15	278.7	276.4	278.6
363.15	295.2	292	295.0
383.15	311.4	308.0.0	309.3
403.15	329.1	325.0	324.9
423.15	347.7	342.8	342.9
Confined gas	Ethane		
Temperature(K)	Experimental Pressure (psi)	Pressures (psi) derived from Ma et al. (2013)	Pressures (psi) derived from Sun et al. (2018)
293.15	240.5	240.5	240.5
323.15	273.0	270.8	271.2
343.15	296.5	292.8	293.0
363.15	319.6	313.0	315.0
383.15	343.1	334.2	338.6
403.15	366.2	356.8	359.6
423.15	390.2	380.6	382.2

4.7. Behavior of Gas Mixtures under Confinement

Phase behavior alterations as a result of confinement require very careful consideration and management so as to avoid possible irreversible losses in productivity. Some models show that confinement can result in a lower risk of condensation in retrograde fluids (Neshat et al., 2018; Rajput and Ertekin, 2014) while other models anticipate an increase in that risk with a higher dew point pressure value (Dong et al., 2016; Jin and Firoozabadi, 2016; Ma et al., 2013; Nagy and Siemek, 2014; Travalloni et al., 2010; Zarragoicoechea and Kuz, 2004).

Experimental work in this area to validate these models has been very limited. Most of the experimental work in this area are based on visual detection of the phase transition inside transparent nanochannels or the detection of the latent heat in calorimetry device (Alfi et al., 2016; Ally et al., 2016; Mostowfi et al., 2012; Pinho et al., 2014). Almost all these studies agreed that confinement in pores less than 100 nm has a significant impact on phase behavior regardless of the pore mineralogy. This effect is more pronounced in smaller pores down to below 10 nm where elevated intermolecular forced increase the levels of complexity of the models (Didar and Akkutlu, 2013; Kamalvand et al., 2008; Li et al., 2014; Peng and Yu, 2008; Pitakbunkate et al., 2015; Sanaei et al., 2014).

Equations of state have been used for decades to describe PVT behavior of reservoir fluids and are still actively used by the industry and in different simulators to investigate reservoir fluid properties. However, most of equations of state proven to be inaccurate in calculating reservoir fluid critical properties in tight formations due to the abundance of nanoscale pores and their consequences including perplexing phase behavior. Many scholars attempted to modify conventional equations of state to include the pore size effect on fluid properties in the original equations. A comprehensive review on these studies is provided elsewhere (Salahshoor et al., 2018). Nevertheless, most of these modifications cause continuous reduction of critical properties of the fluid with reducing the pore size. Therefore, constructed phase envelopes for the confined fluid using these modified equations with shifted critical properties result in an upward shift in the dew point pressure line of the phase envelope. This way, higher saturation pressure at each temperature is expected for the confined condensate mixture compared to the bulk while our experimental results show the opposite behavior. Lowry and Piri (2018) discuss that the mineralogy of the pores has to be considered along with the pore size to evaluate the degree and direction of the shift in the critical properties of nanoconfined fluid compared to the bulk. Liu et al. (2016) defines competitive adsorption of different components of the gas mixture as a controlling factor in alteration of fluid phase behavior. Basically, competitive adsorption of different components to the pore walls can change the initial composition of the fluid mixture and the shift in the critical properties happens consequently.

As stated by Jin and Firoozabadi (2016), direct use of equations of state, even with adjusting critical properties to account for confinement, is not accurate for nanopores, especially pores less than 10 nm. Salahshoor and Fahes (2018a), presented the deficiency of the correlations proposed for critical properties shift in capturing the extent of the change in P-T behavior of pure fluids under confinement. The correlation for critical properties shift proposed by Sun et al. (2018) based on their molecular simulation proves the best estimate of pure fluid isochoric behavior under

confinement. The same correlation is used here to adjust critical properties of ethane and pentane for the average pore sizes of 20 nm in diameter. Details of this correlation are provided in equations 4-21 and 4-22.

Another widely use modification of equations of state is based on adjusting VLE calculations to include the effect of capillary pressure in nanopores into the original calculations (Haider and Aziz, 2017; Liu et al., 2016; Nojabaei et al., 2012; Rajput and Ertekin, 2014). This theory is based on adapting Young-Laplace equation (Eq. 3) into the capillary pressure models, where θ is the contact angle between the pore wall and the wetting phase.

$$dP_G = dP_L + \frac{2\sigma \cos\theta}{r} \qquad (4-23)$$

The first step in VLE studies is defining equilibrium ratio ($K_i = \frac{y_i}{x_i}$). In a multi-component system, the equilibrium ratio is defined as the ratio of the mole fraction of a component in gas phase (y_i) to the mole fraction of that component in liquid phase (x_i) (Lake, 1989).

Zuo et al. (2018), developed a model to incorporate the effect of capillary pressure into phase envelope and saturation pressure prediction of fluid mixture using equation of state. This study show that the presence of capillary pressure causes a decrease in the bubble point pressure of the confined fluid compared to the bulk and an increase in the dew point pressure with reducing the pore size. Their proposed modification to the SRK EoS is used in this study to evaluate the experimental results.

This study utilizes isochoric experiment to examine pressure-temperature (PT) relationships along isochoric lines for a binary hydrocarbon mixture under both confinement and bulk conditions. This experiment is used as a proof of concept for the application of this technique in identifying fluid properties changes of hydrocarbon mixture in the presence of porous medium. Experimental results are compared with the results of some of the widely used correlations for critical properties alteration of fluid in nanopores proposed in the literature. Test results demonstrate that when a fluid mixture is confined in less than 100 nm pore spaces, the dew point pressure of the fluid is shifted towards a lower pressure at a constant temperature compared to the bulk in the retrograde region. Several scholars confirmed this behavior through modeling works (Jin and Firoozabadi, 2016; Neshat et al., 2018; Neshat and Pope, 2017; Rajput and Ertekin, 2014).

4.7.1. Fluid Selection

Barium Titanate (BaTiO3) nanoparticles (≥99.5% purity) in two controlled sizes of 400 nm (in diameter) and <100 nm is used to synthesize a nanoscale porous media. Barium Titanate is insoluble in both water and alkanes and is highly hydrophilic which makes it a great candidate to decouple the effect of mineralogy and wettability from the pore size effect on the hydrocarbon phase behavior. Ultra-high purity ethane (≥99.99%) and HPLC grade pentane (≥99%) are used in this work as hydrocarbon components.

4.7.2. Experimental Procedure

The experiment starts by vacuuming the entire system, including both accumulators, porous medium and all connection, for a period of ten hours to eliminate any possible impurity. After vacuuming, isolation valve (valve 3) is closed which isolates the porous medium from the bulk experimental cell. A binary mixture of %70 ethane and %30 pentane is loaded into a Acc. 1 using a third accumulator as the loading chamber to inject required amount of each component to get the specified composition at the required initial pressure based on the simulation results (Salahshoor and Fahes, 2018).

Once fluid is loaded to the bulk test accumulator (Figure 4.6), the temperature of the air bath is increased to 302 Fahrenheit in order to get the fluid mixture into the single-phase gas region. Once thermal and mechanical equilibrium is established (identify by pressure stabilization recorded through data acquisition unit), the isolation valve is opened to let the fluid expand into the porous medium. Temperature remains constant and pressure is monitored continuously to achieve stabilization. Once system is stabilized, the isolation valve is closed to separate the bulk space from the confined one. From there, isochoric test is started by reducing the temperature of the air bath stepwise and recording the corresponding stabilized pressure on both sides (bulk and confined) through two identical pressure transducers. Upon getting to the minimum temperature (194 F), the temperature is increased with the same increment to get back to the starting point (302 F) while stabilized corresponding pressure is recorded at each step. This process is repeated three times (providing 6 pressure measurement at each temperature) to confirm the reproducibility od the data and minimize possible associated human/measurement errors. Reported pressure value is the arithmetic mean of the 6 recorded values with a maximum standard deviation of 2.8.

Data are plotted on top of the phase envelope for the experimented mixture with the specified composition to illustrate the alteration of saturation pressure (dew point in this specific test) inside nanoscale pore sizes of a tight formation compared to the bulk.

The locus of phase boundary for a binary mixture of %70 ethane and %30 pentane is constructed using SRK equation of state. Volume shift parameters of 0.0605 and 0.1209 are adjusted in the simulator for ethane and pentane respectively to eliminate the volumetric deficiency of equation of state (Ahmed, 2010).

4.7.3. Data processing & experimental uncertainty

During the isochoric experiment the mass and volume of the system remains constant (the system is a control volume that can only exchange energy with the environment). Prior to the experiment, volumes of each section of the setup are measured using gas compressibility equation for the pure gas (helium) filling the system. This gas is pressurized through fluid injection using syringe pump to the bottom of Acc. 1 which is equipped with a piston isolating the bottom portion from the top. Pressure is recorded by 5000 psi pressure transducers with voltage range of 0 to 5 volts (providing ± 0.2 psi accuracy) connected to a data acquisition system (DAQ) which records, monitors, and stores the data Human machine interface (HMI) provides automated data acquisition and control system. Data are sampled every tenth of a second for pressure measurements during all stages of the experiment. Temperature is controlled by a heating chamber capable of holding the temperature constant at the predefined value throughout each stages of the test with an accuracy of ±1 Fahrenheit.

Calibration of a variable against a standard value does not eliminate the system error entirely. Calibration errors are usually associated with three sources; the standard value itself, the calibration instrument or system, or the calibration process. In this work, pressure transducers are calibrated using the dead weight tester (DWT), a pressure producing and pressure measuring device used to calibrate pressure gauges. Calibration process was performed with extra cautious and DWT was in good condition. Therefore, we safely assume calibration errors to be zero. Data-Acquisition (DAQ) errors are errors arising during acquiring data. These errors include system and instrument errors that are not already accounted in calibration; such as unknown changes to the measurement system conditions, sensor installation, sensor failure, etc. These errors are eliminated by calibrating pressure transducers first with DWT and then through DAQ settings in Labview program. Curve-fittings and correlation of data may cause data-reduction errors in test results. Truncation errors, interpolation errors, and assumed models and functional relationships errors also fall into this category. To minimize this category of errors, pressures are recorded every tenth of a second for a period of at least 8 hours. Each reported pressure data is therefore the arithmetic average of 288000 continuous readings.

4.7.4. Experimental Results for Binary Mixture of $C_2 - C_5$

Experimental results of the isochoric test for a binary mixture of %70 ethane and %30 pentane are provided in Table 4.8.

Table 4.8. Isochoric experimental data for %70C_2-%30C_5

	Confined Space	Bulk Space
Temperature (F)	Pressure (psi)	Pressure (psi)
302	1115	1115
284	1043	1025
266	970	941
257	940	900
248	910	868
230	855	810
212	800	750
194	743	690

These results are plotted on the generated phase envelope for the same mixture to show the saturation pressure (point of the slope change) for both bulk and confined fluid on top of the phase boundary and illustrate the direction of the shift (Figure 4.20).

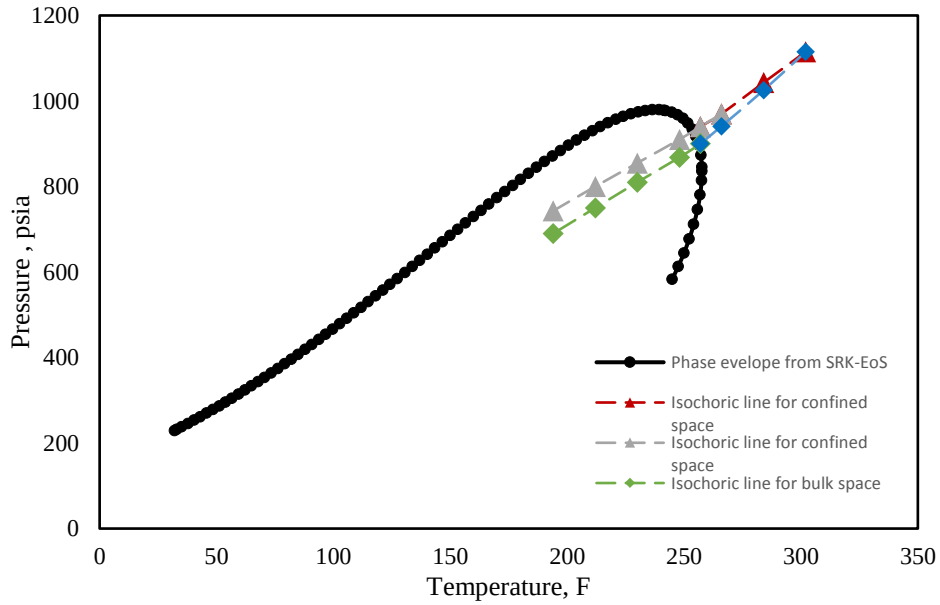

Figure 4.20. Comparison between the isochoric P-T line for the confined mixture of %70C_2-%30C_5 and the bulk mixture of the same composition

As shown in the Figure 4.20, detected saturation pressure for the bulk fluid is 900 psi at the temperature of 257 F which clearly matches the boundary of the phase envelope at that specific temperature. However, the change of the slope happens at the pressure of 941 psi and temperature of 266 F for the confined fluid. This is presented in Figure 4.21 in more details.

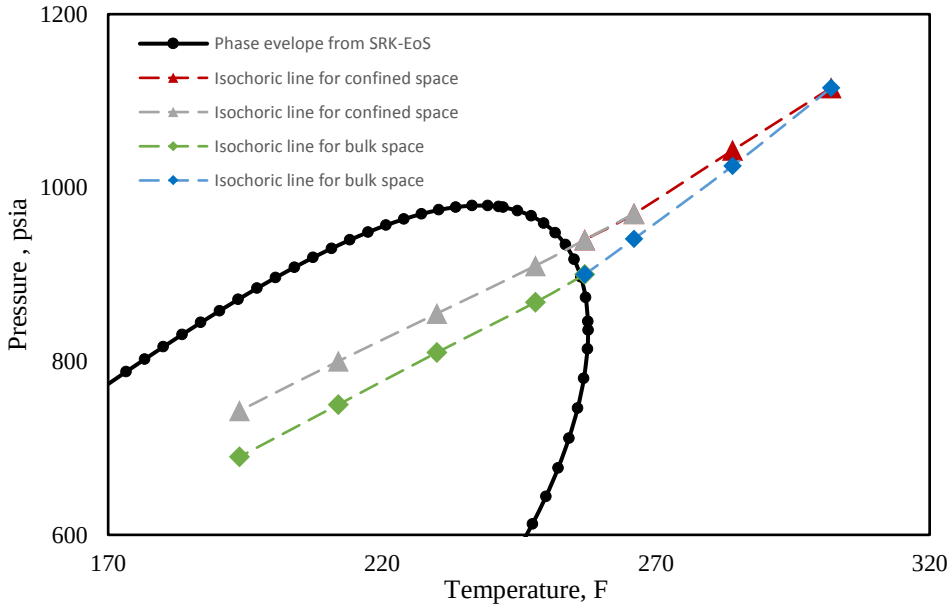

Figure 4.21. Identifying the change of slope in the isochoric line for bulk and confined fluid mixture (%70C_2-%30C_5) to determine the phase transition point

4.7.5. Modeling Behavior of the Confined Mixture using Modified EoSs

Observation of the break in the slope of isochoric line for the fluid in the confined space at a higher temperature and pressure compared to the bulk is an evidence of condensation occurrence with a smaller pressure & temperature drop than what is normally expected for the bulk fluid mixture. In other words, condensation is nanopores can happen while the pressure and temperature are still above the dew point of the bulk fluid calculated using equations of state.

Phase envelope of the confined binary mixture of C2-C5 is generated using shifted critical properties calculated by equations 4-19 to 4-22. In the Figure 4.22, by adjusting critical properties of the components for pore diameters of 1000, 500, 400, 100, 40, and 20 nm, phase envelopes are generated for C2-C5 mixture. As shown in this figure, the phase envelope gets smaller and smaller by reducing the pore diameter and moves towards the bulk for pore sizes around 1 µm.

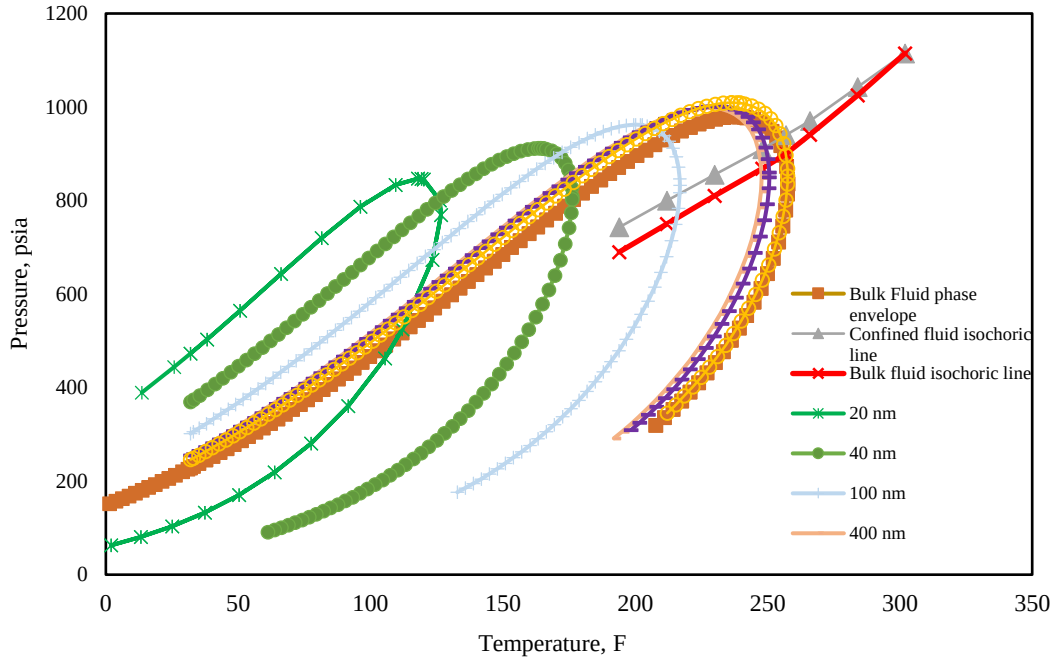

Figure 4.22. Continuous shrinkage of the envelope for a mixture of %70C_2-%30C_5 in bulk and confined spaces as a result pore size reduction

Other proposed correlations for critical properties shift available in the literature are similar in term of predicting the direction of the change and are slightly different in estimating the extent of the shift (Devegowda et al., 2012, Ma et al., 2013, Pitakbunkate et al., 2015, Travalloni et al., 2010b, Zarragoicoechea and Kuz, 2004). Experimentally determined dew point pressure, however, approve that the direct application of the equation

s of state, even by modifying correlations, are not accurate.

4.7.5. Modeling Behavior of the Confined Mixture using Modified VLE

Scholars believe that formation of an adsorption layer around the pore walls is the dominant cause of condensation of fluid in nanopores at a higher pressures and temperatures compared to the bulk. Preferential adsorption of some components compared to the others affects the density

distribution of the fluid inside the nanopores which shifts the phase envelope towards a different composition or different critical properties. For inorganic pores, capillary condensation provides the same effect by accelerating the formation of a higher density layer around the pore walls due to the elevated fluid molecules- pore wall interactions. Many substances are mechanically and adhesively very sensitive to the presence of even traces of "condensable" vapors; "vapors whose liquids form a small contact angle with the surface". Once the first meniscus is formed, it will result in increased van der Waals interaction between vapor phase molecules inside the space of a capillary. Therefore, this process proceeds to a multilayer adsorption from vapor to the solid pore wall (Israelachvili, 2011). This phenomenon is known as capillary condensation; it occurs due to the strong pore wall fluid molecule interactions in tiny pore spaces and can lead to the point that the entire pore space is filled with condensed liquid above the saturation pressure of the vapor, Psat. Li and Firoozabadi (2009) proposed that phase change due to capillary condensation could occur beyond the cricondentherm in nano-pores even when the bulk fluid is still in single phase.

Several mathematical approaches are provided in the literature to account for inhomogeneous density distributions of confined fluids. In terms of modifying equations of state, two popular approaches are modification of the critical properties and accounting for capillary pressure (curvature effect) in VLE calculations. Figure 4.23 illustrates the shifted phase envelope for the same mixture (%70 ethane and %30 pentane) using VLE calculations modification. As shown in the figure, both experimental isochoric line and VLE modified phase envelope are similar in presenting the direction of the shift. The dew point pressure of the phase boundary obtained from modified VLE, matches the experimentally detected phase transition point for the confined fluid. At this point, more experimental data sets are required for bubble point detection to accurately compare and evaluate these methods.

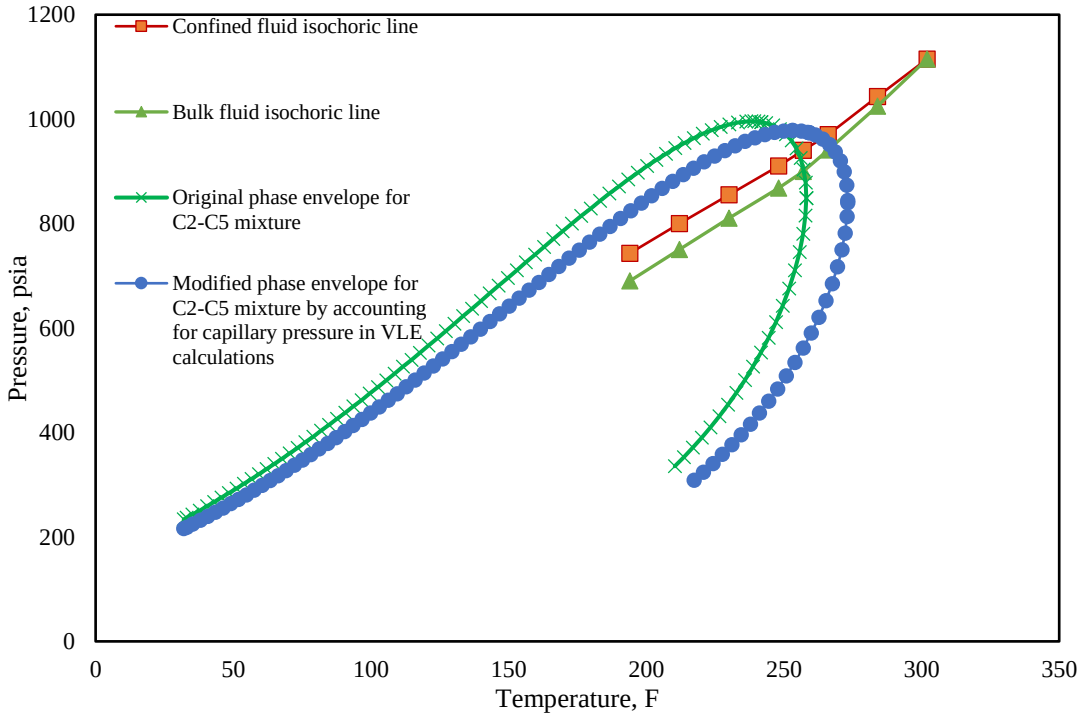

Figure 4.23. Original phase envelope and modified envelopes using critical properties/VLE modifications versus experimentally measured isochoric lines

4.8. Concluding Remarks of Isochoric Experiment

1. The unique behavior of each tight formation in comparison to the other ones makes it difficult to evaluate their reservoir properties suing conventional methods. The effect of nanoconfinement on fluid phase behavior and its long-term impact on reservoir characteristics and production profiles needs further investigations. In order to compare and evaluate available theories and mathematical models with their contradictory predictions of fluid behavior in a systematic way, more experimental work is required.
2. Isochoric experiment is one the most convenient approaches to evaluate fluid phase behavior in the presence of a nanoscale porous medium indirectly. High pressure high temperature resistance of the system alleviates providing reservoir condition for the fluid sample and conducting simultaneous experiments under both confined and bulk conditions assures identical experimental condition for both fluid samples and minimizes experimental errors. Constant volume nature of this experiment along with the possibility of isolating the fluid confined in porous medium from the bulk fluid are other advantages of this method.
3. The experimental data comparing behavior of pure gases in a decent range of pressures and temperatures for both bulk and confined condition prove that there is change in the properties and behavior of fluid caused by the porous media and pore size effect. Most of the published models in the literature agreed on the effect of confinement on fluid behavior. However, there are discrepancies in measuring the extent of this effect for various gases and different pore sizes using these correlations or models. This paper delivers experimental pressure measurements for pure gases (both hydrocarbon and non-hydrocarbon) undergoing the same heating process to evaluate present models and correlations in terms of their accuracy in capturing the level of the change in the behavior of confined fluid. Results show that although using correlation involving shifted critical properties of the fluid as a function pore and fluid molecule sizes are correct in terms of providing the direction of the shift, they do not show enough accuracy at higher temperatures. This effect needs to be further investigated to develop a new all-inclusive model or correlation that could be applied to a wide range of pore radii and molecular potentials for different pressure and temperatures.
4. For the gas mixtures, condensation is nanopores can happen while the pressure and temperature are still above the dew point of the bulk fluid calculated using equations of state. In other words, the phase envelope of confined gas condensate is larger than the phase envelope of the same bulk fluid which disapproves reduction of critical properties as a result of pore size reduction.
5. This work is a proof of concept for this methodology and needs to be further expanded for different gas condensate and oil mixtures towards achieving an all-inclusive model or correlation to be used for PVT studies in unconventional reservoirs.

Chapter 5: Conclusions and Future Work

In this work, the effect of nano-pores on the phase behavior of pure gases and gas condensates was experimentally investigated. Systematic laboratory experiments were conducted to study the phase behavior of pure gases and gas mixtures undergoing pressure and temperature changes through an isochoric procedure. The experimental results were compared to available mathematical models in the literature in order to identify the most promising approach in addressing the effect of pore size on the fluid phase behavior.

The crucial role of improving knowledge of extraction and production of fluids from unconventional reservoirs with micro- and even nano-Darcy permeabilities as a result of very small pore sizes and pore throats (1–300 nm in radius) was addressed in this work. Also, theorical models and experimental studies available in the literature were thoroughly discussed to highlight the contradictions among the outcome of several existing models and the significant experimental limitations of previous experimental studies.

Isochoric experiment, an accurate non-visual mean of phase transition point determination, which has been applied in disciplines other than petroleum engineering, was conducted on several gases. Results of these experiments provided not only an insight into the effect of pore size on phase transition point of gas mixtures, but also, an invaluable insight on the effect of pore size reduction on the behavior of pure gases which opens the door for future work in this area both experimentally and theoretically. The experimental procedure can be expanded to evaluate the phase transition point of other hydrocarbon mixtures in the laboratory with an acceptable accuracy, reasonable cost, and efficient time.

The experimental pressure measurements for pure gases (both hydrocarbon and non-hydrocarbon) undergoing the same process of temperature increase, were used to evaluate present models and correlations in terms of their accuracy in capturing the level of the change in the behavior of confined fluid. Results showed that although using correlation involving shifted critical properties of the fluid as a function pore and fluid molecule sizes are correct in terms of providing the direction of the shift, they do not show enough accuracy at higher temperatures. This effect needs to be further investigated to develop a new all-inclusive model or correlation that could be applied to a wide range of pore radii and molecular potentials for different pressure and temperatures.

Experimental results of phase behavior study for the binary mixture of gases, proved that condensation in nanopores can happen while the pressure and temperature are still above the dew point of the bulk fluid calculated using equations of state. This outcome was expected based on theorical modified VLE models available in the literature which was contradictory to the results of the models who utilized critical properties adjustment to address the effect of pore size on the fluid phase behavior.

This work is a proof of concept for this methodology and needs to be further expanded for different gas condensate and oil mixtures in different pore size distributions towards achieving an all-inclusive model or correlation to be used for PVT studies in unconventional reservoirs.

Nomenclature

θ_1	adsorbed amount of fluid, $(g/cm3)$
σ_1	measure of adsorbed molecule bond to the surface
μ_1	rate of gas condensation on an uncovered surface, $(g/cm3)$
b	Langmuir constant
p	Pressure, (bar)
T	temperature, (K)
θ_{excess}	excess amount of adsorbed phase $(g/cm3)$
ρ_{ads}	density of adsorbed phase, $(g/cm3)$
ρ_B	density of bulk fluid phase, $(g/cm3)$
K_n	Knudsen number
λ	gas molecular free path, (m)
r_{pore}	gas flow characteristic size or pore diameter, (m)
P_G	Pressure of gas phase, (bar)
P_L	Pressure of liquid phase, (bar)
σ	interfacial tension, $(J/m2)$
σ_∞	flat surface tension of the fluid, $(J/m2)$
δ	Tolman's length, (m)
r	droplet radius, (m)
v_G	specific volume of gas, (m^3/Kg)
v_L	specific volume of liquid, (m^3/Kg)
R	Universal Gas constant, $(J\ K^{-1}\ mol^{-1})$
G	Gibbs free energy, (J)
V	volume, (m^3)
n_i	the number of moles of component i
S	entropy, (J/K)
μ	chemical potential, (J/mol)
A	Helmholtz free energy, (J)
Ω	Grand potential, (J)

U	internal energy, (J)
a_p	Van der Waals constant
b_p	Van der Waals constant
ν	Average molar volume, $(m^{3} mol^{-1})$
r_p	Pore radius, (m)
δ_p	Width of the region fluid-wall intermolecular forces are effective, (m)
ε_p	energy parameter of the attractive interaction between two fluid molecules, (J)
P_{cB}	critical pressure of the bulk phase, (bar)
T_{cB}	critical temperature of the bulk phase, (K)
P_{cP}	critical pressure of the confined phase, (bar)
T_{cP}	critical temperature of the confined phase, (K)

References

Aerlin, B, 2009. *Molecular thermodynamics of complex systems,* Berlin, Berlin : Springer.

AHMADI, M. A. & BAHADORI, A. 2017. Chapter Eight - Gas Hydrates. *Fluid Phase Behavior for Conventional and Unconventional Oil and Gas Reservoirs.* Boston: Gulf Professional Publishing.

AHMED, T. 2010. Chapter 15 - Vapor-Liquid Phase Equilibria. *In:* AHMED, T. (ed.) *Reservoir Engineering Handbook (Fourth Edition).* Boston: Gulf Professional Publishing.

ALFI, M., NASRABADI, H. & BANERJEE, D. 2016. Experimental investigation of confinement effect on phase behavior of hexane, heptane and octane using lab-on-a-chip technology. *Fluid Phase Equilibria,* 423**,** 25-33.

ALFRED CHATENEVER; JOHN C. COULHAN, J. 1952. Visual Examination of Fluid Behavior in Porous Media. *Transactions of the American Institute of Mining, Metallurgical and Petroleum Engineers,* 195**,** 149-156.

ALLY, J., MOLLA, S. & MOSTOWFI, F. 2016. Condensation in Nanoporous Packed Beds. *Langmuir,* 32**,** 4494-4499.

AMBROSE, R. J., HARTMAN, R. C. & AKKUTLU, I. Y. 2011. Multi-component sorbed phase considerations for Shale Gas-in-place Calculations. Society of Petroleum Engineers.

AMBROSE, R. J., HARTMAN, R. C., DIAZ CAMPOS, M., AKKUTLU, I. Y. & SONDERGELD, C. 2010. New Pore-scale Considerations for Shale Gas in Place Calculations. Society of Petroleum Engineers.

ARAKCHEEV, V. G., VALEEV, A. A., MOROZOV, V. B. & OLENIN, A. N. 2008. CARS diagnostics of molecular media under nanoporous confinement. *Laser Physics,* 18**,** 1451-1458.

BEN-AMOTZ, D. & HERSCHBACH, D. R. 1990. Estimation of effective diameters for molecular fluids. *The Journal of Physical Chemistry,* 94**,** 1038-1047.

BRUNAUER, S., EMMETT, P. H. & TELLER, E. 1938. Adsorption of Gases in Multimolecular Layers. *Journal of the American Chemical Society,* 60**,** 309-319.

BUSTIN, R. M., BUSTIN, A. M. M., CUI, A., ROSS, D. & PATHI, V. M. 2008. Impact of Shale Properties on Pore Structure and Storage Characteristics. Society of Petroleum Engineers.

CASTRO, M. A., CLARKE, S. M., INABA, A., ARNOLD, T. & THOMAS, R. K. 1998. Competitive Adsorption of Simple Linear Alkane Mixtures onto Graphite. *The Journal of Physical Chemistry B,* 102**,** 10528-10534.

CHO, Y., EKER, E., UZUN, I., YIN, X. & KAZEMI, H. 2016. Rock Characterization in Unconventional Reservoirs: A Comparative Study of Bakken, Eagle Ford, and Niobrara Formations. Society of Petroleum Engineers.

CONWAY, J. H. 1999. *Sphere packings, lattices, and groups,* New York, New York : Springer.

DANDEKAR, A. Y. 2006. *Petroleum reservoir rock and fluid properties,* Boca Raton, FL, Boca Raton, FL : CRC/Taylor & Francis.

DANESH, A. 1998. 1 - Phase Behaviour Fundamentals. *In:* DANESH, A. (ed.) *Developments in Petroleum Science.* Elsevier.

DANESH, A., XU, D. H. & TODD, A. C. 1991. Comparative study of cubic equations of state for predicting phase behaviour and volumetric properties of injection gas-reservoir oil systems. *Fluid Phase Equilibria,* 63**,** 259-278.

DAWE, R. A., CARUANA, A. & GRATTONI, C. A. 2010. Immiscible Displacement in Cross-Bedded Heterogeneous Porous Media. *Transport in Porous Media,* 87**,** 335-353.

DEVEGOWDA, D., SAPMANEE, K., CIVAN, F. & SIGAL, R. F. 2012. Phase Behavior of Gas Condensates in Shales Due to Pore Proximity Effects: Implications for Transport, Reserves and Well Productivity. Society of Petroleum Engineers.

DIDAR, B. R. & AKKUTLU, I. Y. 2013. Pore-size Dependence of Fluid Phase Behavior and Properties in Organic-Rich Shale Reservoirs. Society of Petroleum Engineers.

DONG, X., LIU, H., HOU, J., WU, K. & CHEN, Z. 2016. Phase Equilibria of Confined Fluids in Nanopores of Tight and Shale Rocks Considering the Effect of Capillary Pressure and Adsorption Film. *Industrial & Engineering Chemistry Research,* 55**,** 798-811.

ERTAS, D., KELEMEN, S. R. & HALSEY, T. C. 2006. Petroleum Expulsion Part 1. Theory of Kerogen Swelling in Multicomponent Solvents. *Energy & Fuels,* 20**,** 295-300.

ETMINAN, S. R., JAVADPOUR, F., MAINI, B. B. & CHEN, Z. 2014. Measurement of gas storage processes in shale and of the molecular diffusion coefficient in kerogen. *International Journal of Coal Geology,* 123**,** 10-19.

EVANS, R., MARCONI, U. M. B. & TARAZONA, P. 1986. Capillary condensation and adsorption in cylindrical and slit-like pores. *Journal of the Chemical Society, Faraday Transactions 2: Molecular and Chemical Physics,* 82**,** 1763-1787.

FENG, Q.-X., DI, L.-C., TANG, G.-Q., CHEN, Z.-Y., WANG, X.-L. & ZOU, J.-X. A Visual Micro-Model Study: The Mechanism of Water Alternative Gas Displacement in Porous Media. Society of Petroleum Engineers.

FIGLIOLA, R. S. 1995. *Theory and design for mechanical measurements,* New York, New York : Wiley.

FIRINCIOGLU, T., OZKAN, E. & OZGEN, C. 2012. Thermodynamics of Multiphase Flow in Unconventional Liquids-Rich Reservoirs. Society of Petroleum Engineers.

FIROOZABADI, A. 2016. *Thermodynamics and applications in hydrocarbon energy production*, New York : McGraw-Hill Education.

FISHER, R., SHAH, M. K., ESKIN, D., SCHMIDT, K., SINGH, A., MOLLA, S. & MOSTOWFI, F. 2013. Equilibrium gas-oil ratio measurements using a microfluidic technique. *Lab on a Chip,* 13**,** 2623-2633.

HAIDER, B. A. 2015. effect of confinement on phase behavior in shale.

ISRAELACHVILI, J. N. 2011. *Intermolecular and surface forces,* Burlington, MA

Burlington, Mass., Burlington, MA : Academic Press.

JACKSON, C. L. & MCKENNA, G. B. 1990. The melting behavior of organic materials confined in porous solids. *The Journal of Chemical Physics,* 93**,** 9002-9011.

JIN, Z. & FIROOZABADI, A. Thermodynamic Modeling of Phase Behavior in Shale Media.

JIN, Z. & FIROOZABADI, A. 2016. Thermodynamic Modeling of Phase Behavior in Shale Media. *SPE Journal,* 21**,** 190-207.

KAMALVAND, M., KESHAVARZI, T. & MANSOORI, G. A. 2008. BEHAVIOR OF THE CONFINED HARD-SPHERE FLUID WITHIN NANOSLITS: A FUNDAMENTAL-MEASURE DENSITY-FUNCTIONAL THEORY STUDY. *International Journal of Nanoscience,* 07**,** 245-253.

KUILA, U. & PRASAD, M. 2013. Specific surface area and pore-size distribution in clays and shales. *Geophysical Prospecting,* 61**,** 341-362.

KUMAR, D., MASOULEH, S. F., GHASSEMI, A., RILEY, S. & ELLIOTT, B. 2018. A 3D Geomechanical Analysis of Horizontal Well Refracturing and “Frac- Hits”. 52nd U.S. Rock Mechanics/Geomechanics Symposium. Seattle, Washington: American Rock Mechanics Association

LAKE, L. W. 1989. *Enhanced oil recovery*, Old Tappan, NJ Prentice Hall Inc.

LANGMUIR, I. 1918. THE ADSORPTION OF GASES ON PLANE SURFACES OF GLASS, MICA AND PLATINUM. *Journal of the American Chemical Society,* 40**,** 1361-1403.

LAZIĆ, Ž. R. 2004. *Design of experiments in chemical engineering : a practical guide,* Weinheim [Germany], Weinheim Germany : Wiley-VCH.

LEE, L. H. 1991. Fundamentals of Adhesion. *Springer Science & Business Media***,** 454.

LENORMAND, R., ZARCONE, C. & SARR, A. 1983. Mechanisms of the displacement of one fluid by another in a network of capillary ducts. *Journal of Fluid Mechanics,* 135**,** 337-353.

LI, Z. & FIROOZABADI, A. 2009. Interfacial tension of nonassociating pure substances and binary mixtures by density functional theory combined with Peng–Robinson equation of state. *The Journal of Chemical Physics,* 130**,** 154108.
LI, Z., JIN, Z. & FIROOZABADI, A. 2014. Phase Behavior and Adsorption of Pure Substances and Mixtures and Characterization in Nanopore Structures by Density Functional Theory. *SPE Journal,* 19.
LU, X. & HU, Y. 2009. *Molecular Thermodynamics of Complex Systems*.
LUNDSTEDT, T., SEIFERT, E., ABRAMO, L., THELIN, B., NYSTRÖM, Å., PETTERSEN, J. & BERGMAN, R. 1998. Experimental design and optimization. *Chemometrics and Intelligent Laboratory Systems,* 42**,** 3-40.
LUO, S., NASRABADI, H. & LUTKENHAUS, J. L. 2016. Effect of confinement on the bubble points of hydrocarbons in nanoporous media. *AIChE Journal,* 62**,** 1772-1780.
MA, Y., JIN, L. & JAMILI, A. 2013. Modifying van der Waals Equation of State to Consider Influence of Confinement on Phase Behavior. Society of Petroleum Engineers.
MANTILLA, I. D. 2012. Accurate measurements and modeling of the PρT behavior of pure substances and natural gas-like hydrocarbon mixtures.
MCCAIN, W. D. 1990. *The properties of petroleum fluids,* Tulsa, Okla., Tulsa, Okla. : PennWell Books.
MCCAIN, W. D. 2010. *Petroleum Reservoir Fluid Property Correlations,* Tulsa, Tulsa : PennWell Corporation.
MCGONIGAL, G. C., BERNHARDT, R. H. & THOMSON, D. J. 1990. Imaging alkane layers at the liquid/graphite interface with the scanning tunneling microscope. *Applied Physics Letters,* 57**,** 28-30.
MESBAH, M. & BAHADORI, A. 2017. Chapter Two - Equations of State. *Fluid Phase Behavior for Conventional and Unconventional Oil and Gas Reservoirs.* Boston: Gulf Professional Publishing.
MOSTOWFI, F., MOLLA, S. & TABELING, P. 2012. Determining phase diagrams of gas-liquid systems using a microfluidic PVT. *Lab on a Chip,* 12**,** 4381-4387.
NAGY, S. & SIEMEK, J. 2014. Confined Phase Envelope of Gas-Condensate Systems in Shale Rocks. *Archives of Mining Sciences.*
NELSON, P. H. 2009. Pore-throat sizes in sandstones, tight sandstones, and shales. *AAPG Bulletin,* 93**,** 329-340.
NGO, T. 2015. Reservoir capacity estimates in shale plays based on experimental adsorption data. 94.
NOJABAEI, B., JOHNS, R. T. & CHU, L. 2012. Effect of Capillary Pressure on Fluid Density and Phase Behavior in Tight Rocks and Shales. Society of Petroleum Engineers.
PARSA, E., YIN, X. & OZKAN, E. Direct Observation of the Impact of Nanopore Confinement on Petroleum Gas Condensation. Society of Petroleum Engineers.
PARSA, E., YIN, X. & OZKAN, E. 2015. Direct Observation of the Impact of Nanopore Confinement on Petroleum Gas Condensation. Society of Petroleum Engineers.
PATHAK, M., DEO, M., CRAIG, J. & LEVEY, R. 2014. Geologic Controls on Production of Shale Play Resources: Case of the Eagle Ford, Bakken and Niobrara. Unconventional Resources Technology Conference.
PENG, B. & YU, Y.-X. 2008. A Density Functional Theory with a Mean-field Weight Function: Applications to Surface Tension, Adsorption, and Phase Transition of a Lennard-Jones Fluid in a Slit-like Pore. *The Journal of Physical Chemistry B,* 112**,** 15407-15416.
PETERSON, B. K., WALTON, J. P. R. B. & GUBBINS, K. E. 1986. Fluid behaviour in narrow pores. *Journal of the Chemical Society, Faraday Transactions 2: Molecular and Chemical Physics,* 82**,** 1789-1800.
PINHO, B., GIRARDON, S., BAZER-BACHI, F., BERGEOT, G., MARRE, S. & AYMONIER, C. 2014. A microfluidic approach for investigating multicomponent system thermodynamics at high pressures and temperatures. *Lab on a Chip,* 14**,** 3843-3849.

PITAKBUNKATE, T., BALBUENA, P. B., MORIDIS, G. J. & BLASINGAME, T. A. 2015. Effect of Confinement on Pressure/Volume/Temperature Properties of Hydrocarbons in Shale Reservoirs.

RAJPUT, A., Q.A. PANHWAR, U.A. NAHER, S. RAJPUT AND E. HOSSAIN ET AL. 2014. Influence of incubation period, temperature and different phosphate levels on phosphate adsorption in soil. *Am. J. Agric. Biol. Sci.,* 9.

REINECKE, S. A. & SLEEP, B. E. 2002. Knudsen diffusion, gas permeability, and water content in an unconsolidated porous medium. *Water Resources Research,* 38**,** 16-1-16-15.

ROBERT, M. A., LEGROS, M., FACCHINELLI, L., VALERIO, L., RAMSEY, J. M., SCOTT, T. W., GOULD, F. & LLOYD, A. L. 2012. Mathematical Models as Aids for Design and Development of Experiments: The Case of Transgenic Mosquitoes. *Journal of Medical Entomology,* 49**,** 1177-1188.

ROQUE-MALHERBE, R. M. A. & ROQUE-MALHERBE, R. M. A. 2007. *Adsorption and diffusion in nanoporous materials,* Boca Raton, Boca Raton : CRC Press.

ROSS, D. J. K. & BUSTIN, M. R. 2009. The importance of shale composition and pore structure upon gas storage potential of shale gas reservoirs. *Marine and Petroleum Geology,* 26**,** 916-927.

ROY, S., RAJU, R., CHUANG, H. F., CRUDEN, B. A. & MEYYAPPAN, M. 2003. Modeling gas flow through microchannels and nanopores. *Journal of Applied Physics,* 93**,** 4870-4879.

SALAHSHOOR, S. & FAHES, M. 2018. Experimental Determination of the Phase Transition Point in Gas Condensates using a Cost-Effective Semiautomated Isochoric Apparatus. *SPE Western Regional Meeting.* Garden Grove, California, USA: Society of Petroleum Engineers.

SALAHSHOOR, S. & FAHES, M. 2017. A Study on the Factors Affecting the Reliability of Laboratory-Measured Gas Permeability. Abu Dhabi International Petroleum Exhibition & Conference. Abu Dhabi, UAE: Society of Petroleum Engineers.

SALAHSHOOR, S. & FAHES, M. 2018a. Experimental and Theoretical Investigation of the Confinement Effect on Gas Properties in Nano-scale Porous Media. Unconventional Resources Technology Conference. Houston, Texas, USA: Unconventional Resources Technology (URTeC).

SALAHSHOOR, S. & FAHES, M. 2018b. Experimental Determination of the Phase Transition Point in Gas Condensates using a Cost-Effective Semiautomated Isochoric Apparatus. SPE Western Regional Meeting. Garden Grove, California, USA: Society of Petroleum Engineers.

SALAHSHOOR, S., FAHES, M. & TEODORIU, C. 2018. A review on the effect of confinement on phase behavior in tight formations. Journal of Natural Gas Science and Engineering, 51, 89-103.

SANAEI, A., JAMILI, A. & CALLARD, J. 2014. Effect of Pore Size Distribution and Connectivity on Phase Behavior and Gas Condensate Production From Unconventional Resources. Society of Petroleum Engineers.

SCHETTLER, P. D., PARMELY, C. R. & LEE, W. J. 1989. Gas Storage and Transport in Devonian Shales.

SIGMUND, P. M., DRANCHUK, P. M., MORROW, N. R. & PURVIS, R. A. Retrograde Condensation in Porous Media.

SIGMUND, P. M., DRANCHUK, P. M., MORROW, N. R. & PURVIS, R. A. 1973. Retrograde Condensation in Porous Media. *Society of Petroleum Engineers Journal,* 13**,** 93-104.

SINGH, S. K., SINHA, A., DEO, G. & SINGH, J. K. 2009. Vapor−Liquid Phase Coexistence, Critical Properties, and Surface Tension of Confined Alkanes. *The Journal of Physical Chemistry C,* 113**,** 7170-7180.

SONDERGELD, C. H., AMBROSE, R. J., RAI, C. S. & MONCRIEFF, J. 2010. Micro-Structural Studies of Gas Shales. Society of Petroleum Engineers.

SUN, Z., SHI, J., WU, K. & LI, X. 2018. Gas Flow Behavior through Inorganic Nanopores in Shale Considering Confinement Effect and Moisture Content. *Industrial & Engineering Chemistry Research,* 57**,** 3430-3440.

TALU, O. & MYERS, A. L. 2001. Reference potentials for adsorption of helium, argon, methane, and krypton in high-silica zeolites. *Colloids and Surfaces A: Physicochemical and Engineering Aspects,* 187-188**,** 83-93.

TAN, S. P. & PIRI, M. 2015. Equation-of-state modeling of confined-fluid phase equilibria in nanopores. *Fluid Phase Equilibria,* 393**,** 48-63.

THOMMES, M., FINDENEGG, G. H. & SCHOEN, M. 1995. Critical Depletion of a Pure Fluid in Controlled-Pore Glass. Experimental Results and Grand Canonical Ensemble Monte Carlo Simulation. *Langmuir,* 11**,** 2137-2142.

TINDY, R. & RAYNAL, M. 1966. Are Test-Cell Saturation Pressures Accurate Enough? *Oil & Gas Journal,* 64**,** 14.

TOSCANO, A., BILOTTI, F., ASDRUBALI, F., GUATTARI, C., EVANGELISTI, L. & BASILICATA, C. 2016. Recent Trends in the World Gas Market: Economical, Geopolitical and Environmental Aspects. *Sustainability,* 8**,** 154.

TRAVALLONI, L., CASTIER, M., TAVARES, F. W. & SANDLER, S. I. 2010a. Critical behavior of pure confined fluids from an extension of the van der Waals equation of state. *The Journal of Supercritical Fluids,* 55**,** 455-461.

TRAVALLONI, L., CASTIER, M., TAVARES, F. W. & SANDLER, S. I. 2010b. Thermodynamic modeling of confined fluids using an extension of the generalized van der Waals theory. *Chemical Engineering Science,* 65**,** 3088-3099.

VELEZ, A., PEREDA, S. & BRIGNOLE, E. A. 2010. Isochoric lines and determination of phase transitions in supercritical reactors. *The Journal of Supercritical Fluids,* 55**,** 643-647.

WANG, S., FENG, Q., JAVADPOUR, F., XIA, T. & LI, Z. 2015. Oil adsorption in shale nanopores and its effect on recoverable oil-in-place. *International Journal of Coal Geology*.

WANG, S., JAVADPOUR, F. & FENG, Q. 2016. Confinement Correction to Mercury Intrusion Capillary Pressure of Shale Nanopores. *Scientific Reports,* 6**,** 20160.

WAXMAN, M. & HASTINGS, J. R. 1971. A Burnett apparatus for the accurate determination of gas compressibility factors and second virial coefficients and an evaluation of Its capability based on some results for argon and carbon dioxide. *J. Res. Natl. Bur. Stand. Sect. C,* 75**,** 165-176.

WONG, A. P. Y., KIM, S. B., GOLDBURG, W. I. & CHAN, M. H. W. 1993. Phase separation, density fluctuation, and critical dynamics of ${\mathit{N}}_{2}$ in aerogel. *Physical Review Letters,* 70**,** 954-957.

WU, Q. 2014. *Investigation of fluids flow behavior in nano-scale channels by using optic imaging system.* Ph. D. in Chemistry, Missouri University of Science and Technology.

YUSUKE, H. & MAKOTO, Y. 2004. Phase behaviour of water confined in Vycor glass at high temperatures and pressures. *Journal of Physics: Condensed Matter,* 16**,** 7903.

ZARRAGOICOECHEA, G. J. & KUZ, V. A. 2002. van der Waals equation of state for a fluid in a nanopore. *Physical review. E, Statistical, nonlinear, and soft matter physics,* 65**,** 021110.

ZARRAGOICOECHEA, G. J. & KUZ, V. A. 2004. Critical shift of a confined fluid in a nanopore. *Fluid Phase Equilibria,* 220**,** 7-9.

ZHOU, J., PATIL, P., EJAZ, S., ATILHAN, M., HOLSTE, J. C. & HALL, K. R. 2006. (p,Vm,T) and phase equilibrium measurements for a natural gas-like mixture using an automated isochoric apparatus. *The Journal of Chemical Thermodynamics,* 38**,** 1489-1494.

Appendix A: Lagrange Multiplier

Method of Lagrange multipliers is used to locate the minimum or maximum of a function. Defining a function as F=F(x,y,z), at the maximum or minimum we will have:

$$dF(x,y,z) = \left(\frac{\partial F}{\partial x}dx + \frac{\partial F}{\partial y}dy + \frac{\partial F}{\partial z}dz\right) = 0$$

Where x,y and z are independent variables, hence dx, dy, and dz are linearly independent. Subsequently we have:

$$\frac{\partial F}{\partial x} = \frac{\partial F}{\partial y} = \frac{\partial F}{\partial z} = 0$$

To indicate those values which makes F(x,y,z) maximum or minimum, a constraint needs to be defined. G(x,y,z)=C is the equation of a surface which can be defined as a constraint for optimizing F(x,y,z). Note that in this case, dx, dy and dz are not linearly independent, because only two of them are linearly independent.

At maximum or minimum, we have:

$$dG(x,y,z) = \left(\frac{\partial G}{\partial x}dx + \frac{\partial G}{\partial y}dy + \frac{\partial G}{\partial z}dz\right) = 0$$

Lagrange defined an auxiliary function as below in order to solve this problem:

$$H = F + \lambda G$$

Where, λ is a Lagrange multiplier. As mentioned above, dF=0 and dG=0, therefore, dH=0.

$$dF + \lambda dG = 0$$

Consequently,

$$\left(\frac{\partial F}{\partial x} - \lambda\frac{\partial G}{\partial x}\right)dx + \left(\frac{\partial F}{\partial y} - \lambda\frac{\partial G}{\partial y}\right)dy + \left(\frac{\partial F}{\partial z} - \lambda\frac{\partial G}{\partial z}\right)dz = 0$$

Since λ is an arbitrary parameter, we can choose it at (x_0, y_0, z_0) applying $\frac{\partial F}{\partial z} - \lambda\frac{\partial G}{\partial z}dz = 0$

Therefore, the remaining terms are linearly independent, hence we have:

$$\left(\frac{\partial F}{\partial x} - \lambda\frac{\partial G}{\partial x}\right)dx + \left(\frac{\partial F}{\partial y} - \lambda\frac{\partial G}{\partial y}\right)dy = 0$$

Where,

$$\left(\frac{\partial F}{\partial x} - \lambda\frac{\partial G}{\partial x}\right)dx = 0$$

$$\left(\frac{\partial F}{\partial y} - \lambda \frac{\partial G}{\partial y}\right) dy = 0$$

Now, with the help of these three equations (listed below once again), we have enough equations to locate the maximum or minimum.

1. $\left(\frac{\partial F}{\partial x} - \lambda \frac{\partial G}{\partial x}\right) dx = 0$
2. $\left(\frac{\partial F}{\partial y} - \lambda \frac{\partial G}{\partial y}\right) dy = 0$
3. $(\frac{\partial F}{\partial z} - \lambda \frac{\partial G}{\partial z}) dz = 0$

Appendix B: Legendre Transformation

Legendre transformation is used to enable us describing a function using a different (conjugate) set of variables. Considering a function f(x,y), the total derivative of the function is given as:

$$df = (\frac{\partial F}{\partial x})_y dx + (\frac{\partial F}{\partial y})_x dy$$

Defining partial derivatives as:

$$u = (\frac{\partial F}{\partial x})_y$$

$$v = (\frac{\partial F}{\partial y})_x$$

df can be re-written as $df = udx + vdy$.

We call u and x conjugate variable, and likewise v and y.

In order to change to a new representation, the function $g(u,x)$ is defined as $g(u,x) = f(x,y) - ux$. Which gives us the following equation:

$$dg = df - xdu - udx$$

Using the total derivative of $f(x,y)$ then:

$$dg = -xdu + vdy$$

Where, $x = -\frac{\partial g}{\partial u}$ and $v = \frac{\partial g}{\partial y}$.

In summary, we have transformed a function $f(x,y)$ to a new function $g(u,y)$ by applying Legendre transformation, in which variable x is replaced by its conjugate variable u. Needless to say, one could replace y with v to obtain $h(x,v)$ or could replace both independent variables to get $k(u,v)$. In general, there are 2^n potentials for a function of n independent variables to be re-written in the form of conjugate variables.

Appendices C & D: Functionals

Defining y(x) on an interval like [a,b], gives us a curve on (x,y) plane. Functionals are defined as functions of another functions (instead of another variable). Therefore, functional F could be defined as:

$$F[y(x)] = \int_a^b f\big(x, y(x), y_x(x)\big)dx$$

Where $y_x(x) = \frac{dy}{dx}$. A function like F[y(x)] is named a "functional" to be distinguishable from ordinary real-valued functions, whose domains consists of ordinary variables. The value of this functional will depend on the choice of the function, y(x), and calculus of variations deal with finding a function which makes the above-mentioned integral minimum or maximum.

In order to drive extreme values of a functional, the function $f\big(x, y(x), y_x(x)\big)$ in the integral needs to have continuous derivatives of x, y, and y_x. The continuity of derivatives is also needed because differentiation requires applying chain rules and Leibniz rules.

If $y(x)$ is a curve on [a,b] which minimizes the functional f[y(x)], then:

$$\delta F[y(x)] = \delta \int_a^b f\big(x, y(x), y_x(x)\big)dx = \int \left(\frac{\partial f}{\partial y}\delta y + \frac{\partial f}{\partial y_x}\delta y_x\right) = 0$$

Which can be easily re-written as below using rules of chain:

$$\delta F[y(x)] = \int \left(\frac{\partial f}{\partial y} - \frac{d}{dx}\frac{\partial f}{\partial y_x}\right)\delta y(x)dx = 0$$

In terms of so-called functional derivatives, it can be rearranged as:

$$\frac{\delta F[y(x)]}{\delta y(x)} = \int \left(\frac{\partial f}{\partial y} - \frac{d}{dx}\frac{\partial f}{\partial y_x}\right)dx = 0$$

The function y=y(x) which minimizes the functional F[y(x)] complies with the following differential equation:

$$\frac{\partial f}{\partial y} - \frac{d}{dx}\left(\frac{\partial f}{\partial y_x}\right) = 0$$

This equation is the so-called Euler-Lagrange equation.

Appendix E: Diffusion due to confinement

Generally, diffusion is a very slow process and is neglected in conventional reservoirs because in such reservoirs, fluid velocity is high and Darcy flow is dominated. However, in unconventional reservoirs where the fluid velocity is much lower, the contribution of diffusion is significant. Heterogeneity of the pore size distribution is the key factor in developing concentration gradient which leads to diffusive flow (Firincioglu et al., 2012).

Knudsen number defined by Knudsen (1934) is usually used to describe gas flow pattern in porous media. This dimensionless number is defined as the ratio of the molecular mean free path (free path travelled by molecule) (λ) to the pore diameter (D_{pore}).

$$K_n = \frac{\lambda}{D_{pore}}$$

Flow regime is defined based on Knudsen number as below:

Table E.1 Flow regimes based on Knudsen number (Roy et al., 2003).

Kn range	Flow Regime
Kn < 0.001	Darcy Flow
0.001 < Kn < 0.01	Slippage Flow
0.01 < Kn < 0.1	Fick Diffusion
0.1 < Kn < 10	Transition Diffusion
Kn > 10	Knudsen Diffusion

Knudsen diffusion is dominant regime during flow in nano-pore system because of elevated molecule-wall interactions and can be calculated for a gas in a cylinder shape pore as below:

$$D_k = \frac{D_{pore}}{3}\sqrt{\frac{8RT}{\pi M}}$$

Where D_k ($m^2.s^{-1}$) is Knudsen diffusion coefficient, R is molar mass constant ($Pa.m^3.mol^{-1}.K^{-1}$), T is temperature (K), M is molecular weight of gas ($kg.mol^{-1}$), and D_{pore} is pore diameter (m).

Having D_k, Knudsen flux of gas in a cylindrical capillary is:

$$N_k^i = -C D_k^i \nabla x_i$$

Where N_k^i is the molar Knudsen flux of gas i (mol m^2 s^{-1}), C is the total molar density ($mol.m^{-3}$), D_k^i is the Knudsen diffusion coefficient ($m^2.s^{-1}$) for gas i, and ∇x_i is mole fraction gradient (m^{-1}) (Reinecke and Sleep, 2002). It worth mentioning that pore-wall interactions only cause Knudsen diffusion and for that Knudsen diffusion is one of the outcomes of confinement and this should not be confused with Fickian diffusion. Fickian diffusion is dominant whenever there is a concentration difference (after desorption for example) and is modeled using Ficks Diffusion Law based on concentration gradient between two points:

$$J = -D\nabla C$$

Where J (mol m^2 s^{-1}) is diffusion flux, ∇C (mol m^{-4}) is the concentration, and D (m^2 s^{-1}) is diffusion coefficient.

Fick's second law gives us a concentration independent diffusion coefficient.

$$\frac{\partial c}{\partial t} = D\nabla.(\nabla C)$$

These two diffusion equations can be related to fluid flow equations in porous media using continuity equation which is applicable in modeling diffusive flow of fluid through tight formations.

Appendix F: Labview Code and Pressure Recording

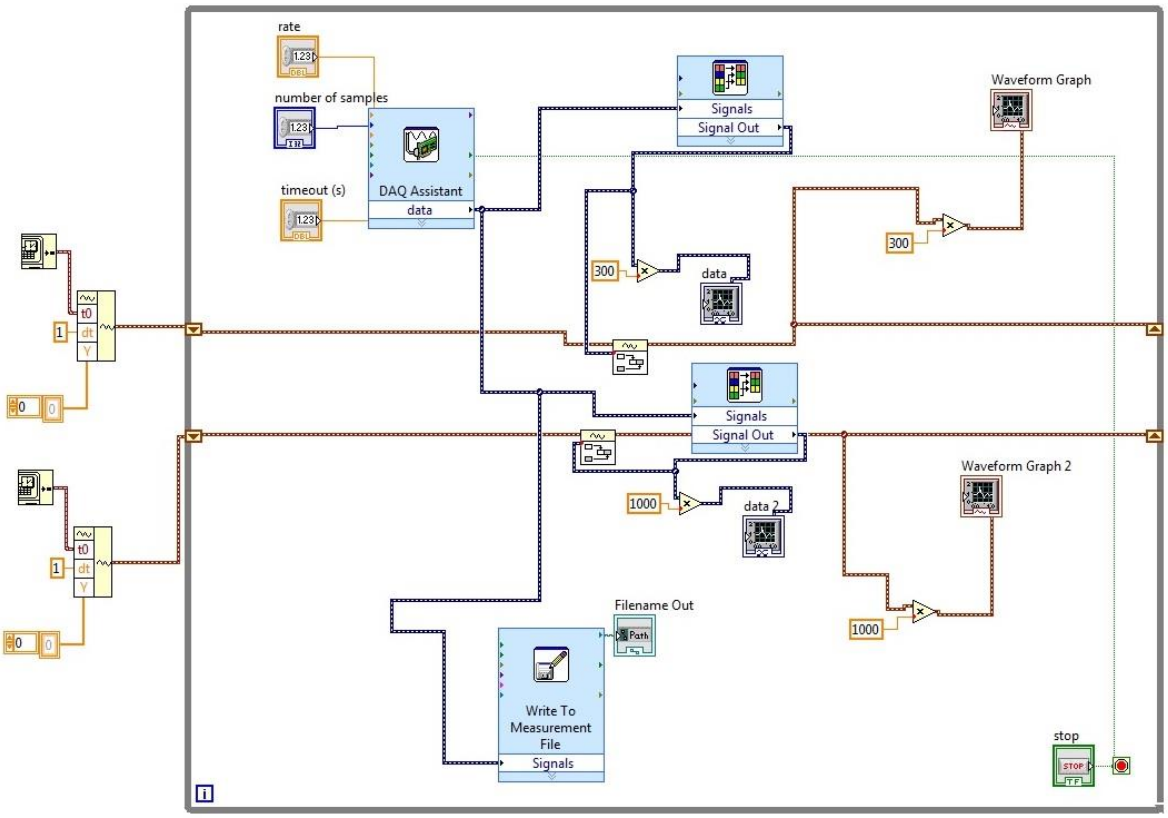

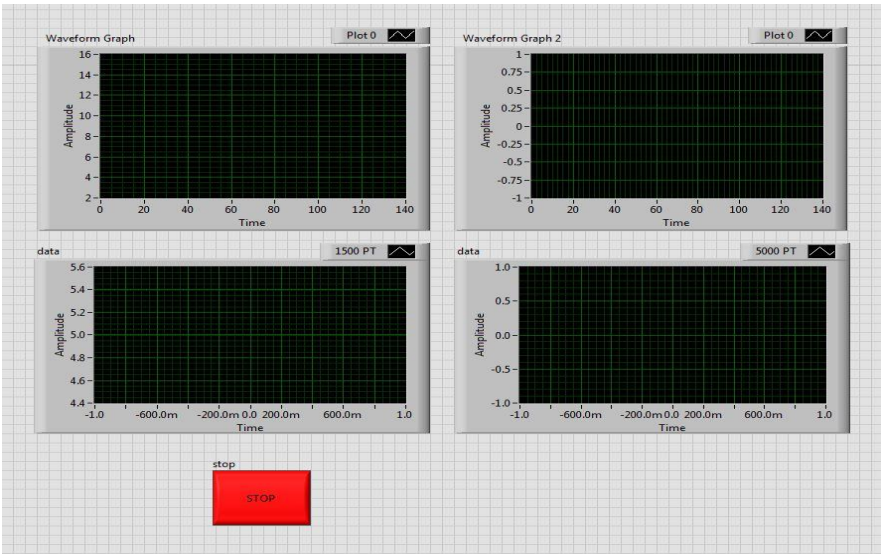

Appendix G: Volume Measurements

G.1. Volume test (Bulk Isochoric Experiment)

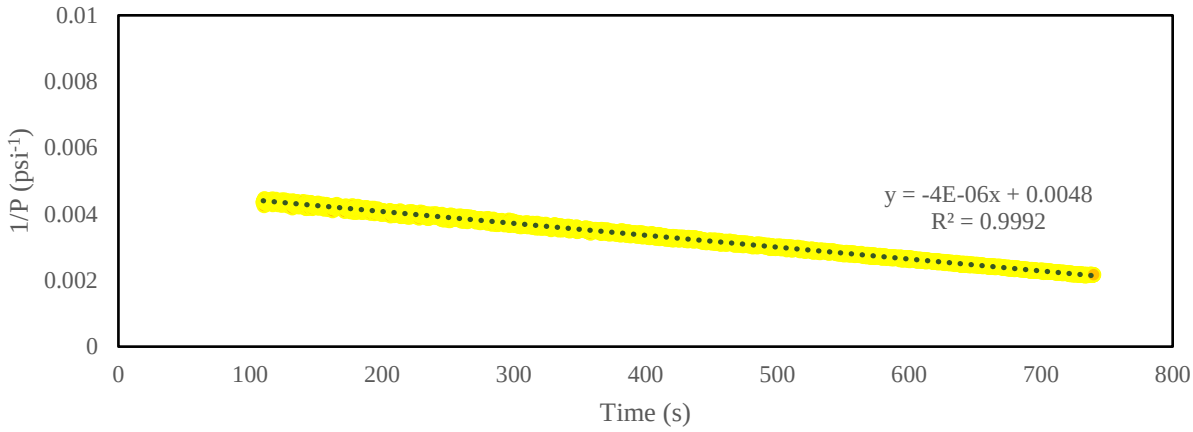

flowrate (q) cc/min	time (s)	q (cc/s)	V=q*t
50	739.9	0.833333	616.5833
slope	**intercept**	**nRT**	**V_i**
0.0000040000	0.0048000000	208333.3	**1000**

G.2. Volume test (Bulk vs. Confined Isochoric Experiment) V_1,V_2, V_3 Determination

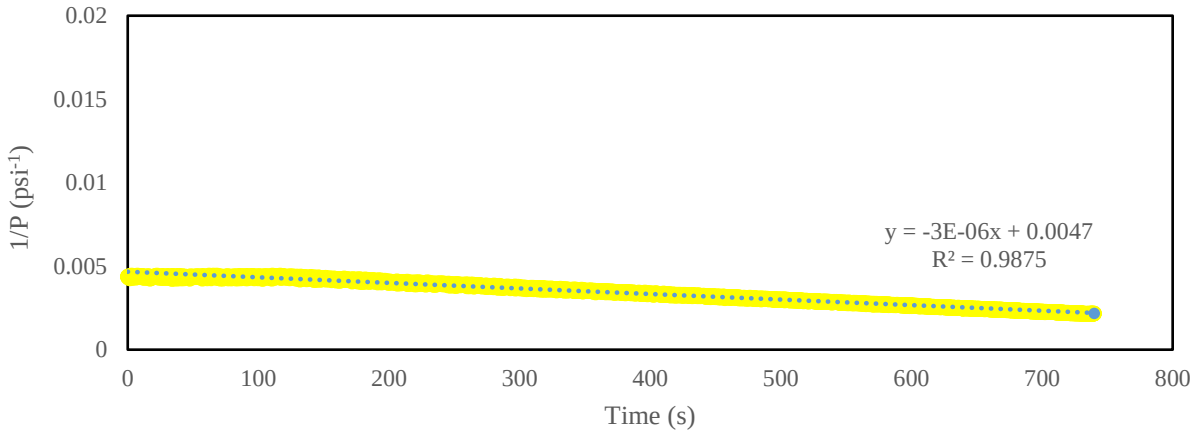

flowrate (q) cc/min	time (s)	q (cc/s)	V=q*t
50	739.9	0.833333	616.5833
slope	**intercept**	**nRT**	**V_1**
0.0000030000	0.0047000000	277777.8	**1305.556**

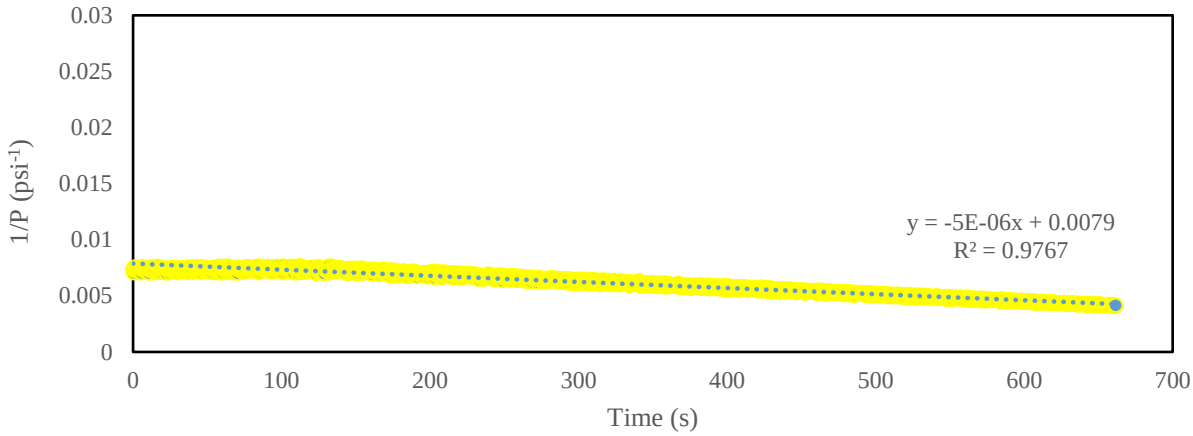

flowrate (q) cc/min	time (s)	q (cc/s)	V=q*t
50	740	0.833333	616.6667
slope	**intercept**	**nRT**	**V_1+V_2**
0.000005	0.0079	166666.7	**1316.667**

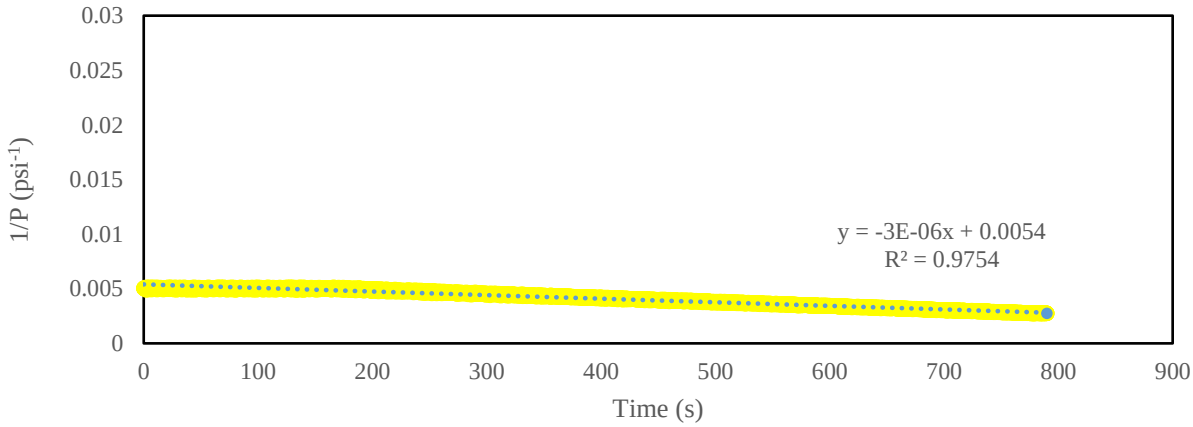

flowrate (q) cc/min	time (s)	q (cc/s)	V=q*t
50	790	0.833333	658.3333
slope	**intercept**	**nRT**	**$V_1+V_2+V_3$**
0.000003	0.0054	277777.8	**1500**

Appendix H: Supplemental Graphs from Experiment

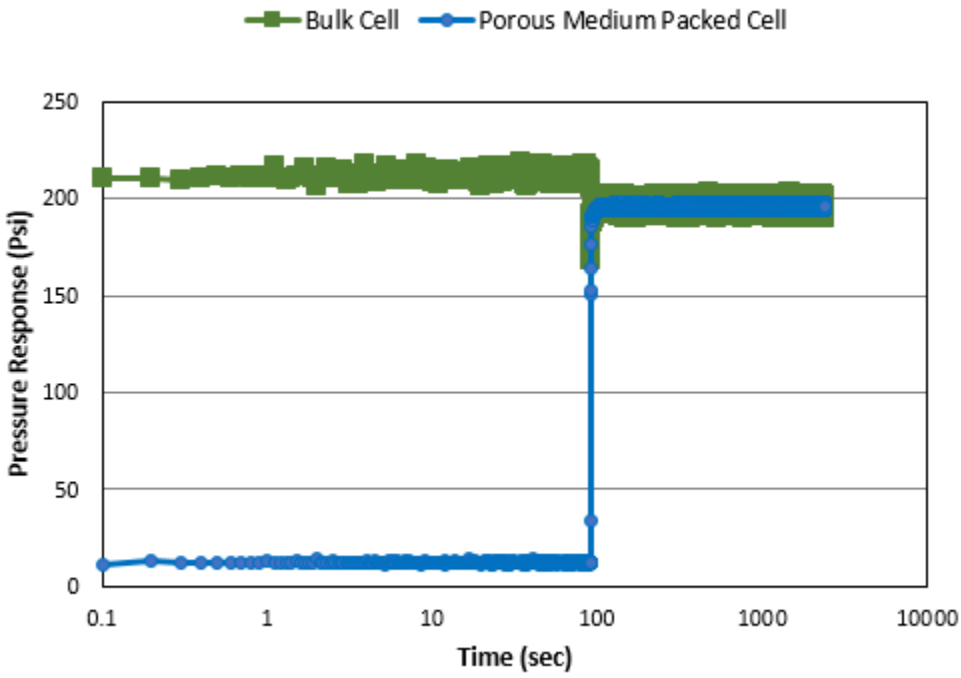

Figure H1. Pressure responses of Helium in bulk and packed PVT cells. Packed cell is under vacuum and gas is introduced to it by opening the isolation valve between packed and bulk cell, leading to pressure equilibrium of both cells.

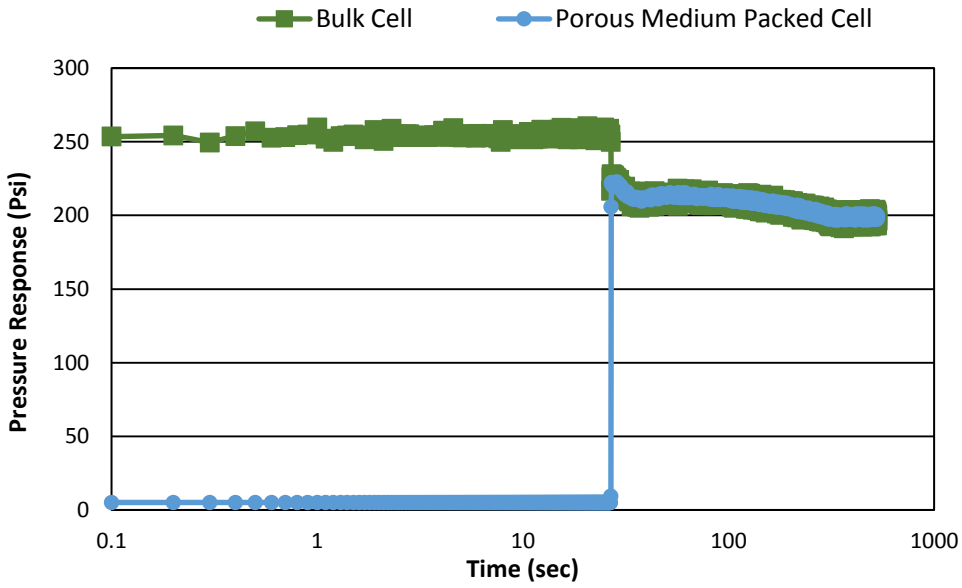

Figure H2. Pressure responses of Helium in bulk and packed PVT cells. Matching responses of both transducers under pressure reduction confirms successful calibration

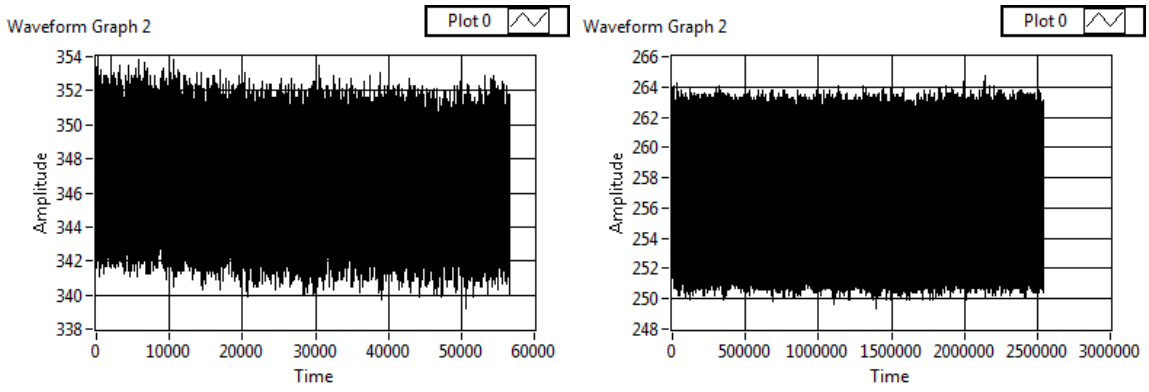

Figure H3. Pressure responses of Helium in bulk PVT cell. Stabilized pressure recorded for each temperature step (right graph) is recorded after 2500000 seconds equal to 28 days.

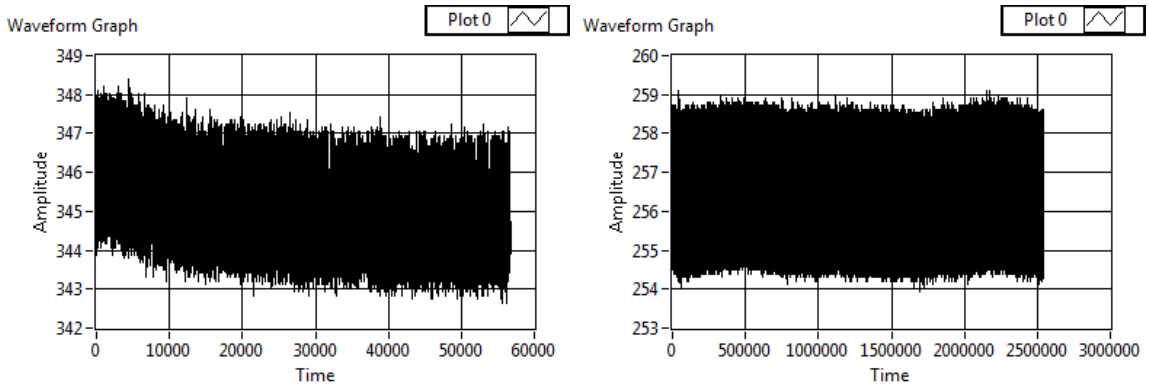

Figure H4. Pressure responses of Helium in porous medium packed PVT cell. Stabilized pressure recorded for each temperature step (right graph) is recorded after 2500000 seconds equal to 28 days. Initial decline of the pressure in the cell (left graph) is an evidence of gas diffusion inside the porous medium which stops after establishing equilibrium.